Acoustic Aberration in Non-Invasive Histotripsy Therapy

by

Yohan Kim

A dissertation submitted in partial fulfillment
of the requirements for the degree of
Doctor of Philosophy
(Biomedical Engineering)
in The University of Michigan
2013

Doctoral Committee:

Assistant Professor Zhen Xu, Chair
Professor Charles A. Cain
Professor J. Brian Fowlkes
Assistant Research Scientist Timothy L. Hall
Clinical Assistant Professor Gabe E. Owens

“As for the future, your task is not to foresee it, but to enable it.”

(Antoine de Saint-Exupéry)

Dedication

To all the teachers who encouraged and inspired me

in my lifelong pursuit of knowledge and wisdom,

especially my very first mentors, Mom and Dad.

Acknowledgements

I'm deeply grateful to my advisor, Dr. Zhen Xu, for her guidance and patience in mentoring me throughout my years as a graduate student. Dr. Xu's earnest enthusiasm and dedication towards research have always been sources of motivation and encouragement in many of the projects I had the chance to work in. I'm also indebted to all my committee members, Drs. Charles Cain, Brian Fowlkes, Gabe Owens and Timothy Hall. I'm thankful to have had the opportunity to work under Dr. Cain, whose exceptional research creativity has been a continuous driver of innovation in our laboratory. I'd like to thank Dr. Fowlkes for his willingness to share his broad research expertise in discussions that provided critical insights for a variety of projects. I'm grateful to Dr. Owens for his continuous collaboration in many of our *in vivo* experiments and for sharing his medical knowledge, allowing us to better evaluate our research under a clinical perspective. I'm also thankful to Dr. Hall, who has been an indispensable source of expertise in all practical aspects regarding the operation of transducers in the lab. It is unnecessary to say that his help and collaboration made much of the research presented herein possible.

I'd like to thank my colleagues, Ryan, Kuang-Wei, Alex, Eli, Steven and Xi, for all their help over the years, and for making the lab a more convivial place to work. I'd also like to extend my gratitude to my former lab mates, Drs. Tzu-Yin Wang and Adam

Maxwell, who often took on the role of secondary mentors when I first joined the lab and with whom I had the opportunity to share many productive experiments and discussions. I'm thankful to our collaborators at the UM hospital for their help with many of our projects, especially our veterinarian, Dr. Kimberly Ives who has always been an essential team member in our *in vivo* studies.

Of course, research would be impossible without a competent support team, and I'm grateful to all of our administrative staff, who kept everything running smoothly in our department, especially to Kathy McCrumb, Maria Steele, Katharine Guarino, Chuck Nicholas, Dana Jackson, Susan Bitzer and Tonya Brown (now retired). Whether I was placing lab orders, or straightening out my student paperwork, our management staff was always prompt and efficient in helping me address whatever issues I was faced with.

Finally, I thank my family, for the support and encouragement they've given me over the years, especially to my aunt Joyce in Portland, for always taking care of me as a surrogate parent while I was in the US. Lastly, I'm blessed to have my parents, missionaries Kyung Jo Kim (Dad) and Young Joo Kwon (Mom) for their continuous love and support, for providing me with the opportunity to achieve more despite of all limitations and difficulties, and for sharing with me, through their many years of selfless dedication in serving God and community, the best fundamentals that I'll carry through life, which no amount of research could have taught.

Ann Arbor, Michigan

April, 2013

Table of Contents

List of Figures

List of Tables

List of Appendices

Abstract

Acoustic Aberration in Non-Invasive Histotripsy Therapy

Chair: Zhen Xu

Acoustic aberration effects have been extensively studied over the years for high intensity focused ultrasound (HIFU) due to the significant therapeutic disruption they can cause in thermal ablation procedures, often rendering the treatment ineffective without the implementation of aberration correction mechanisms.

Histotripsy therapy uses highly energetic cavitation bubble clouds to mechanically fractionate tissue. The cavitation bubble cloud initiation is dependent on a pressure threshold mechanism, which allows this process to be controlled by the pressure amplitude available at the focus. The work presented herein explores the therapeutic effects of acoustic aberration in the scope of histotripsy therapy and investigates the feasibility of conducting non-invasive histotripsy procedures without using correction mechanisms in distinct therapeutic contexts likely to introduce high degrees of acoustic aberration.

The first context investigated is transcostal therapy. It is demonstrated that histotripsy therapy is able to generate precise lesions through rib obstacles without aberration correction despite the presence of large grating lobes in the focal profile. An *in* *vivo* study follows, in which comparable porcine liver lesions are created through windows with full and no ribcage obstruction, inducing no visible damage on overlying tissues.

The second context investigates transabdominal fetal therapy. It is shown that histotripsy therapy can achieve precise fetal tissue ablation in sheep models through the intact maternal abdomen without aberration correction. A long-term study on the impact of the therapy in the course of pregnancy is conducted, indicating the potential safety of this technique for non-invasive fetal applications.

The third, and perhaps the most challenging therapeutic context involves transcranial therapy. A large aperture array transducer is specifically designed, and a novel sonication mechanism using extremely short pulses with large negative pressures is introduced. It is shown that precise cavitation lesions can be successfully generated transcranially by careful modulation of the focal pressure amplitude.

Overall results show that the pressure threshold mechanism governing the initiation of histotripsy bubble clouds lends the therapy a considerable degree of immunity against acoustic aberration effects, a feature, which in combination with the low thermal impact of the therapy would be highly beneficial for a variety of non-invasive therapeutic applications.

Chapter 1

Introduction

The main objectives of this work are to explore the effects of acoustic aberration in pulsed cavitational ultrasound therapy, or histotripsy, and to investigate the feasibility of conducting non-invasive histotripsy therapy without the use of aberration correction mechanisms in a variety of acoustically challenging therapeutic scenarios. To that end, this dissertation explores and discusses results from a series of *in vitro* and *in vivo* experimental studies to evaluate the robustness of histotripsy therapy in treatment situations highly likely to introduce severe acoustic aberration effects to the therapeutic ultrasound beam. Methods of avoiding or minimizing the consequences of acoustic aberration are also proposed by exploiting the unique characteristics of histotripsy therapy. Finally, recommendations for specific applications and future research are discussed.

This chapter will introduce the concept of acoustic aberration and its definition for the purposes of the work presented in this dissertation, followed by an overview of the techniques currently in use to reduce the effects of acoustic aberration in applications involving high intensity therapeutic ultrasound. Histotripsy therapy is introduced to provide sufficient background information on its basic mechanism of action and unique characteristics which will be referenced throughout the course of this work.

1.1 Sources of Acoustic Aberration in Ultrasound

In the scope of medical ultrasound, the term acoustic aberration has been traditionally applied to describe the defocusing effects arising from phase changes and attenuation imparted to the ultrasound wavefront due to the heterogeneous structure of the overlying tissue, a problem that has been extensively studied in the field of ultrasound imaging [1-9]. Because of its mechanical nature, ultrasound propagation is highly dependent on the material properties of the medium through which they traverse, and while the propagation speed of ultrasound in water is approximately 1482 m/s at 20 °C, the sound speed in different types of tissue may significantly vary, from 1430 m/s up to 1580 m/s [10, 11]. Harder materials such as bone tissue are known to have even higher sound speeds, in the range of 2500 m/s and above [12]. In diagnostic and therapeutic ultrasound applications that require focusing and steering capabilities, these variations in propagation speed can substantially alter the beam profile of the transducer at the focus if the waves do not arrive in phase, which can lead to arbitrary destructive and constructive interference patterns, compromising the spatial integrity of the focal beam.

While phase aberration is a major concern restricting proper ultrasound focusing, other acoustic propagation phenomena, such as non-uniform attenuation and diffraction effects can also be a significant cause of focal beam disruption. These effects can become more prominent in treatment situations where hard obstacles with inherently high degrees of attenuation or reflectivity (such as bone tissue or gas bodies) are present in the acoustic propagation field [13, 14]. By blocking a significant portion of the radiating aperture, these obstructions may change the sound field pattern of the transducer as received at the focal region, introducing undesirable distortions in the field. Furthermore, because of their high degree of echogenicity, such structures can also cause multiple scattering events, giving origin to additional interference patterns outside the intended focusing region. Such effects can further affect the quality of the ultrasonic beam, and consequently the resulting treatment.

For the purposes of this dissertation, the concept of acoustic aberration will be extended to include any phenomena that may significantly disrupt or alter the ultrasound pressure distribution profile in comparison to that generated in a homogeneous propagation medium (such as water). As the primary focus of this work revolves around therapeutic ultrasound applications, more specifically high power therapy for tissue ablation purposes, the discussion presented herein will concentrate on acoustic aberration effects as pertinent in the scope of high intensity therapeutic ultrasound.

1.2 Aberration Correction Techniques for Therapeutic Ultrasound

As research trends continue moving toward non-invasive clinical applications, substantial efforts have been dedicated in developing aberration correction techniques particularly tailored for therapeutic purposes. In the context of this work, it is appropriate to present an overview of the most established methods and algorithms developed for aberration correction in high intensity ultrasound therapy.

Currently, the majority of ultrasound tissue ablation procedures are based on thermal methods, requiring that a sufficient amount of heat be deposited at the treatment focus in order to cause cell necrosis in the targeted region. High intensity focused ultrasound (HIFU) has become a synonym with thermal ultrasound tissue ablation [15-17], in which the local temperature of the targeted tissue is raised rapidly (within seconds) in excess of 56º C [18]. In order to achieve such concentrated energy deposition, HIFU requires acoustic power levels 3-4 orders of magnitude greater than those used in typical diagnostic ultrasound imaging applications [19, 20]. The total thermal dosage is dependent on the intensity-time product of the ultrasonic exposure and in order to achieve effective treatment, the therapeutic ultrasound focus must be accurately controlled to minimize energy loss and collateral injury to overlying tissues.

However, in many non-invasive applications, the treatment may be susceptible to the formation of secondary lobes (such as side lobes and grating lobes) outside the main focus due to acoustic aberration effects, which can induce undesired damage at the locations where these secondary hotspots are formed, resulting in loss of treatment precision [21, 22]. The presence of acoustically reflective or absorbent interfaces such as bone tissue in the therapeutic window also needs to be carefully taken into consideration in order to avoid excessive thermal absorption, and subsequent damage at such boundaries [23-25]. Furthermore, in certain cases, frequency-dependent aberration effects may also broaden and distort the spatiotemporal shape of the focal main beam [26, 27], making aberration correction mechanisms a greater necessity to maintain therapeutic precision.

The simplest form of phase aberration correction for transducer arrays may be performed using a hydrophone or similar acoustic detector positioned at the focus of the treatment, across an aberrating region. Each element of the array is individually activated and the time delays from the elements are recorded. The element excitation timings can then be adjusted to compensate for the phase distortion induced by the aberrating layer, either by simple time of arrival calculations or by cross-correlation techniques. Hydrophone based methods are considered to be the gold standard for aberration correction, but the invasiveness of the measurement procedure limits its usefulness in most clinical applications.

In order to overcome this limitation and improve compatibility with non-invasive therapy applications, a large number of aberration correction schemes devised for therapeutic ultrasound purposes have been proposed over the years, resulting in a wealth of research papers on the subject and clearly demonstrating the interest and importance of addressing acoustic aberration effects in high intensity therapeutic ultrasound. Given the sheer number of different algorithms and techniques available in literature, it would be useful and convenient to categorize these studies for the purposes of this discussion. Though particular implementation methods may vary, the majority of current aberration correction techniques may be classified into two broad categories as a function of the mechanism through which acoustic inhomogeneities are evaluated or estimated: point-source detection methods and field map estimation methods.

Point-source detection methods have been initially studied for ultrasound imaging [28, 29] and require that transducer arrays possess both transmit and receive capabilities. The basic operation mechanism consists in the identification of an acoustic source or reflector at the focus of the treatment. Based on the echo signals received from this reference point, appropriate delays may be applied to the therapeutic waveform in order to compensate for the inhomogeneous nature of the medium. Improved levels of beam correction may be achieved if the acoustic waveform can be reconstructed and reverse-propagated by either phase conjugation [30, 31] or time-reversal techniques [32-35], which have also been shown to be effective in compensating for frequency-dependent attenuation effects. While naturally hyperechoic targets may be used as reference points in select cases, active sources or simple reflectors such as thermocouples may be required in many instances [36, 37]. More recently, however, studies have investigated the possibility of using droplet vaporization or inertial cavitation as potential non-invasive acoustic sources for aberration correction purposes with promising results [38-40].

Field mapping techniques for aberration correction have become more widely researched as imaging and computational technologies improved, allowing large simulations to be conducted within reasonable time frames for therapeutic applications. The principle behind this class of algorithms involves obtaining detailed information of the propagation medium *a priori*. Acoustic compensation is then performed based on the estimated speed of sound variations for different tissue layers, or from full wave propagation simulations, which may allow for more accurate distortion correction. Different imaging modalities have been investigated for this purpose; Magnetic resonance imaging (MRI) has been one of the most widely used techniques, applied for aberration correction purposes in transcostal, transabdominal and transcranial therapeutic scenarios [41-44]. Computerized tomography (CT) imaging has also been investigated for aberration correction, as proponents of this imaging modality point out that CT may be able to better differentiate subtle details in tissue composition such as the internal layers of the skull [45, 46]. Ultrasound imaging has been explored to a minor extent for treatment planning [47], possibly due to challenges involved in accurately capturing large 3D spatial volumes as required for optimal aberration correction using field mapping techniques. By their very nature, these estimation methods have the advantage of providing completely non-invasive aberration correction, although the degree of focal restoration may be limited by the resolution of the images that can be obtained before the treatment and the accuracy of the simulation parameters used for reconstruction. Depending on the application, field mapping techniques may also require considerably greater equipment and computational resources than point-source detection methods.

Aberration correction mechanisms for therapeutic ultrasound are under continuous investigation, with numerous research groups dedicating efforts to improve upon the state-of-the-art. While a significant amount of progress has been made in recent years in improving the accuracy and non-invasiveness of different aberration correction methods, a potential limitation of currently available algorithms is the requirement of a relatively static target, as beam path calculations are optimized for pre-selected focal locations, and target movement may render those estimates inaccurate. Because the number of elements in a transducer array used for aberration correction purposes may reach into the hundreds [48] or even thousands [49], the implementation of real-time aberration correction algorithms still remains a considerable technical and computational challenge. It would therefore be highly desirable to investigate additional therapeutic alternatives that could potentially be applied to cope with acoustic aberration effects in non-invasive ultrasound therapy.

1.3 Histotripsy Therapy

Histotripsy is a relatively novel high intensity ultrasound therapy modality that uses precise, highly energetic cavitation bubble clouds for mechanical tissue ablation [50, 51]. The rapid expansion and collapse of these bubble clouds effectively induce localized tissue liquefaction, resulting in the formation of tissue homogenate consisting of micron-sized acellular debris [52, 53]. Because of its unique ablation mechanism, histotripsy holds several benefits for therapeutic applications, such as the ability to actively remove tissue by fractionation and complete immunity to heat sink effects present in highly vascular tissues. In addition, the highly echogenic cavitation bubbles easily allow real-time treatment imaging with conventional ultrasound imaging systems [54]. Therapeutic progress can also be easily assessed in a similar manner, as tissue structures fractionated by histotripsy bubble clouds have been shown to display a substantial reduction in speckle intensity, allowing the operator to use standard B-mode ultrasound imaging to determine regions that have already been treated [55, 56]. Furthermore, in non-invasive treatment scenarios, the low therapeutic duty cycles used in histotripsy may help minimize the likelihood of inducing collateral heating effects on overlying tissues [57], which can be a concern when highly absorptive structures such as bones are present in the acoustic treatment window. Over the years, histotripsy therapy has been explored for a variety of applications, including treatments for congenital heart conditions [50], benign prostatic hyperplasia [58] , renal tumors [59], thrombosis [60] and kidney stones [61].

In recent studies, Maxwell et al. have demonstrated that the initiation of cavitation bubble clouds in histotripsy therapy is strongly dependent on the instantaneous peak rarefactional acoustic pressure available at the treatment target, allowing bubble clouds to be generated exclusively at focal locations where this pressure exceeds the cavitation bubble threshold of the medium. In these studies, two principal mechanisms have been identified to govern the initiation of dense cavitation bubble clouds in histotripsy therapy: High amplitude compressional shockwave scattering [62] and supra-intrinsic threshold rarefaction [63].

The shockwave scattering initiation mechanism involves highly non-linear pulses several cycles in length, typically > 3. Under this sonication regime, the initiation process takes place with the expansion of microbubbles by the initial rarefactional (negative) cycle of the incident wave, upon which the high amplitude shock front from an incoming compressional (positive) cycle is reflected. As the microbubbles present a pressure release boundary, the shockwave is inverted upon reflection, creating a large negative cycle that is backscattered and constructively interferes with the following negative cycle of the pulse, generating an additional layer of bubbles. This process repeats itself with subsequent cycles until the end of the pulse, generating a large bubble cloud expansion against the propagation direction of the wave. This multi-cycle shock scattering sonication method has been traditionally used for the majority of histotripsy studies to date.

The second mechanism of histotripsy bubble cloud initiation, supra-intrinsic threshold rarefaction, uses short, large peak negative pulses that exceed the “intrinsic” rarefactional cavitation threshold of the medium. In their study [63], Maxwell et al. defined this threshold as the peak negative pressure necessary to achieve a 50% probability of cavitation initiation using single pulses consisting of 2 cycles, which fell in the range of 26-30 MPa in samples with high water content. The use of extremely short pulses was noted to initiate more consistent bubble clouds, minimizing the effect of additional bubble cloud expansion due to shock scattering phenomena. This pulse strategy has only been explored very recently, as new improvements in transducer design and driver technology allowed the generation of the high peak rarefactional pressures required to enable the study of this bubble cloud initiation mechanism.

At this point, it is important to note that the cavitation thresholds of interest in this study refer to the pressure levels needed to initiate a dense cavitation bubble cloud at the focus of the treatment. Nucleation thresholds for isolated, single bubbles may be significantly lower than the pressure levels necessary to initiate and maintain a histotripsy bubble cloud; however, these isolated bubbles have been observed to possess a relatively negligible ablation potential in comparison to the highly energetic cavitation bubble clouds needed for effective tissue fractionation in histotripsy treatments. Therefore, for the purposes of this work, the term “cavitation threshold” will refer exclusively to cavitation bubble cloud initiation threshold as relevant for histotripsy treatments.

The unique characteristics of histotripsy represent a major paradigm shift in the field of high intensity ultrasound therapy, warranting a fresh approach in the evaluation of the therapeutic impact of acoustic aberration on this cavitation-based treatment modality. This was a motivation for the work presented herein, which aims to develop a body of knowledge concerning the effects of acoustic aberration specifically in the scope of non-invasive histotripsy therapy. Such an investigation would not only be of interest from the scientific standpoint, but would also have a direct impact on future clinical applications of this technique, aiding in the development of novel treatment strategies to address or circumvent various forms of acoustic aberration effects encountered in non-invasive treatment situations.

1.4 Outline of the Dissertation

This dissertation is organized in seven chapters presenting both *in vitro* and *in vivo* studies investigating the feasibility of using histotripsy therapy under diverse treatment scenarios likely to introduce significant degrees of acoustic aberration. Four chapters will discuss studies involving “traditional”, multi-cycle shock scattering histotripsy therapy while one chapter will explore the recently developed short pulse supra-intrinsic rarefaction sonication technique. More detailed descriptions for individual chapters are provided below.

Chapter 2 discusses the feasibility of using shock scattering histotripsy therapy through rib obstructions without using aberration correction, presenting *in vitro* experiments involving rib phantoms and excised rib sections. Chapter 3 extends this concept to study the application of transcostal histotripsy therapy in a porcine model *in vivo* by comparing treatments conducted through windows with and without full ribcage obstruction. Chapter 4 discusses the feasibility of using shock scattering histotripsy for *in vivo* non-invasive fetal surgery through complex treatment windows consisting of heterogeneous tissues. Chapter 5 presents a follow-up investigation on the acute and long-term safety aspects of the therapy in an ovine model. Chapter 6 investigates the feasibility and potential of using short pulse, supra-intrinsic threshold histotripsy therapy for non-invasive transcranial therapy applications. Finally, Chapter 7 provides a summary of the most important findings and conclusions from each study, with recommendations for further improvements and future research possibilities for histotripsy therapy in each of the application areas discussed in this work.

1.5 References

[1] P. W. Marcus and E. L. Carstensen, "Problems with absorption measurements of inhomogeneous solids," *Journal of the Acoustical Society of America,* vol. 58, pp. 1334-1335, 1975.

[2] S. W. Smith, G. E. Trahey, and O. T. von Ramm, "Phased array ultrasound imaging through planar tissue layers," *Ultrasound Med Biol,* vol. 12, pp. 229-43, Mar 1986.

[3] M. O'Donnell and S. W. Flax, "Phase aberration measurements in medical ultrasound: human studies," *Ultrason Imaging,* vol. 10, pp. 1-11, Jan 1988.

[4] L. Nock, G. E. Trahey, and S. W. Smith, "Phase aberration correction in medical ultrasound using speckle brightness as a quality factor," *J Acoust Soc Am,* vol. 85, pp. 1819-33, May 1989.

[5] D. Rachlin, "Direct estimation of aberrating delays in pulse-echo imaging systems," *J Acoust Soc Am,* vol. 88, pp. 191-8, Jul 1990.

[6] G. E. Trahey, P. D. Freiburger, L. F. Nock, and D. C. Sullivan, "In vivo measurements of ultrasonic beam distortion in the breast," *Ultrason Imaging,* vol. 13, pp. 71-90, Jan 1991.

[7] M. Karaman, A. Atalar, H. Koymen, and M. O'Donnell, "A phase aberration correction method for ultrasound imaging," *IEEE Trans Ultrason Ferroelectr Freq Control,* vol. 40, pp. 275-82, 1993.

[8] Y. Li, "Phase aberration correction using near-field signal redundancy. I. Principles [Ultrasound medical imaging]," *IEEE Trans Ultrason Ferroelectr Freq Control,* vol. 44, pp. 355-71, 1997.

[9] J. P. Fortes, "A closed loop ML algorithm for phase aberration correction in phased array imaging systems. I. Algorithm synthesis and experimental results [Ultrasound medical imaging]," *IEEE Trans Ultrason Ferroelectr Freq Control,* vol. 44, pp. 259-70, 1997.

[10] F. A. Duck, "Physical Properties of Tissue: A Comprehensive Reference Book," *Academic Press Limited, Academic Press. Inc.,* 1990.

[11] T. L. Szabo, "Diagnostic Ultrasound Imaging: Inside Out," *Academic Press Series in Biomedical Engineering, Elsevier Academic Press,* 2004.

[12] F. J. Fry and J. E. Barger, "Acoustical properties of the human skull," *J Acoust Soc Am,* vol. 63, pp. 1576-90, May 1978.

[13] J. E. Barger, "Attenuation and dispersion of ultrasound in cancellous bone," *Ultrasonic Tissue Characterization II,* vol. M. Linzer (ed.), NBS Spec. Publ. 525. US Govt. Printing Office, Washington, D.C., 1979.

[14] S. H. Hosseini, X. Zheng, and S. Vaezy, "Effects of gas pockets on high-intensity focused ultrasound field," *IEEE Trans Ultrason Ferroelectr Freq Control,* vol. 58, pp. 1203-10, Jun 2011.

[15] N. T. Sanghvi and R. H. Hawes, "High-intensity focused ultrasound," *Gastrointest Endosc Clin N Am,* vol. 4, pp. 383-95, Apr 1994.

[16] C. R. Hill, I. Rivens, M. G. Vaughan, and G. R. ter Haar, "Lesion development in focused ultrasound surgery: a general model," *Ultrasound Med Biol,* vol. 20, pp. 259-69, 1994.

[17] J. E. Kennedy, "High-intensity focused ultrasound in the treatment of solid tumours," *Nat Rev Cancer,* vol. 5, pp. 321-7, Apr 2005.

[18] G. ter Haar, "Therapeutic applications of ultrasound," *Prog Biophys Mol Biol,* vol. 93, pp. 111-29, Jan-Apr 2007.

[19] P. L. Carson, P. R. Fischella, and T. V. Oughton, "Ultrasonic power and intensities produced by diagnostic ultrasound equipment," *Ultrasound Med Biol,* vol. 3, pp. 341-50, 1978.

[20] M. S. Canney, M. R. Bailey, L. A. Crum, V. A. Khokhlova, and O. A. Sapozhnikov, "Acoustic characterization of high intensity focused ultrasound fields: a combined measurement and modeling approach," *J Acoust Soc Am,* vol. 124, pp. 2406-20, Oct 2008.

[21] J. Dupenloup, J. Y. Chapelon, D. Cathingnol, and O. A. Sapozhnikov, "Reduction of the grating lobes of annular arrays used in focused ultrasound surgery," *IEEE Trans Ultrason Ferroelectr Freq Control,* vol. 43, pp. 991-998, 1996.

[22] V. Khokhlova, S. Bobkova, and L. Gavrilov, "Focus splitting associated with propagation of focused ultrasound through the rib cage," *Acoustical Physics,* vol. 56, pp. 665-674, 2010.

[23] J. B. Marmor and G. M. Hahn, "Ultrasound heating in previously irradiated sites," *Int J Radiat Oncol Biol Phys,* vol. 4, pp. 1029-32, Nov-Dec 1978.

[24] J. E. Kennedy, F. Wu, G. R. ter Haar, F. V. Gleeson, R. R. Phillips, M. R. Middleton, and D. Cranston, "High-intensity focused ultrasound for the treatment of liver tumours," *Ultrasonics*, vol. 42, pp. 931-5, Apr 2004.

[25] M. Tanter, M. Pernot, J. F. Aubry, G. Montaldo, F. Marquet, and M. Fink, "Compensating for bone interfaces and respiratory motion in high-intensity focused ultrasound," *Int J Hyperthermia,* vol. 23, pp. 141-51, Mar 2007.

[26] M. Moshfeghi and R. C. Waag, "In vivo and in vitro ultrasound beam distortion measurements of a large aperture and a conventional aperture focussed transducer," *Ultrasound Med Biol,* vol. 14, pp. 415-28, 1988.

[27] T. Christopher, "Finite amplitude distortion-based inhomogeneous pulse echo ultrasonic imaging," *IEEE Trans Ultrason Ferroelectr Freq Control,* vol. 44, pp. 125-39, 1997.

[28] S. W. Flax and M. O'Donnell, "Phase-aberration correction using signals from point reflectors and diffuse scatterers: basic principles," *IEEE Trans Ultrason Ferroelectr Freq Control,* vol. 35, pp. 758-67, 1988.

[29] D. Zhao, L. N. Bohs, and G. E. Trahey, "Phase aberration correction using echo signals from moving targets. I: Description and theory," *Ultrason Imaging,* vol. 14, pp. 97-110, Apr 1992.

[30] W. Hong, E. S. Ebbini, M. O'Donnell, and C. A. Cain, "Phase aberration correction and motion compensation for ultrasonic hyperthermia phased arrays: experimental results," *Ultrasonics, Ferroelectrics and Frequency Control, IEEE Transactions on,* vol. 41, pp. 34-43, 1994.

[31] G. T. Clement, J. White, and K. Hynynen, "Investigation of a large-area phased array for focused ultrasound surgery through the skull," *Phys Med Biol,* vol. 45, pp. 1071-83, Apr 2000.

[32] F. Wu, J. L. Thomas, and M. Fink, "Time reversal of ultrasonic fields. Il. Experimental results," *IEEE Trans Ultrason Ferroelectr Freq Control,* vol. 39, pp. 567-78, 1992.

[33] J. L. Thomas, P. Roux, and M. Fink, "Inverse scattering analysis with an acoustic time-reversal mirror," *Phys Rev Lett,* vol. 72, pp. 637-640, Jan 31 1994.

[34] M. Tanter, J. L. Thomas, and M. Fink, "Time reversal and the inverse filter," *J Acoust Soc Am,* vol. 108, pp. 223-34, Jul 2000.

[35] Y. Jing, F. C. Meral, and G. T. Clement, "Time-reversal transcranial ultrasound beam focusing using a k-space method," *Phys Med Biol,* vol. 57, pp. 901-17, Feb 21 2012.

[36] J. L. Thomas and M. Fink, "Ultrasonic beam focusing through tissue inhomogeneities with a time reversal mirror: application to transskull therapy," *IEEE Trans Ultrason Ferroelectr Freq Control*, vol. 43, pp. 1122-1129, 1996.

[37] J. R. Ballard, A. J. Casper, Y. Wan, and E. S. Ebbini, "Adaptive transthoracic refocusing of dual-mode ultrasound arrays," *IEEE Trans Biomed Eng,* vol. 57, pp. 93-102, Jan 2010.

[38] O. D. Kripfgans, J. B. Fowlkes, M. Woydt, O. P. Eldevik, and P. L. Carson, "In vivo droplet vaporization for occlusion therapy and phase aberration correction," *IEEE Trans Ultrason Ferroelectr Freq Control,* vol. 49, pp. 726-38, Jun 2002.

[39] K. J. Haworth, J. B. Fowlkes, P. L. Carson, and O. D. Kripfgans, "Towards aberration correction of transcranial ultrasound using acoustic droplet vaporization," *Ultrasound Med Biol,* vol. 34, pp. 435-45, Mar 2008.

[40] J. Gateau, L. Marsac, M. Pernot, J. F. Aubry, M. Tanter, and M. Fink, "Transcranial ultrasonic therapy based on time reversal of acoustically induced cavitation bubble signature," *IEEE Trans Biomed Eng,* vol. 57, pp. 134-44, Jan 2010.

[41] J. Sun and K. Hynynen, "Focusing of therapeutic ultrasound through a human skull: a numerical study," *J Acoust Soc Am,* vol. 104, pp. 1705-15, Sep 1998.

[42] H. L. Liu, N. McDannold, and K. Hynynen, "Focal beam distortion and treatment planning in abdominal focused ultrasound surgery," *Med Phys,* vol. 32, pp. 1270-80, May 2005.

[43] A. Okada, T. Murakami, K. Mikami, H. Onishi, N. Tanigawa, T. Marukawa, and H. Nakamura, "A case of hepatocellular carcinoma treated by MR-guided focused ultrasound ablation with respiratory gating," *Magn Reson Med Sci,* vol. 5, pp. 167-71, Oct 2006.

[44] N. McDannold, G. T. Clement, P. Black, F. Jolesz, and K. Hynynen, "Transcranial magnetic resonance imaging- guided focused ultrasound surgery of brain tumors: initial findings in 3 patients," *Neurosurgery,* vol. 66, pp. 323-32; discussion 332, Feb 2010.

[45] J. F. Aubry, M. Tanter, M. Pernot, J. L. Thomas, and M. Fink, "Experimental demonstration of noninvasive transskull adaptive focusing based on prior computed tomography scans," *J Acoust Soc Am,* vol. 113, pp. 84-93, Jan 2003.

[46] F. Marquet, M. Pernot, J. F. Aubry, G. Montaldo, L. Marsac, M. Tanter, and M. Fink, "Non-invasive transcranial ultrasound therapy based on a 3D CT scan: protocol validation and in vitro results," *Phys Med Biol,* vol. 54, pp. 2597-613, May 7 2009.

[47] J. F. Aubry, M. Pernot, F. Marquet, M. Tanter, and M. Fink, "Transcostal high-intensity-focused ultrasound: ex vivo adaptive focusing feasibility study," *Phys Med Biol,* vol. 53, pp. 2937-51, Jun 7 2008.

[48] M. Pernot, J. F. Aubry, M. Tanter, J. L. Thomas, and M. Fink, "High power transcranial beam steering for ultrasonic brain therapy," *Phys Med Biol,* vol. 48, pp. 2577-89, Aug 21 2003.

[49] J. Song and K. Hynynen, "A 1372 element large scale hemispherical ultrasound phased array transducer for noninvasive transcranial therapy," *Proceedings of the 8th International Symposium on Therapeutic Ultrasound,* vol. 1113, pp. 377-381, 2008.

[50] Z. Xu, A. Ludomirsky, L. Y. Eun, T. L. Hall, B. C. Tran, J. B. Fowlkes, and C. A. Cain, "Controlled ultrasound tissue erosion," *IEEE Trans Ultrason Ferroelectr Freq Control,* vol. 51, pp. 726-36, Jun 2004.

[51] J. E. Parsons, C. A. Cain, G. D. Abrams, and J. B. Fowlkes, "Pulsed cavitational ultrasound therapy for controlled tissue homogenization," *Ultrasound Med Biol,* vol. 32, pp. 115-29, Jan 2006.

[52] Z. Xu, Z. Fan, T. L. Hall, F. Winterroth, J. B. Fowlkes, and C. A. Cain, "Size measurement of tissue debris particles generated from pulsed ultrasound cavitational therapy-histotripsy," *Ultrasound Med Biol,* vol. 35, pp. 245-55, Feb 2009.

[53] F. Winterroth, Z. Xu, T. Y. Wang, J. E. Wilkinson, J. B. Fowlkes, W. W. Roberts, and C. A. Cain, "Examining and analyzing subcellular morphology of renal tissue treated by histotripsy," *Ultrasound Med Biol,* vol. 37, pp. 78-86, Jan 2011.

[54] B. A. Rabkin, V. Zderic, and S. Vaezy, "Hyperecho in ultrasound images of HIFU therapy: involvement of cavitation," *Ultrasound Med Biol,* vol. 31, pp. 947-56, Jul 2005.

[55] T. L. Hall, J. B. Fowlkes, and C. A. Cain, "A real-time measure of cavitation induced tissue disruption by ultrasound imaging backscatter reduction," *IEEE Trans Ultrason Ferroelectr Freq Control,* vol. 54, pp. 569-75, Mar 2007.

[56] T. Y. Wang, Z. Xu, F. Winterroth, T. L. Hall, J. B. Fowlkes, E. D. Rothman, W. W. Roberts, and C. A. Cain, "Quantitative ultrasound backscatter for pulsed cavitational ultrasound therapy- histotripsy," *IEEE Trans Ultrason Ferroelectr Freq Control,* vol. 56, pp. 995-1005, May 2009.

[57] K. Kieran, T. L. Hall, J. E. Parsons, J. S. Wolf, Jr., J. B. Fowlkes, C. A. Cain, and W. W. Roberts, "Refining histotripsy: defining the parameter space for the creation of nonthermal lesions with high intensity, pulsed focused ultrasound of the in vitro kidney," *J Urol,* vol. 178, pp. 672-6, Aug 2007.

[58] A. M. Lake, T. L. Hall, K. Kieran, J. B. Fowlkes, C. A. Cain, and W. W. Roberts, "Histotripsy: minimally invasive technology for prostatic tissue ablation in an in vivo canine model," *Urology*, vol. 72, pp. 682-6, Sep 2008.

[59] N. R. Styn, J. C. Wheat, T. L. Hall, and W. W. Roberts, "Histotripsy of VX-2 tumor implanted in a renal rabbit model," *J Endourol*, vol. 24, pp. 1145-50, Jul 2010.

[60] A. D. Maxwell, G. Owens, H. S. Gurm, K. Ives, D. D. Myers, Jr., and Z. Xu, "Noninvasive treatment of deep venous thrombosis using pulsed ultrasound cavitation therapy (histotripsy) in a porcine model," *J Vasc Interv Radiol*, vol. 22, pp. 369-77, Mar 2011.

[61] A. P. Duryea, T. L. Hall, A. D. Maxwell, Z. Xu, C. A. Cain, and W. W. Roberts, "Histotripsy erosion of model urinary calculi," *J Endourol*, vol. 25, pp. 341-4, Feb 2011.

[62] A. D. Maxwell, T. Y. Wang, C. A. Cain, J. B. Fowlkes, O. A. Sapozhnikov, M. R. Bailey, and Z. Xu, "Cavitation clouds created by shock scattering from bubbles during histotripsy," *J Acoust Soc Am*, vol. 130, pp. 1888-98, Oct 2011.

[63] A. D. Maxwell, C. A. Cain, T. L. Hall, J. B. Fowlkes, and Z. Xu, "Probability of cavitation for single ultrasound pulses applied to tissues and tissue-mimicking materials," *Ultrasound Med Biol*, vol. 39, pp. 449-65, Mar 2013.

Chapter 2

Transcostal Histotripsy Therapy

This chapter presents an investigation on the feasibility of conducting transcostal histotripsy therapy without using aberration correction. Acoustic aberration effects of periodic rib obstruction in the acoustic window are examined and the pressure threshold mechanism of cavitation bubble cloud initiation is investigated to evaluate the robustness of histotripsy therapy against distortion effects induced by the rib aberrators. Histotripsy lesion patterns are generated with and without the presence rib obstacles without aberration correction in order to quantify the ablation precision of the therapy and the extent of collateral damage induced in the treatment region.

2.1 Introduction

The effects of acoustic obstruction from rib bones have long been a challenge to researchers in high intensity focused ultrasound (HIFU). In several non-invasive surgery applications, such as treatment for liver and pancreatic cancer, it is often the case that the available acoustic windows are partially blocked by the ribs, which can substantially decrease the ultrasound energy delivery to the focal target and may overheat overlying tissues due to the highly absorptive nature of bones [1-4]. Furthermore, ribs can cause significant field aberration, resulting in increased secondary lobes and reduced main lobe intensities in the beam profile which may cause undesired collateral damage.

To overcome these issues, significant efforts have been dedicated to develop aberration correction algorithms in order to spare the ribs and improve beam forming. Theoretical studies on the application of virtual phased arrays to sonicate between the rib bones have been conducted [5]; a physically segmented transducer design was also proposed to prevent sonication to the ribs by aligning active elements with the intercostal gaps [6]. More recently, adaptive focal optimization algorithms for transcostal therapy have been developed, depending on the presence of a point source or an identifiable acoustic spot at the desired focus [7, 8]. More sophisticated non-invasive approaches using ultrasound scanning and time-reversal to identify the ribs [9] require transducers with transmit and receive capabilities. Other non-invasive methods explored involve the use of CT or MRI [10, 11] to image the rib obstructions and selectively deactivate elements shadowed by the rib bones.

Even if the ribs are spared, another potential issue is the formation of strong grating lobes at the focal profile due to the spatial distribution of the ribs. This “focal splitting” effect has been described and characterized more analytically in a recent study , which shows that grating lobes may still be present in the focal profile even after correction algorithms are applied due to the periodic ultrasound blockage pattern caused by the ribs [12].

This study presents an investigation on the feasibility of using histotripsy therapy to generate lesions through rib aberrators without applying any correction mechanisms other than transducer power modulation to compensate for attenuation effects. The tissue fractionation effect from histotripsy therapy occurs when the focal pressure exceeds a certain threshold level at which a cavitation bubble cloud is initiated [13-15]. Based on this threshold mechanism, it is hypothesized that histotripsy therapy can generate precise lesions through the ribs, provided that the pressure main lobe maintains its shape and exceeds the bubble cloud initiation threshold while secondary lobes are below the threshold (Figure 2.1). No bubble clouds are generated in regions that are below the initiation threshold, resulting in minimal collateral damage to regions surrounding the main lesion.

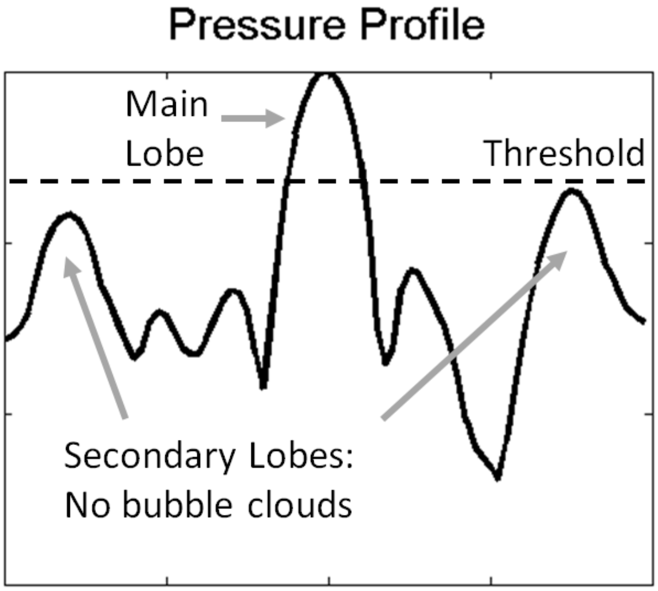

Figure 2.1. Illustration of the cavitation threshold effect in histotripsy therapy: By modulating the acoustic power in such a way that only the main lobe exceeds the bubble cloud initiation threshold, confined focal lesions with minimal collateral damage should be generated at the treatment focus.

To test this hypothesis, histotripsy treatment was applied to tissue-mimicking gel phantoms in free field and through rib aberrators at similar rarefactional focal pressures and identical treatment settings without using aberration correction. The bubble cloud generated was monitored for cases with and without the rib aberrators, and resulting lesions were compared for overall dimensions and presence of collateral damage caused by secondary lobes.

2.2 Methods

A 750 kHz, 18 channel spherically focused transducer (IMASONIC, Voray sur l'Ognon, France) was used in this study. The transducer has a geometric focal length of 12 cm, with an aperture size of 15 cm (f# 0.8) and a center hole of 5.9 cm in diameter designed to accommodate an ultrasound imaging probe (not used in this study). All 18 elements were driven in phase through a custom-designed 18 channel switching amplifier unit with appropriate electrical matching circuits built in house. Input signal controls were provided by a Field-Programmable Gate Array (FPGA) board (Altera Corporation, San Jose, CA, USA) that functioned as a custom signal generator.

A rib phantom made of polycarbonate rods was constructed to emulate acoustic aberration conditions typically caused by rib bones. The rods had a diameter of 13 mm and were separated by 25 – 30 mm, which are comparable to the sizes and intercostal separations in the human ribcage. In addition to the polycarbonate rib phantom, excised ribcage sections from adult pigs were also used for further validation. Both the phantom and the rib sections were positioned between the transducer and its geometric focus inside a tank filled with degassed water. Porcine rib sections were immersed in a thin plastic bag with 0.9% saline, and then submerged in the tank. An illustration of the experiment setup is given in (Figure 2.2).

A high-sensitivity needle hydrophone (HNR-0500 Onda Corporation, Sunnyvale CA, USA) was used to scan focal pressure profiles with and without the rib aberrators. Pressure profiles were obtained for each of the situations considered in this study: in free field, with the rib phantom positioned at 8 cm and 4 cm from the focus, and with porcine ribs at 8 cm from the focus. The porcine rib section was placed in an acoustically transparent plastic bag filled with saline, which limited its placement to 8 cm from the focus to avoid contact of the bag with the hydrophone probe. At the focus, high pressure shockwave measurements were conducted using a multimode fiber optic hydrophone system designed and built in-house [16]. Based on these high pressure measurements, the peak rarefactional pressure was controlled so that it would be approximately equal at the focus for all treatments.

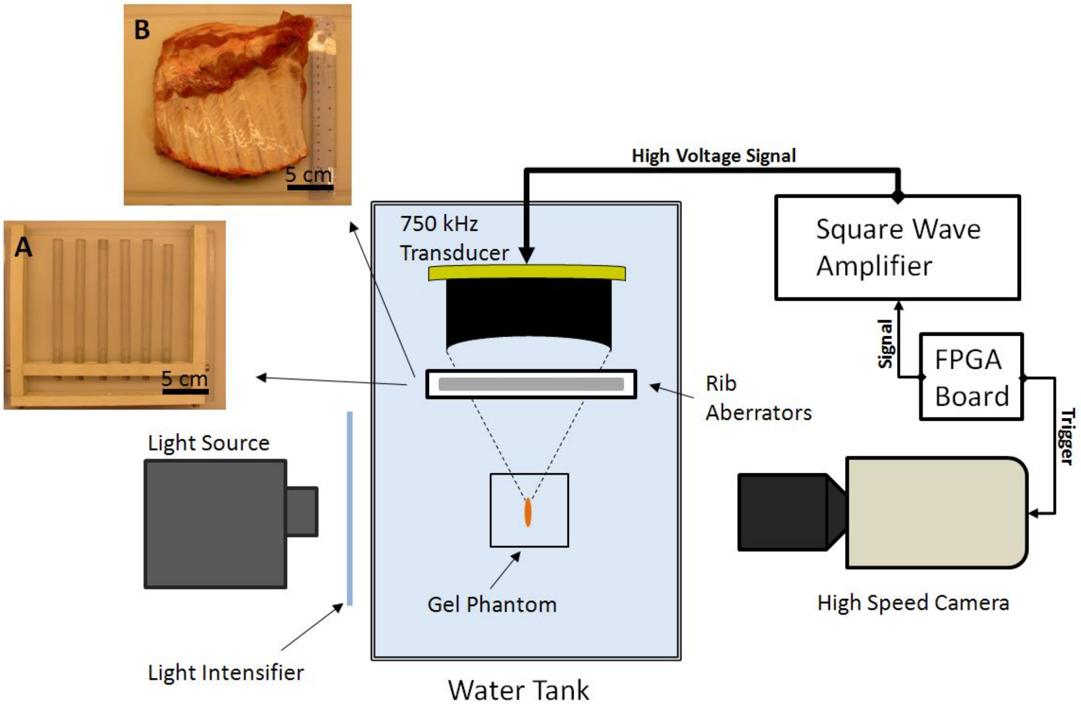

Figure 2.2. Illustration of the experimental setup for bubble cloud imaging with pictures of the rib aberrators: (A) Polycarbonate rib phantom. (B) Porcine rib section.

2.2.1 Bubble Cloud Imaging Setup

A high-speed, 1 megapixel CCD camera, (Phantom V210 - Vision Research, Wayne, New Jersey, USA) was used to capture bubble cloud images in transparent 1% agarose gel phantoms with and without the rib aberrators. The camera was triggered through the same FPGA signal generator driving the transducer's amplifier system. Images of the bubble cloud were collected at set delay of 12 µs after each pulse's arrival at the transducer's geometric focus, with one frame (1280 × 800 pixels) captured every 10 treatment pulses (800 frames captured per treatment). A back-lit setup was used with a halogen light source, intensified with fresnel lens sheets. An adjustable camera lens (AF Nikkor 70-210 mm f/4-5.6, Nikon, Tokyo, Japan) coupled with magnifying lenses allowed an image resolution of 40 pixels/mm. To achieve satisfactory background illumination through the gel phantom, frame exposure times were set at 4 µs.

2.2.2 Red Blood Cell Phantom Treatment

Tissue-mimicking red blood cell (RBC) agarose phantoms developed in house were used to assess the extent of the fractionation produced with and without the presence of the rib aberrators. The base composition of the gel phantom was made by mixing agarose power and saline (0.9%) at a ratio of 1% of agarose to saline by weight. Structurally, the phantoms consisted of three layers, with the top and bottom layers (2-2.5 cm thickness) acting as buffer zones between the water in the tank and the middle (RBC) layer (approximately 0.5 – 1.5 mm in thickness), in which canine RBCs (5% concentration by volume) were added. The phantom has been successfully used as an indicator of cavitational damage caused by histotripsy in tissue [17]. The opaque, intact RBC layer in the phantom becomes translucent once the cells in the layer are fractionated by cavitation (Figure 2.3A). The major advantage of using RBC phantoms over tissue is that cell fractionation patterns caused by histotripsy treatment can be visualized directly in different planes without time-consuming histopathological analysis.

Treatment was administered through the rib aberrators by driving the transducer in such a way that the peak rarefactional pressure at the focus was equivalent to that applied in free field treatments. For each case, treatment pulses were applied at a pulse repetition frequency (PRF) of 100 Hz and 5 cycles per pulse. A total of 8000 pulses were applied per treatment (80 s) to ensure complete fractionation of the targeted volume. Lesion profiles were created along the transversal and longitudinal focal planes by appropriately positioning the RBC layer at the focal zone. For transversal lesions, the RBC layer was positioned perpendicularly with respect to the axis of the transducer. Longitudinal plane lesions were generated by positioning the RBC layer at the focus, parallel to the axis of the transducer.

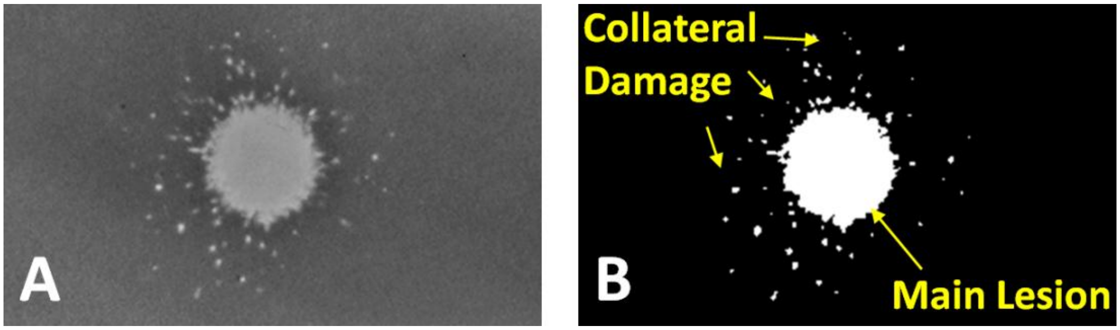

Figure 2.3. (A) Sample picture of a treated RBC phantom showing a translucent lesion. (B) Processed image sample for lesion size and collateral damage assessment. Collateral damage appears as small translucent spots surrounding the main lesion area.

Lesion sizes and collateral damage distribution were assessed with the aid of an image analysis script written in-house [18]. The script allows image binarization into fractionated and intact areas, with fractionated areas defined as zones with pixel intensities three standard deviations higher than the chosen background, typically the space-averaged intensity of pixels from a sample area on the intact blood layer. Once the image is binarized, lesion dimensions are then estimated by a pixel count. For this study's purpose, the continuous translucent area extending from the center of the main lobe location was defined as the main lesion, and collateral damage was defined as the remaining damage spots found outside the main lesion (Figure 2.3B).

2.3 Results

2.3.1 Acoustic Pressure Profile

Without applying power compensation, the presence of the rib aberrators substantially reduced the peak rarefactional pressure amplitude at the focus in comparison to free field measurements. Pressure insertion losses were approximately -5.5 dB through the rib phantom and up to -7 dB through the porcine ribs. High levels of secondary (grating) lobes were introduced in the focal profile along the transversal axis perpendicular to the orientation of the rib obstacles. No significant secondary lobe development was observed in the transversal axis parallel to the orientation of the obstacles or along the longitudinal axis of propagation. The highest secondary lobes were in the range of -7 dB to -4 dB normalized to their respective main lobes; -7 dB with porcine ribs and -4 dB with the rib phantom positioned at 4 cm from the focus (Figure

2.4). The location of the secondary lobes varied from 5-8 mm with respect to the center of the main lobe, developing closer to the center when the rib obstacles were placed farther away from the transducer (closer to the focus).

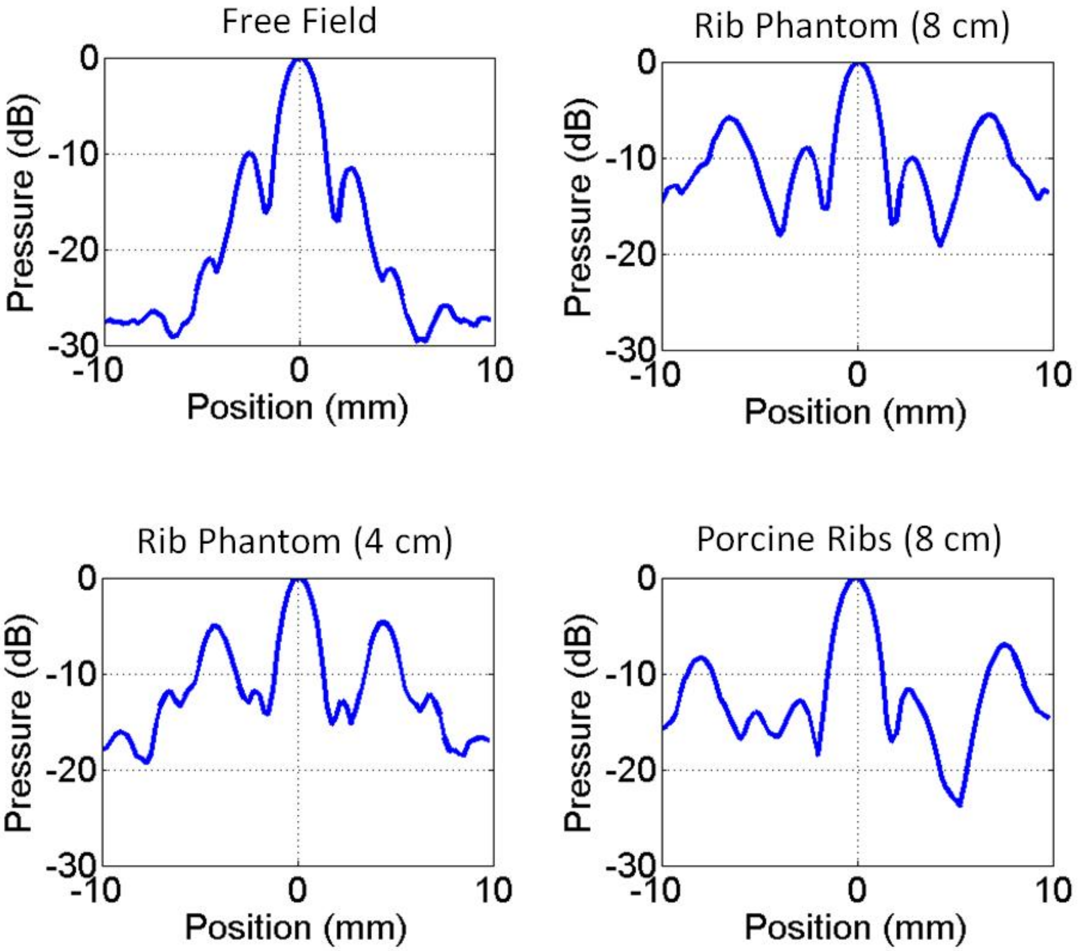

Figure 2.4. Normalized transversal focal pressure profiles obtained in free field and through the rib aberrators. Secondary lobes were not observed to develop in the longitudinal axis or the transversal axis parallel to the orientation of the rib obstacles. “Rib Phantom (8 cm)” indicates that the rib phantom was placed between the transducer and the focus, 8 cm away from the focus. Scan profiles reference peak rarefactional values at each location.

In comparison to free field measurements, the main lobe did not undergo any noticeable shift in the transversal or longitudinal coordinates in the presence of the rib phantom. In scans involving the porcine ribs, the main lobe was shifted closer towards the transducer by approximately 3 mm, but no significant transversal shifts were observed. Despite the presence of high secondary lobes, the main lobe remained undistorted in all cases.

The measured minimum focal pressure threshold to initiate and maintain a cavitation bubble cloud in degassed water (40~45% dissolved O_2) under free field conditions was approximately at a peak rarefactional pressure of 16 MPa and a peak compressional pressure of 60 MPa (with 5 cycle pulses delivered at a 100 Hz repetition rate). Because of the significant insertion losses measured in the presence of the rib aberrators, the transducer power was appropriately increased to compensate for the attenuation and approximately equalize peak rarefactional pressure levels at the focus, which were within the range of 16-18 MPa (Figure 2.5**)**.

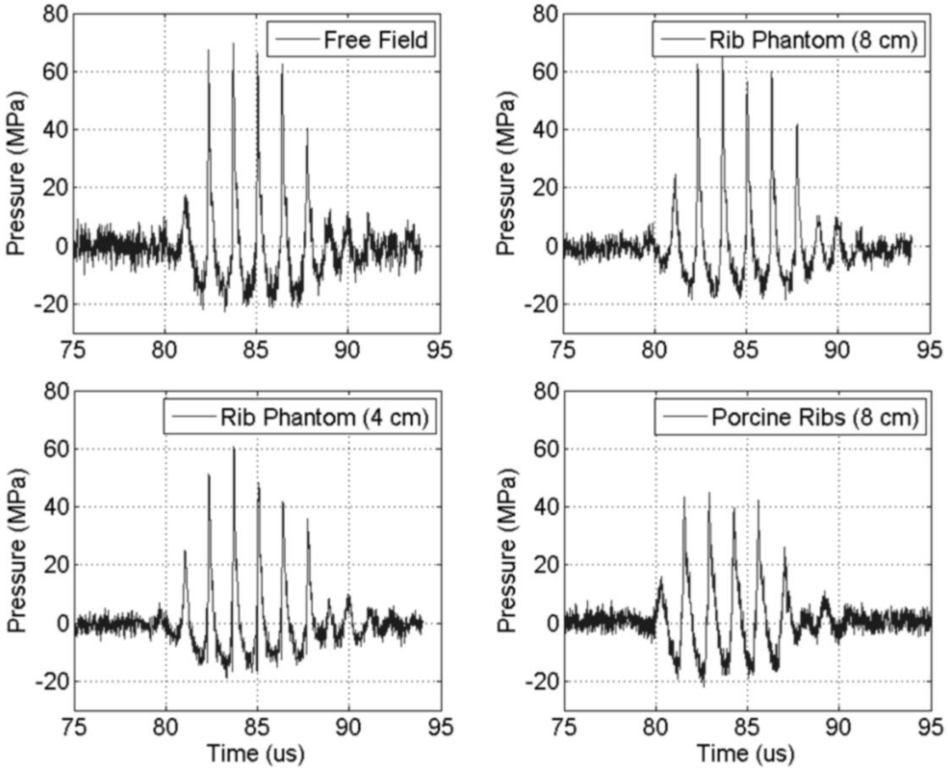

Figure 2.5. Treatment pulse waveforms measured in free field and through the rib aberrators. Measurements were taken at the geometric focus of the transducer.

2.3.2 Bubble Cloud Imaging

Cavitation bubble clouds of comparable sizes were successfully developed at the focus in all cases, with and without the rib aberrators. In the initial stages of the treatment, large bubbles were observed to form at the main lobe location within the first few pulses. These cavitation bubbles eventually formed a larger cigar-shaped bubble cloud at the location of the main lobe as the gel was fractionated (Figure 2.6). In the clear agarose gels, consistent bubble clouds were observed through all cases, with dimensions corresponding to approximately 3 x 12 mm.

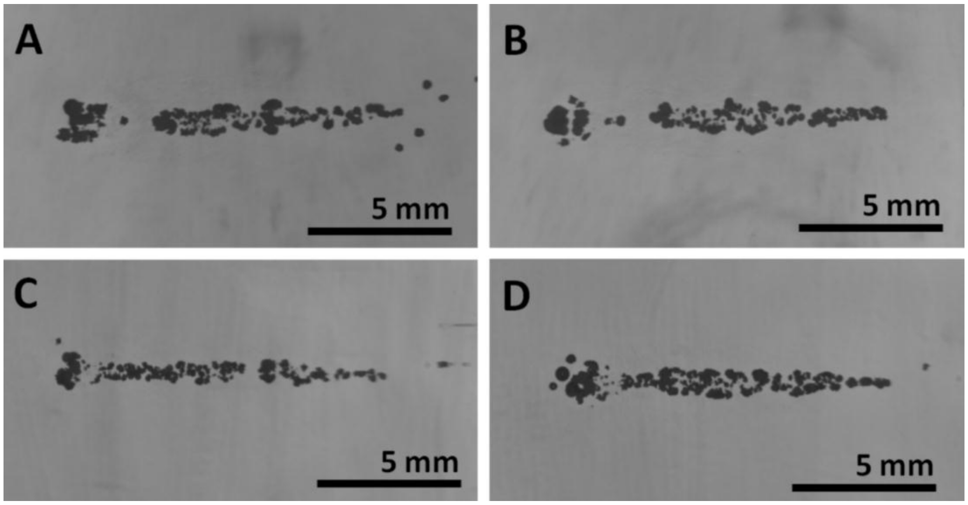

Figure 2.6. High-speed images of bubble clouds (shown as the dark clusters of dots) generated in a transparent agarose phantom. (A) In free field; (B) with the rib phantom at 8 cm; (C) with the rib phantom at 4 cm; (D) with the porcine ribs at 8 cm. Longitudinal planes are shown. Ultrasound propagation: left to right.

The treatment progression in the RBC phantoms was also monitored optically. In the presence of the rib obstacles, small cavitation nuclei were observed near locations where the secondary lobes were the highest. However, as treatment progressed, these marginal bubbles did not become part of a cloud and were pushed away by radiation force, eventually collapsing on their own within the first 1000 to 2000 pulses and preventing further damage to be generated on the RBC layer.

2.3.3 Lesion Analysis

Lesions were successfully created at the focus of the transducer in all cases. A total of 87 lesions were created in RBC phantoms: 22 reference lesions were generated under free field conditions, 45 lesions were created through the polycarbonate rib phantom and 20 lesions through the porcine ribs. Morphology of representative transversal plane lesions is shown in Figure 2.7. A circular main lesion was observed in all treatment cases, with collateral damage occurring in the form of a few sporadic points within a ring shaped zone around the main lesion area. In treatments through the rib aberrators, minor damage spots were observed at the locations where the secondary lobes were the highest, but no significant fractionation areas were observed outside the main lesion.

To evaluate the longitudinal plane lesion profiles, the RBC tissue phantom was positioned in such a way that the RBC layer was perpendicular with respect to the orientation of the rib obstacles to ensure that the layer coincided with the plane where the secondary lobes were present. A cigar shaped main lesion was created in all treatments, with incompletely fractionated areas in the form of thin damage streaks at the tail of the main lesion (Figure 2.8). Lesions generated through the rib aberrators also displayed damage streaks on both sides of the main lesion, consistent with locations where the temporary marginal nuclei were observed during the high-speed camera imaging. But as with the transversal plane treatments, no significant lesion development occurred outside the main lobe region.

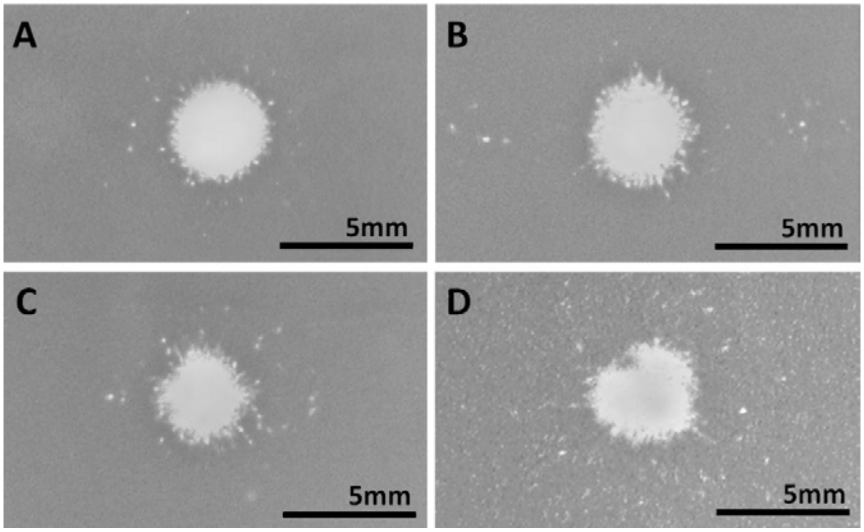

Figure 2.7. Transversal lesion patterns: (A) in free field; (B) with the rib phantom positioned at 8 cm from the focus; (C) with the rib phantom at 4 cm; (D) with porcine ribs at 8 cm. Lesions correspond to the visually clear areas surrounded by the darker background color of the RBC layer. Collateral damage was defined as the sum of all damage spots detected outside of the continuous portion of the main lesion.

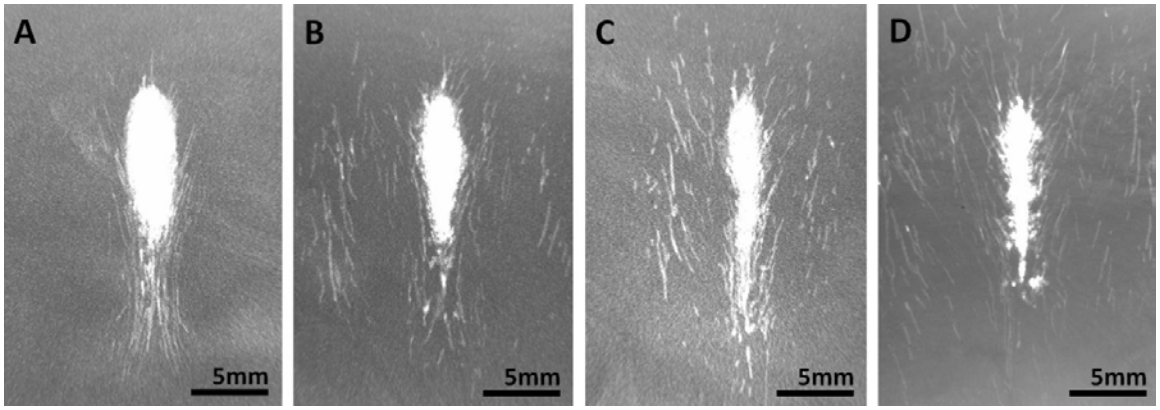

Figure 2.8. Representative longitudinal plane lesions: (A) in free field; (B) with the rib phantom at 8 cm; (C) with the rib phantom at 4 cm; (D) with porcine ribs at 8 cm. The trailing paths created by the translation of marginal bubble nuclei were the cause of most of the collateral effects seen in the longitudinal plane. Ultrasound propagation: top to bottom.

In a more quantitative point of view, the focal lesion areas generated through the rib aberrators were comparable to within a standard deviation of the lesion areas created in free field, although the mean lesion sizes generated through the aberrators were slightly smaller (Figure 2.9). Considering mean lesion dimensions in both transversal and longitudinal planes, the largest lesions were generated in free field conditions while the smallest lesions were obtained through the porcine ribs.

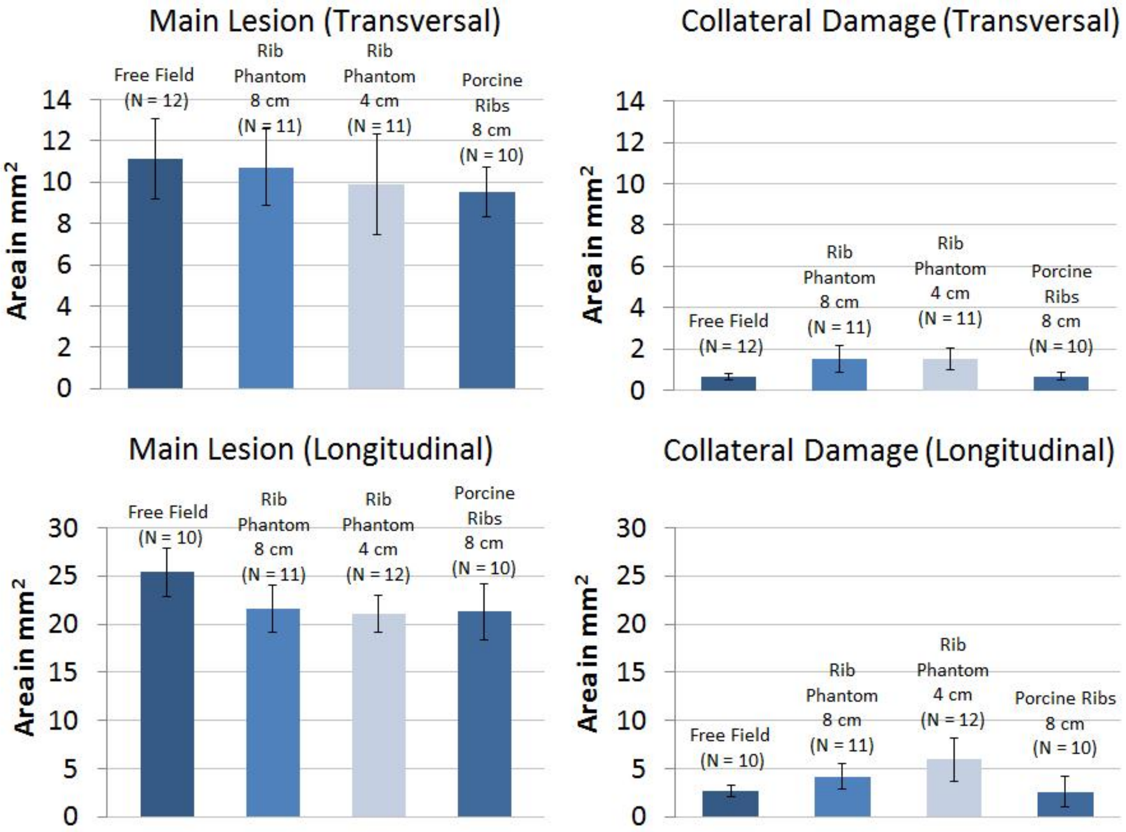

Figure 2.9. Main lesion dimensions and collateral damage on the transversal and longitudinal plane lesions generated in free field and through the rib aberrators. Error bars correspond to plus or minus one standard deviation for each dataset.

The collateral damage created through the porcine ribs was minimal and not statistically significant in comparison to that observed in free field lesions (Transversal:

N=10 / p-value = 0.92; Longitudinal: N = 10 / p-value = 0.7). Higher levels of collateral damage from marginal bubble nuclei were observed in lesions created through the rib phantom, particularly when the phantom was placed closer to the focus (at 4 cm).

In actual treatment scenarios, it is likely that a region larger than a single focal size will need to be ablated. Lesions consisting of 5 focal spots separated by 1 mm were created by mechanically scanning the transducer to examine the feasibility of generating composite lesions through the ribs (Figure 2.10). As with the single focus treatments, comparable fractionated areas were created in all cases; lesion development was well confined and limited to the focal zone while collateral damage from secondary lobes consisted of thin streaks caused by the translation of marginal bubble nuclei.

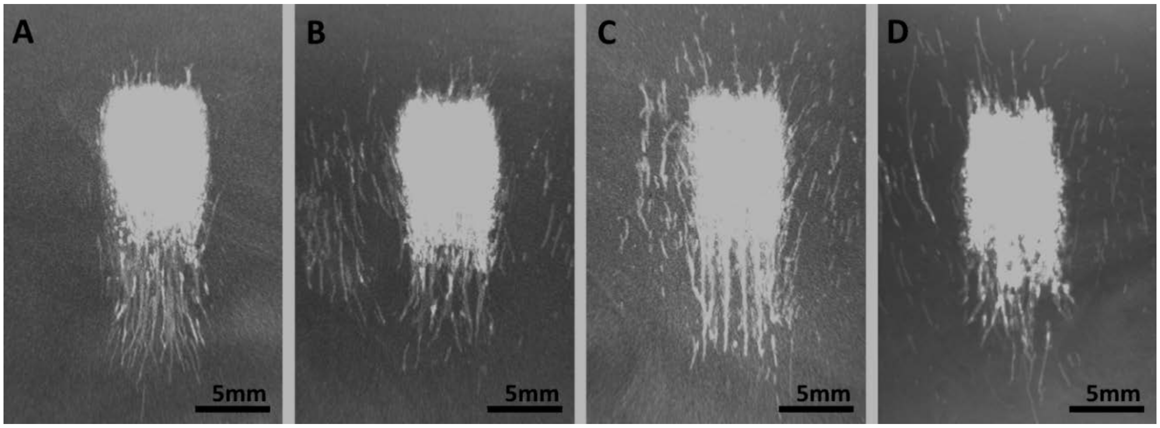

Figure 2.10. Lesions created by applying 5 adjacent treatments separated by 1 mm, covering a total zone of approximately 7 x 10 mm. (A) in free field; (B) with the rib phantom at 8 cm; (C) with the rib phantom at 4 cm; (D) with porcine ribs at 8 cm. Ultrasound propagation: top to bottom.

2.4 Discussion

The rib aberrators significantly distorted the focal profile in the form of increased secondary lobes at the expense of reduced main lobe intensities in comparison to free field measurements. In this case, the formation of secondary lobes is primarily a consequence of the distribution of the solid bone obstacles in the ribs, which together act as an acoustically diffractive mask, effectively creating an aperture with active elements radiating from the intercostal separations between the solid obstacles. It has been shown theoretically [19] that while the relative location of these secondary lobes (in this case grating lobes) may change depending on the spatial pattern of the distribution of the rib bones, the main lobe should remain relatively undistorted if a reasonably large transducer aperture is used. This is consistent with measurements, as the main lobe profile did not appear to be appreciably changed (except for attenuation effects) with the introduction of the rib aberrators. Other forms of acoustic aberration may affect the beam profiles similarly [20] so that this method may be relevant to other situations where acoustic aberration effects limit therapeutic options, e.g.: the skull.

It was hypothesized that histotripsy therapy could be used to generate precise lesions through the ribs, as long as the focal main lobe maintains its shape and exceeds the cavitation cloud initiation threshold while secondary lobes are below the threshold. Supporting this premise, cavitation bubble clouds of similar sizes were generated through the ribs, and despite the high secondary lobes introduced by the rib aberrators, the formation of a bubble cloud was limited to the main lobe, which was also the only location where a full lesion successfully developed. Temporary cavitation bubbles were observed to form at the locations of secondary lobes during the initial stages of treatment through the rib aberrators, but these bubbles did not form a cloud, eventually collapsing on their own, pushed away by radiation force. This is evidenced by the collateral damage patterns observed in the RBC phantoms, which consisted of peripheral spots or streaks not comparable to the central main lesion.

It is interesting to note that the secondary lobe levels measured through the porcine ribs were lower relative to those measured through the polycarbonate rib phantom. One plausible explanation is that the more uniform geometry of the phantom created better conditions for the formation of secondary lobes at the focal profile in comparison to the relatively randomly shaped and spaced porcine ribs. As a consequence, lesions created through the porcine ribs were more confined, presenting minimal collateral damage in comparison to lesions generated in free field. In clinical applications requiring a larger volume to be ablated, lesions with multiple foci could be generated by mechanically sweeping the focus of the transducer (as shown in this study) or by electronic focal steering if a phase array is used. As ablated regions increase in size, it is expected that the collateral damage caused by secondary lobes would become even less relevant relative to the total size of the lesion.

Although the main lesion dimensions generated with and without the rib aberrators were comparable when accounting standard deviation ranges, the mean area of lesions obtained through the rib aberrators was smaller relative to free field lesions, a result that may seem counter-intuitive since similar treatment parameters were used. It should be pointed out, however, that while all lesions were generated at comparable focal peak rarefactional pressure levels, (16-18 MPa) peak compressional pressures were observed to vary more significantly, with measurements differing by as much as 25 MPa in comparison to free field.

Peak rarefactional pressure measurements have been commonly reported in literature as thresholds for cavitation events [21-23], but as previously discussed in Chapter 1, the bubble cloud initiation process using histotripsy pulses consisting of multiple, highly non-linear cycles is likely to be dependent on the shock scattering phenomena described by Maxwell et al. [24], giving peak compressional pressures (higher pressure harmonics) a significant role in this process. It is possible that the attenuation of these higher pressure harmonics may have affected the cavitation dynamics at the focus, resulting in the formation of smaller lesions in the presence of the rib aberrators. This correlates with the observation that the smallest lesions were generated through the porcine ribs and through the rib phantom positioned at 4 cm from the focus, which were also the configurations that most attenuated the focal peak compressional pressure levels.

From this perspective, it is noticeable that the peak compressional pressure measured through the porcine ribs was considerably lower than its counterparts in free field and through the polycarbonate rib phantom (up to 35%), but no comparable reduction in the sizes of the bubble clouds or lesions were observed. In this particular case, the peak compressional pressure may have been underestimated because the focal pressure measurements were taken at the geometric focus of the transducer. As previously noted, the porcine ribs introduced a small axial shift (3 mm) in the focal profile. Since the higher harmonic components of a shockwave have much tighter focusing characteristics than the fundamental, the focal shift may have significantly lowered the peak compressional pressure amplitude measured at the geometric focus of the transducer.

While cavitation threshold pressures cannot be easily measured *in vivo*, histotripsy therapy at or near bubble cloud threshold levels is still feasible since cavitation bubble clouds can be readily monitored using conventional ultrasound imagers, allowing the operator to be aware of when and where the threshold has been reached anywhere within a given region of interest. In an *in vivo* scenario, the operator would start the treatment from low acoustic power settings and gradually increase power levels until a cavitation bubble cloud is imaged at the focal spot. Once a bubble cloud is created at the focus, treatment could then proceed at that level, confining the bubble cloud to the location of the main lobe and preventing secondary lobes from reaching the cavitation threshold. This provides direct imaging feedback to validate the location of the tissue ablating bubble cloud.

In addition, because cavitation bubble clouds can be initiated at arbitrarily low duty cycles — even single pulses — as long as enough pressure is available at the focus, the likelihood of inducing thermal effects in overlying tissues can be drastically reduced with the pulsed ultrasound parameters used in histotripsy therapy. In this study for example, the effective sonication duty cycle applied to achieve a bubble cloud was less than 0.07% in all treatments, which is virtually negligible in terms of HIFU therapy standards. This could potentially allow transcostal therapy to be performed by simple single element transducers with minimal thermal effects on the ribs, without requiring phased array designs to sonicate between the intercostal spaces. Thus, with a sufficiently powerful transducer, compensation of the main lobe pressure to counteract attenuation could be accomplished without significant thermal consequences to overlying tissues at the expense of reduced duty cycle, and perhaps, treatment time.

While in this study histotripsy therapy was applied to create lesions through rib obstacles without any compensation methods other than power modulation, aberration correction mechanisms may be beneficial to help improve focusing and increase treatment efficiency, especially when severe phase aberration is present. Potential sources of phase aberration are multiple layers of thick inhomogeneous tissue, which could significantly distort the main lobe and prevent the initiation of a cavitation bubble cloud at the focus. Since it is only necessary to move the peak pressure of the focal main lobe beyond the bubble cloud cavitation threshold and above all secondary lobes, relatively coarse aberration correction schemes could potentially be applied to appropriately accentuate the main lobe, if necessary. Future studies will explore how such inhomogeneous tissue may affect histotripsy therapy, followed by an investigation of possible methods to circumvent aberration effects and improve the efficacy of the treatment.

This study evaluated the feasibility of using histotripsy therapy to generate lesions through rib obstacles without using aberration correction mechanisms. It was hypothesized that precise lesions can be generated through ribs by histotripsy therapy without aberration correction as long as the pressure main lobe maintains its shape and exceeds the cavitation cloud initiation threshold while secondary lobes are below the threshold. The rib aberrators significantly attenuated the peak focal pressure and introduced high secondary lobes in the focal profile. Treatment was conducted by adjusting the input voltage of the transducer such that the peak rarefactional pressures at the focus were at similar levels to free field conditions. Despite the presence of significant secondary lobes, cavitation bubble clouds were observed to develop exclusively at the main lobe locations, resulting in lesions that were comparable in size to those created under free field conditions. Collateral damage from secondary lobes was limited to damage spots caused by temporary cavitation bubbles that failed to form a cloud.

The threshold nature of the bubble cloud initiation in histotripsy therapy appears to confer a high degree of robustness to the bubble cloud shape in the presence of secondary lobes introduced by rib aberrators. This characteristic, coupled with the non-thermal nature of the treatment, suggest that histotripsy therapy could be a useful non-invasive tissue ablation modality for transcostal surgical applications such as treatment for hepatic and pancreatic cancer, or for cardiac ablation procedures.

2.5 References

[1] S. E. Jung, S. H. Cho, J. H. Jang, and J. Y. Han, "High-intensity focused ultrasound ablation in hepatic and pancreatic cancer: complications," *Abdom Imaging,* May 29 2010.

[2] J. J. Li, G. L. Xu, M. F. Gu, G. Y. Luo, Z. Rong, P. H. Wu, and J. C. Xia, "Complications of high intensity focused ultrasound in patients with recurrent and metastatic abdominal tumors," *World J Gastroenterol,* vol. 13, pp. 2747-51, May 21 2007.

[3] F. Wu, Z. B. Wang, W. Z. Chen, W. Wang, Y. Gui, M. Zhang, G. Zheng, Y. Zhou, G. Xu, M. Li, C. Zhang, H. Ye, and R. Feng, "Extracorporeal high intensity focused ultrasound ablation in the treatment of 1038 patients with solid carcinomas in China: an overview," *Ultrason Sonochem,* vol. 11, pp. 149-54, May 2004.

[4] J. E. Kennedy, F. Wu, G. R. ter Haar, F. V. Gleeson, R. R. Phillips, M. R. Middleton, and D. Cranston, "High-intensity focused ultrasound for the treatment of liver tumours," *Ultrasonics,* vol. 42, pp. 931-5, Apr 2004.

[5] Y. Y. Botros, E. S. Ebbini, and J. L. Volakis, "Two-step hybrid virtual array ray (VAR) technique for focusing through the rib cage," *Ultrasonics, Ferroelectrics and Frequency Control, IEEE Transactions on*, vol. 45, pp. 989-1000, 1998.

[6] J. Civale, R. Clarke, I. Rivens, and G. ter Haar, "The use of a segmented transducer for rib sparing in HIFU treatments," *Ultrasound Med Biol,* vol. 32, pp. 1753-61, Nov 2006.

[7] J. R. Ballard, A. J. Casper, Y. Wan, and E. S. Ebbini, "Adaptive transthoracic refocusing of dual-mode ultrasound arrays," *IEEE Trans Biomed Eng,* vol. 57, pp. 93-102, Jan 2010.

[8] J. F. Aubry, M. Pernot, F. Marquet, M. Tanter, and M. Fink, "Transcostal high-intensity-focused ultrasound: ex vivo adaptive focusing feasibility study," *Phys Med Biol,* vol. 53, pp. 2937-51, Jun 7 2008.

[9] E. Cochard, C. Prada, J. F. Aubry, and M. Fink, "Ultrasonic focusing through the ribs using the DORT method," *Med Phys,* vol. 36, pp. 3495-503, Aug 2009.

[10] B. Quesson, M. Merle, M. O. Kohler, C. Mougenot, S. Roujol, B. D. de Senneville, and C. T. Moonen, "A method for MRI guidance of intercostal high intensity focused ultrasound ablation in the liver," *Med Phys,* vol. 37, pp. 2533-40, Jun 2010.

[11] H. L. Liu, C. L. Hsu, S. M. Huang, and Y. W. Hsi, "Focal beam distortion and treatment planning for transrib focused ultrasound thermal therapy: a feasibility study using a two-dimensional ultrasound phased array," *Med Phys,* vol. 37, pp. 848-60, Feb 2010.

[12] S. Bobkova, L. Gavrilov, V. Khokhlova, A. Shaw, and J. Hand, "Focusing of high-intensity ultrasound through the rib cage using a therapeutic random phased array," *Ultrasound Med Biol,* vol. 36, pp. 888-906, Jun 2010.

[13] A. D. Maxwell, W. Tzu-Yin, C. A. Cain, J. B. Fowlkes, X. Zhen, O. A. Sapozhnikov, and M. R. Bailey, "The role of compressional pressure in the formation of dense bubble clouds in histotripsy," *Ultrasonics Symposium (IUS), 2009 IEEE International*, pp. 81-84, 20-23 Sept. 2009 2009.

[14] Z. Xu, J. B. Fowlkes, E. D. Rothman, A. M. Levin, and C. A. Cain, "Controlled ultrasound tissue erosion: the role of dynamic interaction between insonation and microbubble activity," *J Acoust Soc Am,* vol. 117, pp. 424-35, Jan 2005.

[15] Z. Xu, J. B. Fowlkes, A. Ludomirsky, and C. A. Cain, "Investigation of intensity thresholds for ultrasound tissue erosion," *Ultrasound Med Biol,* vol. 31, pp. 1673-82, Dec 2005.

[16] J. E. Parsons, C. A. Cain, and J. B. Fowlkes, "Cost-effective assembly of a basic fiber-optic hydrophone for measurement of high-amplitude therapeutic ultrasound fields," *J Acoust Soc Am,* vol. 119, pp. 1432-40, Mar 2006.

[17] A. D. Maxwell, T. Y. Wang, L. Yuan, A. P. Duryea, Z. Xu, and C. A. Cain, "A tissue phantom for visualization and measurement of ultrasound-induced cavitation damage," *Ultrasound Med Biol,* vol. 36, pp. 2132-43, Dec 2010.

[18] T. Y. Wang, Z. Xu, T. Hall, J. Fowlkes, W. Roberts, and C. Cain, "Active focal zone sharpening for high-precision treatment using histotripsy," *IEEE Trans Ultrason Ferroelectr Freq Control,* vol. 58, pp. 305-15, Feb 2011.

[19] V. Khokhlova, S. Bobkova, and L. Gavrilov, "Focus splitting associated with propagation of focused ultrasound through the rib cage," *Acoustical Physics,* vol. 56, pp. 665-674, 2010.

[20] W. Hong, E. S. Ebbini, M. O'Donnell, and C. A. Cain, "Phase aberration correction and motion compensation for ultrasonic hyperthermia phased arrays: experimental results," *Ultrasonics, Ferroelectrics and Frequency Control, IEEE Transactions on,* vol. 41, pp. 34-43, 1994.

[21] J. B. Fowlkes and L. A. Crum, "Cavitation threshold measurements for microsecond length pulses of ultrasound," *J Acoust Soc Am,* vol. 83, pp. 2190-201, Jun 1988.

[22] A. J. Coleman, T. Kodama, M. J. Choi, T. Adams, and J. E. Saunders, "The cavitation threshold of human tissue exposed to 0.2-MHz pulsed ultrasound: preliminary measurements based on a study of clinical lithotripsy," *Ultrasound Med Biol,* vol. 21, pp. 405-17, 1995.

[23] C. K. Holland and R. E. Apfel, "Thresholds for transient cavitation produced by pulsed ultrasound in a controlled nuclei environment," *J Acoust Soc Am,* vol. 88, pp. 2059-69, Nov 1990.

[24] A. D. Maxwell, T. Y. Wang, C. A. Cain, J. B. Fowlkes, O. A. Sapozhnikov, M. R. Bailey, and Z. Xu, "Cavitation clouds created by shock scattering from bubbles during histotripsy," *J Acoust Soc Am,* vol. 130, pp. 1888-98, Oct 2011.

Chapter 3

In Vivo Transcostal Histotripsy Therapy

This chapter explores the feasibility of using non-invasive histotripsy therapy for transcostal treatments *in vivo* without aberration correction. To assess the therapeutic impact of the ribcage during treatments, transcostal and transabdominal treatments are performed in porcine liver and lesions compared in terms of resulting ablation morphology. Thermal effects induced on overlying tissues are also investigated and discussed in the context of comparable HIFU thermal dosages.

3.1 Introduction

The *in vitro* study presented in Chapter 2 suggested that the pressure threshold mechanism governing the initiation of cavitation bubble clouds allowed histotripsy therapy to have a high degree of immunity against acoustic aberration phenomena such as grating lobes. Precise histotripsy lesions could be created through rib obstructions without using aberration correction mechanisms by controlling the input pressure of the transducer in such a way that only the main focal beam exceeded the initiation threshold while maintaining grating lobes below the threshold. This suggests that histotripsy therapy may hold significant therapeutic advantages in comparison to conventional thermal ablation mechanisms, in terms of reduced susceptibility to acoustic aberration effects, and the much lower likelihood of inducing thermal damage on overlying tissues, especially those near the rib bones.

The objective of the study presented herein was to further evaluate the capabilities of histotripsy therapy for non-invasive transcostal surgery *in vivo* without using aberration correction mechanisms. Transcostal porcine liver treatments were conducted through therapy windows with full ribcage coverage and compared to transabdominal treatments performed without rib obstruction. Temperature changes in the overlying tissues were monitored for the entire duration of each treatment to assess potential thermal effects of the therapy, especially in regions near the rib bones. Resulting lesions were evaluated for uniformity of ablation and overall dimensions, while overlying tissues were inspected for any potential signs of collateral damage caused by either mechanical or thermal effects.

3.2 Methods

3.2.1 Animal Preparation

A total of 9 pigs weighing 40-50 kg were used in the preliminary experiments. Each pig was initially sedated with intramuscular injections of tiletamine hydrochloride and zolazepam hydrochloride (Telazol®, Fort Dodge Animal Health, Fort Dodge, IA), and xylazine hydrochloride (AnaSed®, Lloyd Laboratories, Shenandoah, IA). This was followed by catheterization of the auricular ear vein and endotracheal intubation, which allowed full body anesthesia to be induced by inhalation of isoflurane gas (1.5-2.0%). The animal was then placed to the surgical table and positioned with its back lying against the table; the skin of the pig was shaved and treated with a depilatory cream. Ultrasound coupling was achieved through an external water bowl positioned on the chest of the animal. The bowl contains an open cutout to allow the propagation of ultrasound and was lined with adhesive surgical drape (Ioban, 3M Company, St. Paul, MN) to provide a water-tight seal against the skin of the pig and prevent fluid leakage (Figure 3.1). Vital signs were collected throughout the experiment using a veterinary monitoring device. Physiological saline (0.9% sodium hydrochloride) at a rate of 10 ml/kg/h was administered for the duration of the treatment through the auricular catheter. All procedures were approved by the Committee on Use and Care of Animals at the University of Michigan.

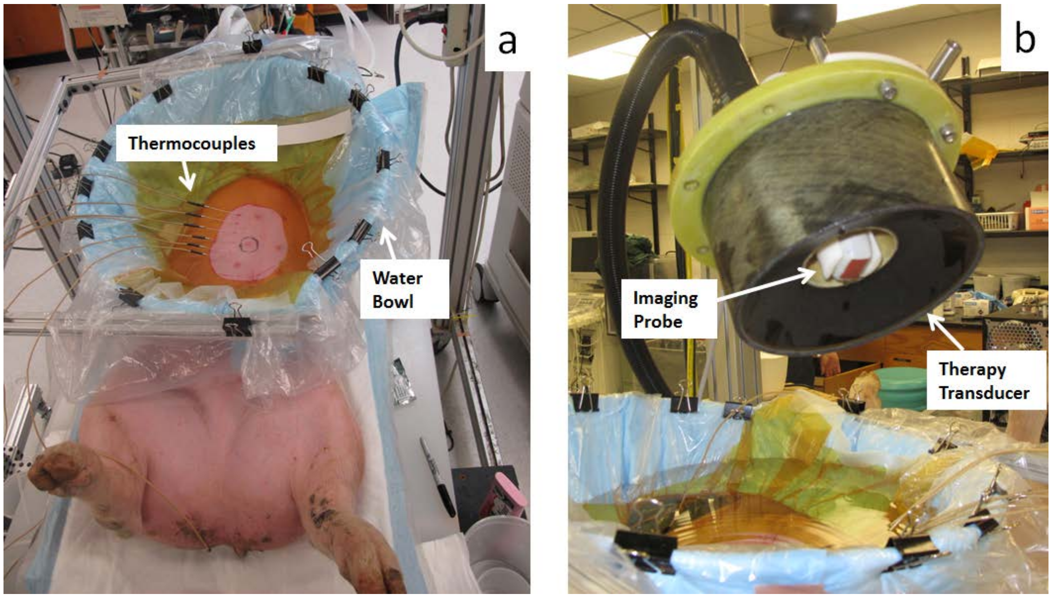

Figure 3.1. (a) Treatment setup with ultrasonic coupling bowl positioned on the chest of the pig. Hypodermic thermocouples were inserted on the ribs to monitor temperature changes during the treatment. (b) Therapy unit with ultrasound imager probe coaxially mounted with a 750 kHz focused transducer.

3.2.2 Experimental Apparatus

A focused, 750 kHz transducer with an aperture size of 15 cm and a geometric focal length of 12 cm (Imasonic SAS, Voray sur l'Ognon, France) was used in all experiments. The transducer aperture contains a concentric hole of 5.9 cm in diameter, specifically designed to accommodate ultrasound imaging probes. The treatment progress was monitored in real time by a 3-8 MHz probe (S8, SONOS 7500, Philips Healthcare, Andover, MA), which was coaxially positioned with the therapy transducer (Figure 3.1). The transducer and imaging probe were attached to a swivel joint mounted to a motorized 3-axis positioning system (Parker-Hannifin, Cleveland, OH) which was used to mechanically steer the focus of the transducer. Ultrasound coupling was accomplished through degassed water at room temperature (23-25 ºC) which was brought in direct contact with the skin of the pigs.

Before each experiment, the therapeutic focus of the transducer was found by creating a bubble cloud in degassed water and identifying the location of the hyperechoic region in the imaging field of the ultrasonic probe with a visual marker. To monitor the degree of heating in the overlying tissues during treatment, 4 to 5 hypodermic needle thermocouples (type T, Physitemp Instruments Inc., Clifton, NJ) were inserted superficially on the skin to cover the aperture of the treatment window. In treatments through windows that were fully covered by the ribcage, the thermocouples were inserted as close as possible to the rib bones to accurately measure the effect of additional energy absorption by bone tissue. Additional temperature measurements were collected by placing thermocouples outside the sonication windows to serve as references. All procedures described herein were reviewed and approved by the University Committee on Use and Care of Animals at the University of Michigan.

3.2.3 Histotripsy Treatment and Evaluation

Preliminary acoustic imaging was performed in each experiment in order to find a suitable acoustic window for treatment. Once this procedure was completed, the estimated treatment focus of the transducer was found by generating a bubble cloud in water, and identifying its position in the field of view of the ultrasound imaging probe. Treatment was administered using sonication pulses of 5 cycles applied at a repetition rate (PRF) of 200 Hz. Estimated *in situ* rarefactional pressures in the range of 17-19 MPa were achieved by gradually increasing the acoustic power level of the transducer until a hyperechoic cavitation cloud was observed at the focus of the treatment.

In all experiments, ablation volumes were created by mechanically steering the therapy focus in a treatment grid of 125 points covering a 5 x 5 x 5 mm cubic region. Each treatment point was separated by 1 mm and treated for approximately 20 s (4000 therapy pulses), with the total treatment time spanning approximately 42 minutes. While this treatment dosage is significantly beyond the requirements for histotripsy liver ablation [1, 2], longer treatment times were specifically used in this study to better evaluate the temperature increase behavior during sonication, and facilitate the assessment of any potential signs of collateral damage from the treatment.

The pigs were euthanized within an hour after treatment, at which point the treated livers and overlying tissue were harvested for gross inspection and further examination under MR imaging. *Ex vivo* samples were embedded in a 1% agarose gel mold and imaged by a 7T small animal scanner (7.0 Tesla, 310 mm bore, Varian, Inc., Walnut Creek, CA). After the imaging procedure, the samples were fixed in 10% buffered formaldehyde solution for histological analysis.

3.3 Results

3.3.1 Ultrasound Imaging

Each animal received a single liver treatment with the exception of one pig which underwent two treatments. Bright, hyperechoic cavitation bubble clouds were successfully generated at the focus of the treatment in all experiments by slowly increasing the acoustic power amplitude of the transducer until a bubble cloud was observed at the focus. As a larger volume of the bulk tissue was ablated, dark, hypoechoic regions were observed to form near the focal region, corresponding to the extent of the tissue that was fractionated by histotripsy therapy. Figure 3.2 shows representative B-mode images of the bubble cloud during treatment through the ribs.

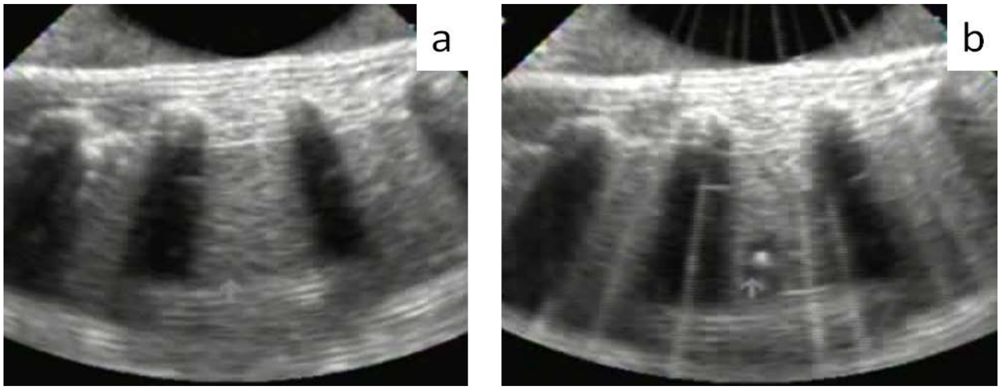

Figure 3.2. B-mode ultrasound image of liver before treatment (a). Dark shadows are visible under the rib bones due to the reflection and attenuation of the ultrasound signal. Ultrasound image captured during histotripsy therapy showing the hyperechoic cavitation bubble cloud (near the arrow) generated in porcine liver and the surrounding, hypoechoic ablated region (b).

3.3.2 Lesion Analysis

A total of 8 liver lesions were created in 7 out of 9 pigs, with 4 lesions generated through transcostal acoustic windows with full rib coverage and 4 lesions generated through transabdominal windows with no overlying bone obstruction. All transcostal lesions and 2 of the transabdominal lesions were generated within the bulk tissue of the liver, whereas the other 2 transabdominal lesions were generated between the lobes of the liver. Transabdominal lesions could not be reproduced as consistently as transcostal lesions in part due to the limited treatment access to the liver presented by acoustic windows with no ribcage obstruction.

In 2 of the 9 pigs used in this experiment series, lesions could not be identified in the harvested liver even though bubble clouds were visible at the focus under B-mode ultrasound. In these two cases, it is possible that the spleen may have been treated due to its echoic similarity to liver tissue. These two cases involved treatments through transabdominal windows.

Figure 3.3 shows MR images and the gross morphological aspect of lesions generated in liver through transcostal and transabdominal treatment windows. Under MR imaging, the ablated regions appeared as homogeneous hyperintense (bright) areas embedded within the liver tissue background. Hypointense (dark) contours surrounded the perimeter of the lesions, consisting primarily of deoxygenated red blood cells. Confined lesion volumes generated in bulk liver tissue through both treatment windows showed comparable lesion dimensions and fractionation patterns. Based on *ex vivo* MRI scans obtained of treated samples, the mean and standard deviation of lesion dimensions measured at their longest and widest points were approximately 20.7 x 13.4 mm ± (4.6 x 2.5 mm) for transcostal lesions and 18.6 x 14.7 mm ± (3.6 x 3.8 mm) for transabdominal lesions. Samples of overlying tissues within the sonication treatment windows were also imaged, with no identifiable evidence of thermal or mechanical damage to the ribs or soft tissue.

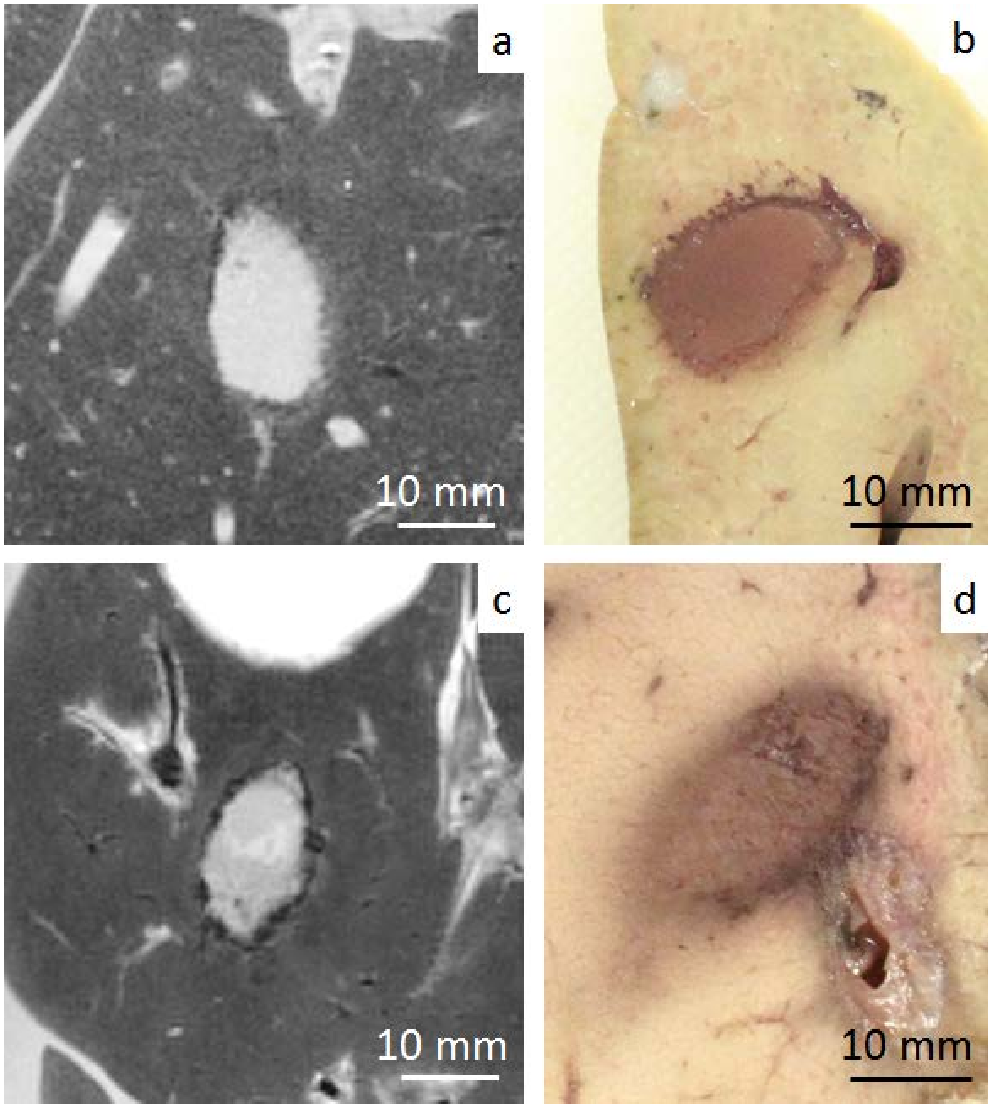

Figure 3.3. MR images and gross morphology pictures showing comparable liver lesions generated through transcostal (a and b), and transabdominal (c and d) treatment windows. Lesions were identifiable under MRI by their bright signature from the presence of homogenized tissue surrounded by a darker contour consisting of deoxygenated red blood cells.

Histological samples showed that lesion volumes generated through both treatment windows displayed an ablated region of homogenized tissue largely consisting of acellular debris (Figure 3.4). The lesions displayed areas with sharp boundaries between homogenized and intact tissue, and also regions where the ablation margins appeared to be less defined, with a more significant presence of hemorrhagic elements. This was observed in both transcostal and transabdominal lesions, and it is likely that the breathing motion of the pigs during the treatments may have contributed in creating this “blurring” effect on the lesion margins across the direction of the movement.

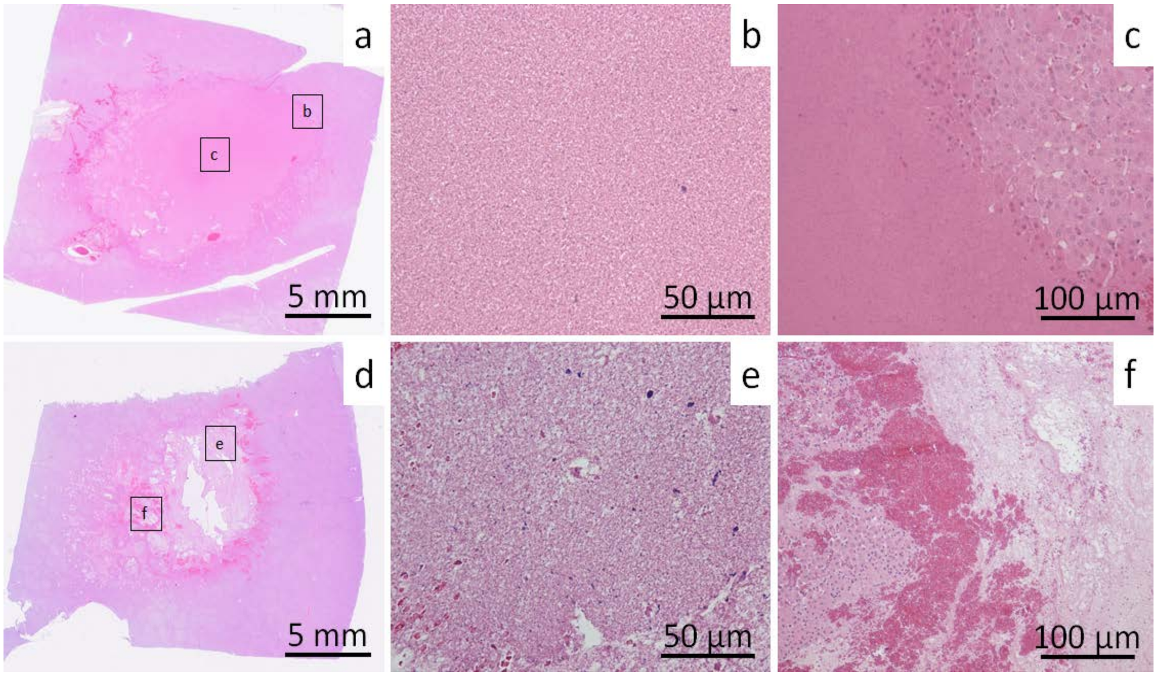

Figure 3.4. Representative histological samples of a transcostal (a-c), and a transabdominal (d-f) liver lesion. In both cases, the lesion center was characterized by the presence fractionated tissue consisting of mostly acellular debris (b and e). Lesion contours generally displayed sharp ablation margins (c), while boundaries with more irregular ablation presented a greater degree of hemorrhage (f).

3.3.3 Temperature Measurements

Temperature measurements of the overlying tissues during treatment were conducted with several hypodermic thermocouples placed across the acoustic window on the skin of the pigs. In transcostal treatments, the mean temperature was observed to increase rapidly within the first 15 minutes of treatment, reaching a saturation level of about 90% of its final value after 25 minutes of treatment. The final mean temperature measured on the ribs after 42 minutes of treatment was approximately 31.4 ºC, an increase of 4.1 ºC with respect to the pre-treatment baseline temperatures (27.3 ºC). The maximum temperature measured during each treatment appeared to follow an inverse trend with approximate distance of the ribcage from the treatment focus (Table 3.1). The maximum temperature increase measured in all experiments reached approximately 8.3 ºC when the ribcage interface was located at 3.5 cm above the treatment focus.

Table 3.1. Approximate distance from the treatment focus to the ribcage in transcostal treatments and maximum temperature increase measured on the ribs.

Treatment Number	*Ribcage distance to focus (cm)*	*Maximum Temperature Increase (ºC)*
1	6	5.4
2	5.5	4.7
3	4.2	6.6
4	3.5	8.3

As expected, the mean temperature rise measured during transabdominal treatments was significantly lower in comparison to that observed in transcostal treatments with full ribcage coverage. The overall mean temperature increase rose to a maximum of 32.7 ºC from a mean baseline temperature of 31.1 ºC, for a total increase of 1.6 ºC during histotripsy treatment. Reference (control) measurements from thermocouples placed outside the sonication window displayed a similar increase pattern from an initial state of 29 ºC to 30.1 ºC (1.1 ºC relative increase), likely due to the warming of the water bath used for acoustic coupling by the animal’s body heat.

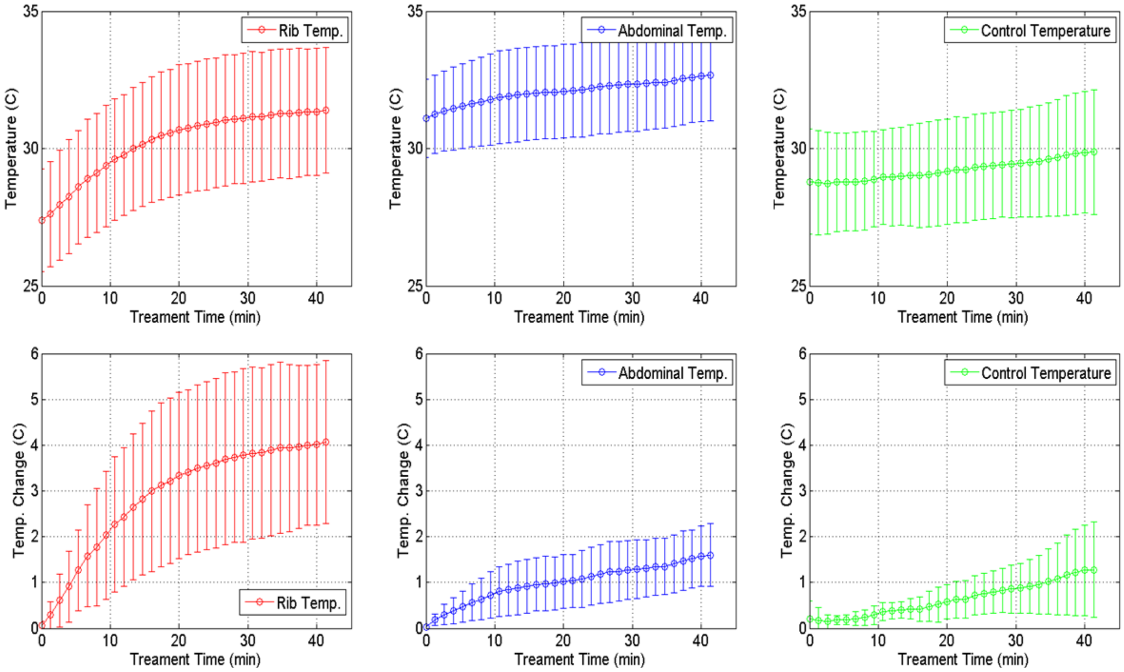

Figure 3.5. Mean and standard deviation plots of thermocouple temperature measurements obtained during transcostal (n = 15) and transabdominal (n = 20) histotripsy treatments. Actual temperature readings are shown in the top row of figures, while baseline temperature increases are displayed in the bottom row. Control temperatures measured outside the treatment window (n = 5) are shown for reference purposes. Error bars correspond to ± 1 standard deviation.

3.4 Discussion

This study explored the feasibility of using non-invasive histotripsy therapy for transcostal tissue ablation *in vivo* without using aberration correction mechanisms. Fully ablated lesions of comparable size could be generated through transcostal and transabdominal treatment windows with full, and no ribcage coverage, with no noticeable signs of damage to the ribs or the overlying soft tissue in either MR imaging or through morphological inspection of samples harvested after the treatment. With the treatment parameters used in this study, (5 cycle pulses at a repetition rate of 200 Hz), the effective sonication duty cycle applied to initiate a bubble cloud was less than 0.14% in all treatments, which is significantly lower than conventional thermal HIFU therapy standards. In all the experiments, the highest temperature measured on the ribs during treatment was still lower than the body temperature of the pigs (~ 36 ºC).

The sonication pressure levels reported herein (17-19 MPa) are estimations based on the expected degree of attenuation and depth of the targets treated in the experiments applied to acoustic calibration data obtained in water. It should be noted that this approach is only able to provide a limited estimation, which is restricted to the linear frequency component (750 kHz) associated with the peak rarefactional pressure of the waveform and does not account for the non-linear behavior of large amplitude compressional shock waves. However, whereas acoustic pressure levels cannot be easily measured *in vivo*, treatment at or near the cavitation bubble cloud threshold of the medium is still feasible thanks to the real-time imaging feedback available for histotripsy therapy. This can be achieved by gradually increasing the acoustic power input until a cavitation bubble cloud is observed to at the focus of the treatment. This near-threshold treatment approach has been shown to be effective in preventing secondary lobes from causing additional collateral damage as discussed in Chapter 2.

As previously mentioned, the higher sonication dosage used in this study (4000 pulses per treatment point) is significantly beyond the requirements for liver fractionation using histotripsy therapy. Longer treatment times were deliberately chosen for this investigation primarily to allow the evaluation of the temperature increase behavior over a wider time window. It is interesting to note, however, that under MRI, the lesion volumes generated in the present study displayed much more uniform hyper-intense ablated areas in comparison to the lesions generated in a previous *in vivo* investigation using a lower sonication dosage (2000 pulses per treatment point) [2]. While this lower dosage was shown to be sufficient to fully homogenize liver tissue under histological evaluation, the acute aspect of these lesions under MRI regularly displayed large hypo-intense areas within the ablated regions, which were characterized by the presence of hemorrhage in the form of deoxygenated red blood cells.

One explanation for the increased uniformity of the ablation volumes observed in MRI would be that the higher treatment dosage used in this study for a relatively small volume may have accelerated the hemolysis process of red blood cells extravasated during the initial fractionation process. Cavitation bubbles are effective in lysing red blood cells [3] and have also been shown to serve as catalysts for platelet aggregation [4], which may have stemmed the flow of additional red blood cells into the already fractionated area.

In both transcostal and transabdominal treatment cases, the overall dimensions of the ablation volumes created by using this higher sonication dosage also appeared to be larger than the 5 mm cubic grid in which the therapy focus was steered. A larger lesion volume was an expected outcome due to the finite size of the transducer's focal region (approximately 3 x 12 mm). Another possible contributing factor was that the bubble cloud echo signature was observed to have tendency to expand in size as the therapy progressed and more of the tissue was fractionated, likely due to the different mechanical characteristics of homogenized tissue. It is possible that the presence of this larger bubble cloud, aided by the high number of sonication pulses applied for each treatment spot may have further extended the ablation boundaries of the lesions. While in this study a fixed sonication power (sufficient to initiate cavitation in bulk tissue in its unfractionated state) was used throughout the entirety of the treatments for consistency purposes, the bubble cloud expansion effects due to tissue homogenization could be mitigated by simply decreasing the power input to the transducer as the treatment progresses.

The maximum temperatures measured on the surface of the ribs in all transcostal treatments were below the body temperature of the animals (~ 36 ºC) using room temperature water (23-25 ºC) in direct contact to the skin of the pigs for acoustic coupling purposes. Mean pre-treatment baseline temperatures were different for transcostal and transabdominal cases (27.3 vs. 31.1 ºC), possibly due to the higher vascular activity near the tissues surrounding the abdominal cavity in comparison to the skin overlying the ribcage. The absolute maximum temperature increase in all experiments measured from a baseline state was approximately 8.3 ºC (Figure 3.6). This particular reading was obtained in an experiment where the ribs were found closer to the focus of the treatment (3.5 cm). This phenomenon is intuitively predictable since the acoustic focusing pattern of the transducer would naturally increase the sonication intensity at locations closer to the focus.

Assuming a simple “worst-case” scenario in which temperature increase and saturation patterns are similar, from a normal baseline temperature of 37 ºC (human body temperature), such an increase would bring the overall saturation point to 45.3 ºC. An equivalent t_{43} thermal dose could then be calculated using the standard formula proposed by Sapareto and Dewey [5]:

$$t_{43} = \int_{t_{initial}}^{t_{final}} R^{43-T(t)}\, dt \qquad 3.1$$

Where $$R = \begin{cases} 0.5 \quad if \quad T(t) > 43\,°C \\ \qquad or \\ 0.25 \quad if \quad T(t) < 43\,°C \end{cases} \qquad 3.2$$

Integrating for the temperature curve shown in Figure 3.6 with a supposed baseline starting point of 37 ºC yields a t_{43} equivalent of approximately 95 minutes, which is still significantly less than the dosages typically applied to achieve thermal tissue ablation [6-8].

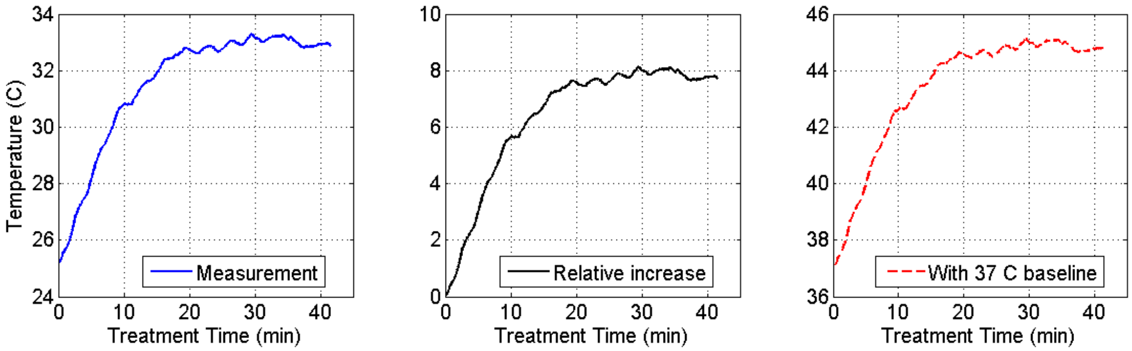

Figure 3.6. Maximum rib temperature recorded in all treatments (left) showing a relative increase of 8.3 ºC from the pre-treatment baseline temperature (center). Estimated maximum temperature increase if a baseline temperature of 37 ºC is applied (right).

It should be stated that this estimation is limited, at best, for the specific treatment parameters used in this study, and that temperatures increase patterns may significantly change if the treatment focus is brought even closer to the plane of the ribs. In addition to the narrowing of the focusing cone, another effect that becomes relevant in this case is the increase in the non-linearity of the acoustic pulses, especially near to the focus of the transducer, which could significantly alter the ultrasound absorption characteristics of the tissue [9]. Future studies will attempt to include a model of the heat uptake behavior of overlying tissues during histotripsy treatment using thermal absorption simulations.

As discussed in previous chapters, the initiation of cavitation bubble clouds in histotripsy therapy is not primarily associated with the duty cycle (or average intensity) of the sonication pulses, but rather, with the peak instantaneous rarefactional pressures available at the focus. While in this study pulse lengths of 5 cycles at a PRF of 200 Hz were used to facilitate bubble cloud initiation through the highly attenuative ribcage, more powerful transducers capable of generating higher focal peak rarefactional pressures could allow the sonication duty cycle of the therapy to be decreased, further reducing thermal effects.

The preliminary results from this study suggest that histotripsy ablation is relatively unaffected by rib obstruction in transcostal treatment windows, as long as sufficient pressure is available at the focus of the treatment. The low duty-cycle operation also minimizes the likelihood of inducing thermally damaging effects on the ribs without the need of rib-sparing aberration correction algorithms. This therapeutic versatility could be a useful feature for a variety of non-invasive transcostal surgical applications such as treatments for hepatic and pancreatic cancer, and for cardiac ablation procedures.

3.5 References

[1] T. Y. Wang, Z. Xu, T. L. Hall, J. B. Fowlkes, and C. A. Cain, "An efficient treatment strategy for histotripsy by removing cavitation memory," *Ultrasound Med Biol,* vol. 38, pp. 753-66, May 2012.

[2] E. Vlaisavljevich, Y. Kim, S. Allen, G. Owens, S. Pelletier, C. Cain, K. Ives, and Z. Xu, "Image-guided non-invasive ultrasound liver ablation using histotripsy: feasibility study in an in vivo porcine model," *Ultrasound Med Biol - Accepted,* 2013.

[3] A. D. Maxwell, T. Y. Wang, L. Yuan, A. P. Duryea, Z. Xu, and C. A. Cain, "A tissue phantom for visualization and measurement of ultrasound-induced cavitation damage," *Ultrasound Med Biol,* vol. 36, pp. 2132-43, Dec 2010.

[4] S. L. Poliachik, W. L. Chandler, R. J. Ollos, M. R. Bailey, and L. A. Crum, "The relation between cavitation and platelet aggregation during exposure to high-intensity focused ultrasound," *Ultrasound Med Biol,* vol. 30, pp. 261-269, 2004.

[5] S. A. Sapareto and W. C. Dewey, "Thermal dose determination in cancer therapy," *Int. J. Radiation Oncology Biol. Phys.,* vol. 10, pp. 787-800, 1984.

[6] S. Dasgupta, J. Wansapura, P. Hariharan, R. Pratt, D. Witte, M. R. Myers, and R. K. Banerjee, "HIFU lesion volume as a function of sonication time, as determined by MRI, histology, and computations," *J Biomech Eng,* vol. 132, p. 081005, Aug 2010.

[7] Y. F. Zhou, "High intensity focused ultrasound in clinical tumor ablation," *World J Clin Oncol,* vol. 2, pp. 8-27, Jan 10 2011.

[8] G. ter Haar, "Acoustic surgery," *Physics Today*, vol. 54, pp. 29-34, 2001.

[9] M. S. Canney, M. R. Bailey, L. A. Crum, V. A. Khokhlova, and O. A. Sapozhnikov, "Acoustic characterization of high intensity focused ultrasound fields: a combined measurement and modeling approach," *J Acoust Soc Am*, vol. 124, pp. 2406-20, Oct 2008.

Chapter 4

In Vivo Transabdominal Fetal Histotripsy Therapy

This chapter presents the first of two studies exploring the feasibility and potential of using non-invasive transabdominal histotripsy for fetal therapy applications *in utero*. In the initial study discussed herein, the feasibility of conducting fetal histotripsy therapy is evaluated in an ovine model without using aberration correction mechanisms. Non-invasive cardiac, hepatic and renal histotripsy treatments are performed to evaluate the level of precision and effectiveness of tissue fractionation induced by transabdominal fetal histotripsy therapy through complex, heterogeneous acoustic windows.

4.1 Introduction

Congenital abnormalities are the leading cause of infant mortality in the U.S., accounting for more than 20% of all infant deaths [1]. Many of these anomalies require invasive surgery after birth; however, some conditions are amenable to fetal intervention procedures, which may be able to prevent disease progression or worsening of the fetal condition [2, 3]. Presently available fetal treatments for congenital abnormalities include percutaneous balloon atrial septoplasty in hypoplastic left heart syndrome with restrictive atrial septum[4], fetoscopic obliteration of blood vessels in twin-twin transfusion syndrome [5], and open surgical debulking for rapidly growing fetal masses [6].

Current prenatal care technology is capable of detecting and diagnosing congenital diseases as early as the second trimester of gestation [7]. However, *in utero* fetal intervention remains a challenging task, requiring experienced operators, with risk often commensurate with the degree of invasiveness of the procedure. Preterm labor, infection and premature rupture of membranes remain as risk factors with even minimally invasive procedures. Physical and practical limitations such as fetal size and adequacy of available equipment exist for current approaches; this limits the timing of interventions and likely affects their success. Non-invasive interventional techniques, such as therapeutic ultrasound, could significantly reduce risks for both mother and fetus while possibly allowing earlier intervention options to yield improved outcomes.

Fetal interventions in animal models have been previously reported using high intensity focused ultrasound (HIFU) as a thermal ablation method [8, 9], but the overall number of studies published on non-invasive fetal therapy is scarce. Histotripsy is a form of focused ultrasound therapy based on a different mechanism in which high intensity ultrasound pulses are applied to create controlled cavitation bubble clouds at the treatment focus. Previous experiments have successfully used histotripsy to fractionate and remove tissue in heart [10, 11], kidney [12] and prostate [13] *in vivo*. The purpose of this study was to demonstrate the feasibility of applying histotripsy to non-invasively create localized lesions in fetal organs in a fetal sheep model.

4.2 Methods

4.2.1 Animal Preparation

Experiments involved 11 gravid ewes, median gestation 115 days, range 102-129 days (full ovine gestation: 150 days) consisting of 15 fetuses. Each ewe was first sedated with an intramuscular injection of diazepam (0.5-1 ml/kg) and intravenous propofol (4-6 ml/kg), followed by endotracheal intubation and inhalation of 1-3% isoflurane gas. Vital signs were monitored throughout the experiment. All procedures were reviewed and approved by the University Committee on Use and Care of Animals at the University of Michigan.

Once the ewe was anesthetized and secured on the table, the abdomen was shaved and a depilatory cream was applied to remove any remaining wool and improve ultrasound coupling. Preliminary ultrasound imaging was performed with a clinical ultrasound imaging system (Sonos 7500, Philips Electronics, Andover, MA) with a 5 MHz curvilinear imaging probe (Model c3540, Philips Electronics, Andover, MA) to determine the number and lie of the fetuses. The ewe was then positioned on her side or back to optimize acoustic windows for fetal targeting.

4.2.2 Experimental Setup

A 1 MHz focused ultrasonic transducer (Imasonic, Besançon, France) with an aperture of 100 mm and focal length of 90 mm was used as the therapeutic unit. To monitor the treatment, a 3 MHz phased array ultrasonic imaging probe was coaxially aligned through a center hole in the therapy transducer specifically designed to accommodate the probe. The focal location of the transducer with respect to the imaging probe's field of view was found prior to treatment by generating a cavitation cloud in degassed water and highlighting the region where hyperechoic activity was observed on the imaging screen. Following this procedure, a metal bowl with a center opening lined with clear plastic was coupled to the ewe's abdomen with acoustic transmission gel and filled with degassed water. The transducer unit was secured to a 3-axis motorized system (Parker Hannifin, Rohnert Park, CA) and positioned within the water bowl to place the transducer's focus on the targeted organ (Figure 4.1).

4.2.3 Histotripsy Treatment

The sheep were exposed to 1 MHz ultrasound pulses with measured free-field peak rarefactional pressures of 10-16 MPa. The ultrasound pulses were 5 μs in duration (5 cycles at 1 MHz) and separated by 1-5 ms (i.e., pulse repetition frequencies of 200 Hz to 1 kHz). The formation of a highly echogenic cavitation bubble cloud at the focus of the transducer during treatment allowed procedures to be monitored in real time, with the cavitating bubble cloud serving the dual purpose of a tissue fractionation agent and a reference point for treatment guidance. Two-dimensional and color Doppler ultrasound imaging were used to follow the treatment and determine its effectiveness. Fetal kidney, liver, lung and heart were targeted at depths ranging from 2-8 cm from the maternal abdominal wall. In fetal kidney, liver and lung, cubic tissue volumes (0.1-1 cm^3) were targeted by mechanically scanning the focus of the therapeutic transducer through a 3-D grid of points during ultrasound exposure, with each point treated for approximately 2 s and adjacent points separated by 0.5-1.5 mm. In fetal hearts, single focus lesions were created by targeting individual spots from 30-80 s.

Following the intervention, the ewes were euthanized with pentobarbital. The fetuses were harvested and visually inspected for any signs of collateral damage near the targeted fetal organs. Targeted organs were removed and evaluated by gross examination, with samples stained with hematoxylin and eosin (H&E) for histological analysis by a pathologist (J.E.W.).

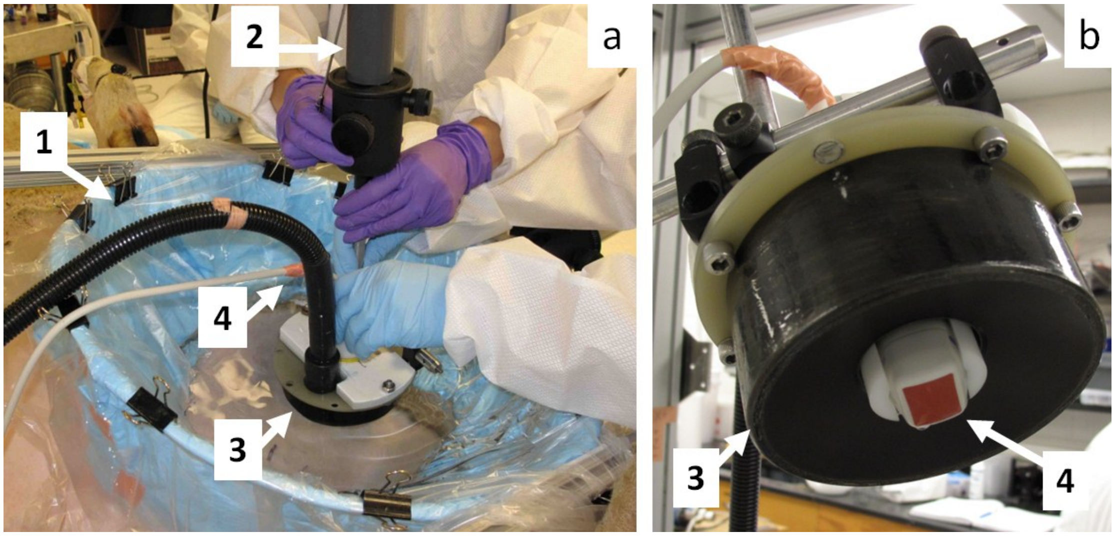

Figure 4.1 Experimental apparatus (a). Frontal view of the therapy unit (b). Legend: (1) Ultrasound coupling bowl with degassed water. (2) 3-axis positioning system. (3) 1 MHz therapeutic transducer. (4) Ultrasound imaging probe.

4.3 Results

A total of 19 out of 31 treatment attempts resulted in the successful generation of a cavitation cloud at the target, with lesions observed in 17 out of the 19 cases in which cavitation was generated (Table 4.1). Fetal kidney, liver and heart were primary targets, with fetal lungs treated in two occasions. Morphological and histological examination confirmed that lesions were generated at the sites where cavitation had been visualized on ultrasound imaging. No lesions were observed in targets where cavitation clouds were absent.

Table 4.1. Fetal histotripsy treatment results.

Targeted Organs	*Depth from maternal abdomen (median and range)*	*Treatments with cavitation monitored at the target*	*Pathologically confirmed lesions in organs with cavitation*
Kidney	3.6 (2.7-5.6) cm	5/5 (100%)	5/5 (100%)
Liver	6.4 (2.4-8.2) cm	5/9 (56%)	3/5 (60%)
Lung	6.4 (5.8-7.0) cm	2/2 (100%)	2/2 (100%)
Heart	7.2 (3.9-8.2) cm	7/15 (47%)	7/7 (100%)
Totals	6.5 (2.4-8.2) cm	19/31 (61%)	17/19 (89%)

4.3.1 Cases with Cavitating Bubble Cloud Generation

Cavitating bubble clouds were observed in 5/5 treatments in kidney, 5/9 in liver and 2/2 in lung, generating identifiable lesions in 5 kidneys, 3 livers and 2 lungs. In real time, the bubble clouds could be identified by their bright, flickering pattern, which was distinguishable from surrounding structures. The bubble clouds appeared as 3-4 mm wide hyperechoic zones at the geometric focus of the transducer by two-dimensional ultrasound imaging. In one occasion, the same liver was treated twice, with only one larger lesion found; the targeting locations of the two treatments were close enough that they likely formed a contiguous treated area which appeared as a single lesion. With the exception of one liver sample in which no clear signs of damage were encountered after treatment, lesions were present in all targets where cavitation bubble clouds were successfully generated.

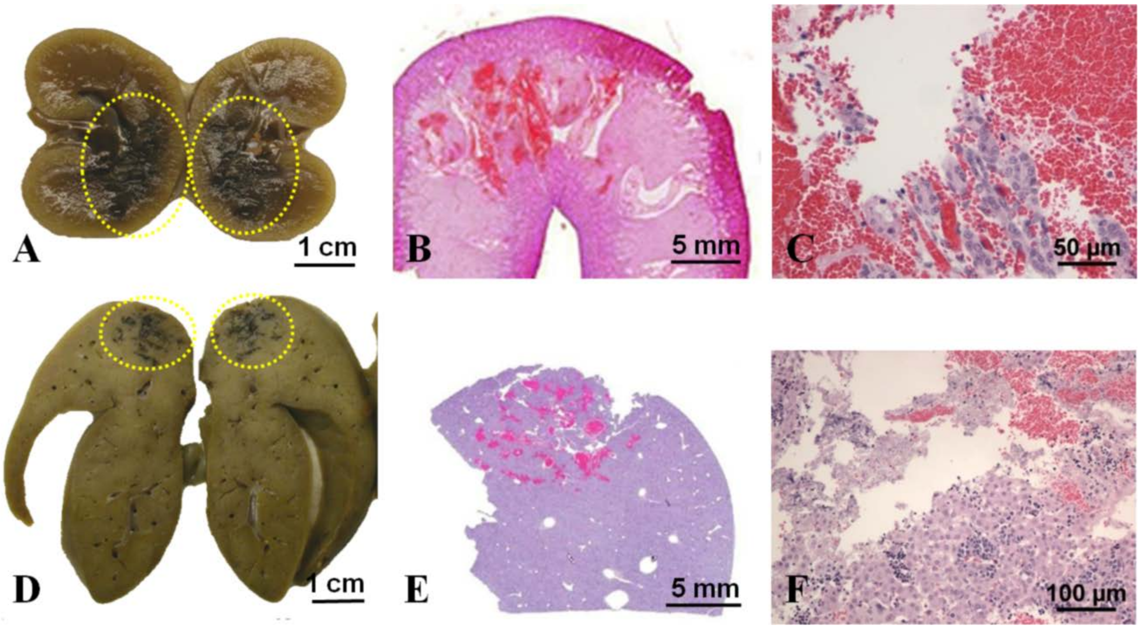

Figure 4.2 Representative pathology and histology pictures of a treated fetal kidney (A-C) and liver (D-F). The dark regions indicated by the ellipses correspond to lesion areas created by mechanically scanning the treatment focus (A and D). Histological examination revealed interspersed hemorrhagic spots in both kidney and liver (B and E). Damaged areas consisted of a variable combination of red blood cells, subcellular debris and intact tissue cells (C and F).

Morphological inspection of fixed samples showed darkened hemorrhagic regions corresponding to the locations where the cavitation bubble clouds had been observed, with affected areas comparable in size to the dimensions of regions scanned during treatment (Figure 4.2 A, D). Hemorrhage effects were noted to be more pronounced in the kidney than in other organs. Histological analysis revealed cellular destruction accompanied by hemorrhage within the treated area in the kidney and liver (Figure 4.2 B, C, E, F), with similar lesion patterns observed in the lung (not shown). The damaged regions were filled with red blood cells, acellular debris, and in certain cases, isolated islands of intact cells. The degree of cellular disruption in the lesions varied from case to case, ranging from total loss of all normal tissue architecture and structures to primarily hemorrhage with the majority of cellular structures physically intact.

In fetal heart treatments, cavitation bubble clouds were successfully generated at the focus in 7/15 cases. A total of 7 targeted single focus lesions were verified by pathology: 5 in the ventricular septum (VS) and 2 others in the ventricular wall. The ventricular free wall was specifically targeted in cases where the ventricular septum was deeper in the maternal abdomen than reachable by the focal zone of the therapy transducer.

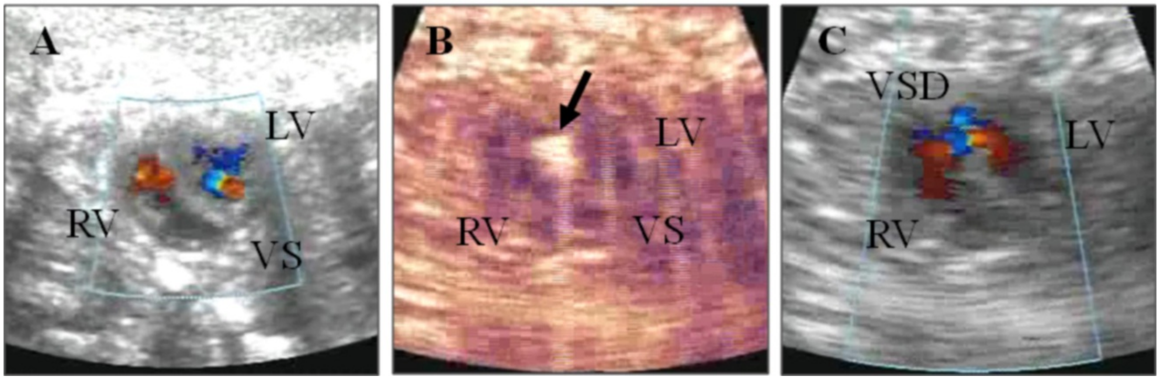

Figure 4.3 Pre-treatment color Doppler image of the fetal heart (A), showing an intact ventricular septum (VS). A cavitation bubble cloud is seen as a hyperechoic zone during histotripsy application as indicated by the arrow (B). Post-treatment color Doppler image of the fetal heart (C). The creation of a ventricular septal defect allows a flow channel between the left ventricle (LV) and the right ventricle (RV).

In one case, a lesion created in the VS perforated the septum and resulted in a ventricular septal defect (VSD), confirmed by two dimensional and color Doppler echocardiography (Figure 4.3). Transient fetal bradycardia was observed during several treatments, but resolved spontaneously with cessation of treatment. In 2 separate cases, the heart function ceased a few minutes after treatment. In both occasions, a cavitation cloud had been sustained for prolonged lengths of time (60 s or more) in the basal portion of the heart, possibly in the vicinity of the atrioventricular node.

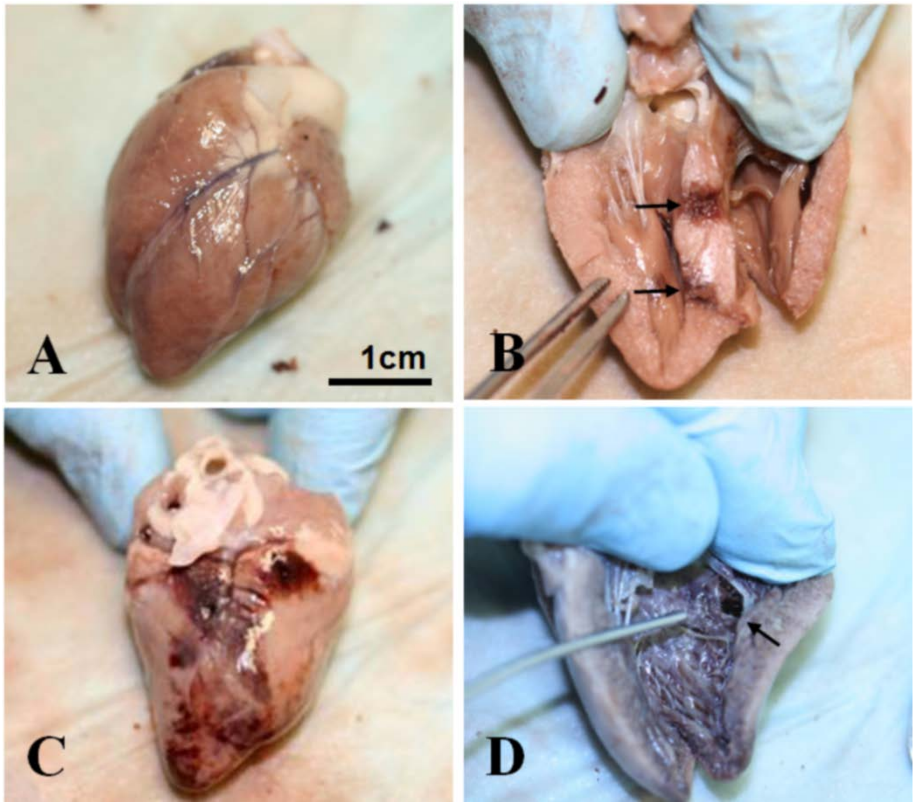

Figure 4.4 (A and B): A fetal heart in which the VS was targeted. External view with intact exterior (A). A longitudinal section of the heart revealed two lesions created in the ventricular septum after 30 and 60 s of exposure (indicated by the arrows), with approximately 2 mm and 3 mm in diameter respectively (B). The lesion edges were well defined within the ventricular septum, without noticeable damage outside this area. (C and D): Sample heart in which the ventricular wall was targeted. Substantial superficial hemorrhage was present on the heart wall (C). A lesion 3 mm in diameter (as indicated) was generated after 80 seconds of treatment (D).

Morphology revealed discolored myocardium at sites where cavitating bubble clouds had been present. Lesions created in the VS were approximately 2-3 mm in diameter, corresponding to the diameter of the cavitation cloud. A small amount of hemorrhage on the exterior of the ventricular wall was observed in 2/3 fetal hearts where the VS had been targeted. In one case (not the VSD case), however, precise lesions were created in the ventricular septum while the heart’s exterior remained intact with no damage visible outside the targeted region (Figure 4.4 A-B). In treatments where the ventricular wall was targeted, lesions were accompanied by the presence of substantial superficial hemorrhage on the pericardium (Figure 4.4 C-D).

Histological evaluation of the ventricular septal lesions showed complete fractionation of the septal tissue at the site of treatment with moderate amounts of free blood in the lesion (Figure 4.5 A-B). The myocardial structure was completely lost in the majority of cases, with lesions characterized by sharp margins. Most of the defect was lined by eosinophilic, contracted myocytes then flanked by normal myocardium. In a few areas, there was a thin rim of cellular debris between the blood and the myocardium. Lesions created on the ventricular free wall were generally characterized by significant hemorrhage and cellular ablation (Figure 4.5 C-D). In many areas, blood surrounded clusters of intact cardiomyocytes. Other areas had considerable cellular debris between the blood and the intact myocardium. Lesions that were less penetrating nevertheless consisted of hemorrhage and significant cellular destruction. Hemorrhage into the myocardial interstitium was occasionally present. The mildest lesions consisted of epicardial hemorrhage with small focal areas of cellular debris between the free blood and the myocardium.

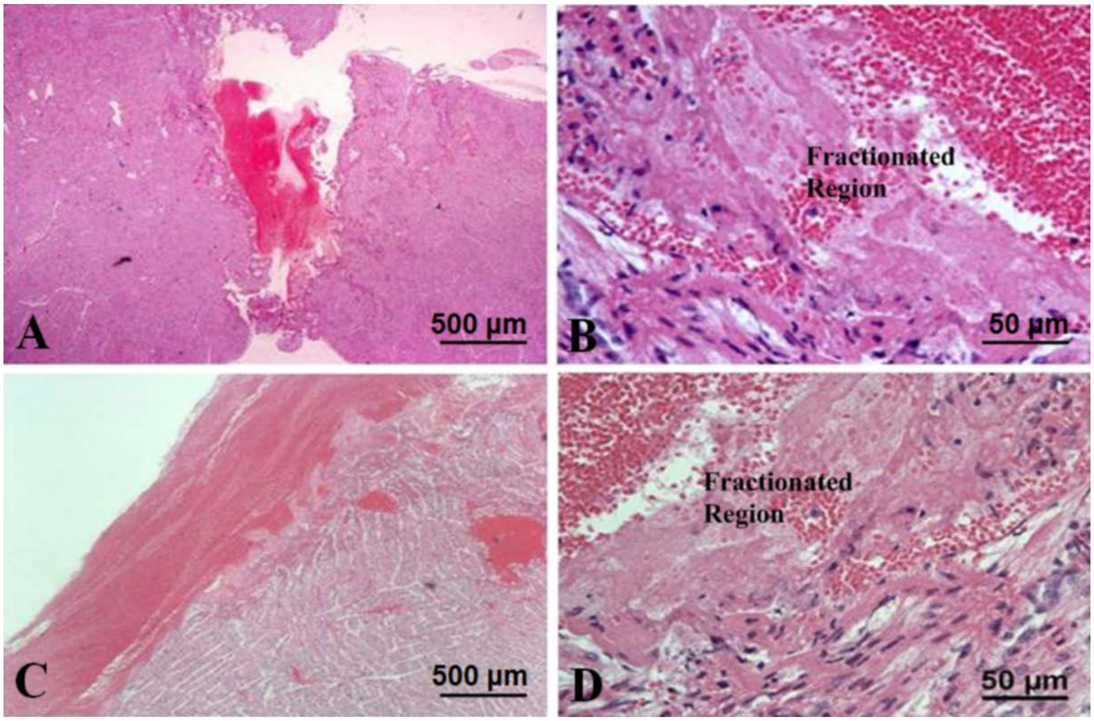

Figure 4.5 (A and B): H&E slides of a lesion created in the ventricular septum at 2x (A) and 20x (B) magnification. The darker area corresponds to residual blood from the ventricle that has coagulated inside the lesion cavity, which spanned almost the entire septum (A). Fractionated areas were characterized by distinct boundaries (B). (C and D): Lesions created on the heart wall were accompanied by epicardial hemorrhage with mild tissue destruction, here shown at 2x (C) and 20x (D) magnifications.

4.3.2 Cases without Cavitating Bubble Cloud Generation

Three factors were associated with the inability to generate a cavitating bubble cloud at the focus: depth of the target organ, acoustic obstruction by fetal limbs, and the presence of prefocal cavitation (Table 4.2). A cavitating cloud was generated in 100% (6/6) of fetal targets <4 cm from the maternal abdominal surface (Figure 4.6); in targets >4 cm from the maternal abdominal surface, the success rate for generation of a bubble cloud was only 52% (13/25, $p = 0.06$). A fetal extremity was in the path of the ultrasound beam in 67% (8/12) of cases with unsuccessful generation of a cavitating cloud, but only 21% (4/19) on cases with successful cavitation generation ($p = 0.03$). In 52% (16/31) of the treatment cases, varying amounts of prefocal cavitation were observed at the fetal skin and amniotic fluid interface, reducing or completely blocking ultrasound energy from reaching the target. This effect was observed in 75% (9/12) of cases in which a bubble cloud could not be generated at the focus and in 37% (7/19) of cases in which a cloud was successfully generated (p = 0.04). In general, short-lived prefocal cavitation did not create any visible damage to fetal tissues, but in a few lambs, longer and more intense occurrences caused partial discoloration on the fetal skin, possibly due to superficial hemorrhage.

Table 4.2. Bubble cloud initiation factors in fetal histotripsy therapy.

	Cavitation Generated	*No Cavitation Generated*	*p value**
Treatments (n = 31)	19	12	
Gestational Age (days) *Median (range)*	112 (102-129)	119 (108-129)	*0.76*
Target Depth (cm) *Median (range)*	6.0 (2.4-7.7)	7.4 (4.5-8.2)	*0.003*
Fetal Organ			*0.11*
Liver	5	4	
Kidney	5	0	
Heart	7	8	
Lung	2	0	
Fetal Orientation			*0.07*
Spine up	9	2	
Spine Down	3	4	
Right side up	1	4	
Left side up	6	2	
Obstructing Structure (*Umbilical cord, placenta and fetal limbs)*	7	10	*0.05*
Obstructing fetal limbs	4	8	*0.03*
Prefocal Cavitation	7	9	*0.04*

* P values: Mann-Whitney U for categorical variables or Fisher Exact Test for continuous variables

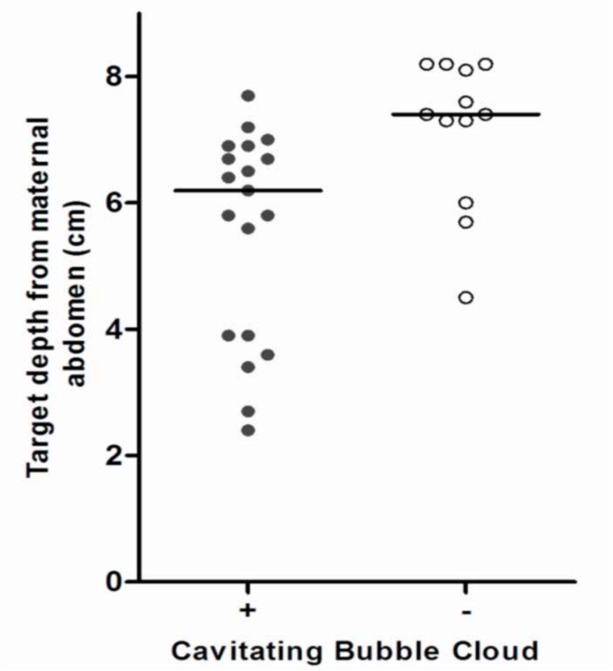

Figure 4.6 Incidence of focal cavitation vs. target depth. Solid dots represent successful attempts while open dots correspond to unsuccessful trials. The black horizontal lines indicate the median depth of each distribution.

4.4 Discussion

In this study, extracorporeal histotripsy was used to successfully generate lesions in fetal targets. Treatment was guided by a temporally changing, hyperechoic cavitation bubble cloud monitored by ultrasound imaging. The formation of a stable cavitation bubble cloud was a necessary requirement for lesion generation, with lesions being exclusively created in locations where cavitation activity was observed.

Histotripsy was successful in creating lesions in 17 out of 31 treatment attempts. In kidney, liver and lung, the size of the affected regions was comparable to the dimensions of the treatment scan; however, there was increased flanking hemorrhage in the kidney, perhaps due to its high vascularity. Ongoing studies show that hemorrhage and flanking injury induced by histotripsy fully recover within one month in neonatal porcine hearts [14]. The degree of cellular disruption in the lesions varied from total loss of all normal tissue architecture to primarily hemorrhage. This variability could be attributed to different levels of acoustic aberration and attenuation from fetal bone and tissue in each experiment. In heart treatments, 2-3 mm lesions separated by less than 1 cm were generated within the fetal ventricular septum. Considering that the ultrasound beam had to traverse up to 8 cm of complex overlying tissue, this targeting accuracy surpassed initial expectations, but still needs further refinement in order to improve consistency.

Treatment accuracy is essentially determined by the cavitation bubble cloud size at the target. Since the bubble cloud depends on acoustic parameters and therapy transducer characteristics, parameter optimization and transducer design modifications could increase the accuracy of the treatment. Improving echocardiographic imaging guidance quality would also be beneficial. In this study, a phased array imaging probe was used during treatment, as space constraints precluded use of a higher resolution curvilinear imaging probe in conjunction with the therapeutic transducer, thus limiting viewing quality. A new therapy transducer compatible with the curvilinear probe is currently under development.

Unsuccessful experiments were more likely to present overlying limbs or increased depth to target. These are somewhat predictable associations, as bone obstruction and multiple layers of inhomogeneous media will invariably subject the ultrasound beam to high degrees of attenuation and aberration before it reaches the focus. Attenuation makes it difficult to achieve sufficiently high focal pressures to initiate cavitation while acoustic aberration effects may change the focal pressure profile and increase the pressure levels of secondary lobes.

To reduce the effect of attenuation and aberration, choosing an appropriate acoustic window with minimal bone and tissue in the pathway is needed prior to treatment. In order to determine the best available window, a thorough 3D pre-treatment ultrasound scan of the fetus would be helpful. Aberration correction mechanisms may be applied to refocus the transducer to an extent by using phased array therapy transducers, but implementation for *in vivo* applications involves significant technical obstacles that were beyond the scope of this study. It is worth pointing out, however, that the relative immunity of histotripsy therapy against aberration effects as shown in Chapter 2 would be a beneficial feature in cases where the focal profile cannot be fully restored to optimal conditions, as long as sufficient acoustic pressure can be coupled to the focus.

Another possibility to reduce attenuation effects would be to treat at an earlier gestation stage, when fetal bones are less calcified. The aberration and attenuation from overlying fetal bone and tissue would be lower, although higher treatment accuracy would be required due to the smaller overall size of the fetus and targets. An additional challenge is the identification of an optimal animal model. Although sheep are commonly used in non-clinical fetal studies due to shared physiological similarities with humans, particular characteristics of this model have added to the challenges in the experiments. In humans, the uterus is located directly beneath the maternal abdomen, making the fetus more accessible and somewhat amenable to manipulation. In comparison, access to the fetal lamb is significantly limited in the sheep model due to the bicornuate ovine uterus, typically with overlying maternal bowels, and the common occurrence of multiple fetuses, all of which impair the ability to maneuver the fetus. Fetal lambs also have proportionally large limbs and hooves, which calcify at a relatively early gestational age [15], limiting the availability of treatment windows. In addition, the presence of fetal wool increases the likelihood of prefocal cavitation events. It is anticipated that such difficulties would be much less relevant in a clinical scenario.

Concern has been raised that fractionated tissue debris resultant from histotripsy therapy may become hazardous emboli. A separate *in vitro* study [16] was conducted to assess the size distribution of these tissue debris particles. Results showed no presence of particles greater than 60 µm in diameter, with > 80% of the particles less than 6 µm. Such particles are unlikely to form hazardous emboli, as 100 µm mechanical filters have been successful at preventing embolization in catheter-based thrombolysis procedures [17]. However, it is not known what size particles in a fetus can cause significant embolization. To further investigate the embolization risk, post-procedure diffusion weighted MRI and pathology analysis of fetal end organs including the brain, lungs and kidneys are planned for future experiments.

This feasibility study in the sheep model demonstrated that extracorporeal histotripsy therapy can induce localized tissue fractionation in fetal organs. These initial results demonstrate the potential of this technique, but it is clear that fetal histotripsy will require further refinement in order to become a viable tool for fetal intervention applications. Future studies will focus on improving the treatment consistency and accuracy in order to demonstrate the safety and efficacy of the technology.

4.5 References

[1] M. Heron, D. L. Hoyert, S. L. Murphy, J. Xu, K. D. Kochanek, and B. Tejada-Vera, "Deaths: final data for 2006," *National vital statistics reports,* vol. 57, pp. 1-134, 2009.

[2] D. B. McElhinney, A. C. Marshall, L. E. Wilkins-Haug, D. W. Brown, C. B. Benson, V. Silva, G. R. Marx, A. Mizrahi-Arnaud, J. E. Lock, and W. Tworetzky, "Predictors of technical success and postnatal biventricular outcome after in utero aortic valvuloplasty for aortic stenosis with evolving hypoplastic left heart syndrome," *Circulation,* vol. 120, pp. 1482-90, Oct 13 2009.

[3] E. S. Selamet Tierney, R. M. Wald, D. B. McElhinney, A. C. Marshall, C. B. Benson, S. D. Colan, E. N. Marcus, G. R. Marx, J. C. Levine, L. Wilkins-Haug, J. E. Lock, and W. Tworetzky, "Changes in left heart hemodynamics after technically successful in-utero aortic valvuloplasty," *Ultrasound Obstet Gynecol,* vol. 30, pp. 715-20, Oct 2007.

[4] D. B. McElhinney, W. Tworetzky, and J. E. Lock, "Current status of fetal cardiac intervention," *Circulation,* vol. 121, pp. 1256-63, Mar 16 2010.

[5] J. E. De Lia, R. S. Kuhlmann, T. W. Harstad, and D. P. Cruikshank, "Fetoscopic laser ablation of placental vessels in severe previable twin-twin transfusion syndrome," *Am J Obstet Gynecol,* vol. 172, pp. 1202-8; discussion 1208-11, Apr 1995.

[6] E. J. Grethel, A. J. Wagner, M. S. Clifton, R. A. Cortes, D. L. Farmer, M. R. Harrison, K. K. Nobuhara, and H. Lee, "Fetal intervention for mass lesions and hydrops improves outcome: a 15-year experience," *J Pediatr Surg,* vol. 42, pp. 117-23, Jan 2007.

[7] F. E. Avni, A. Massez, and M. Cassart, "Tumours of the fetal body: a review," *Pediatr Radiol,* vol. 39, pp. 1147-57, Nov 2009.

[8] B. Paek, J. Foley, V. Zderic, F. Starr, L. E. Shields, and S. Vaezy, "Selective reduction of multifetal pregnancy using high-intensity focused ultrasound in the rabbit model," *Ultrasound Obstet Gynecol,* vol. 26, pp. 267-70, Sep 2005.

[9] B. W. Paek, S. Vaezy, V. Fujimoto, M. Bailey, C. T. Albanese, M. R. Harrison, and D. L. Farmer, "Tissue ablation using high-intensity focused ultrasound in the fetal sheep model: potential for fetal treatment," *Am J Obstet Gynecol,* vol. 189, pp. 702-5, Sep 2003.

[10] Z. Xu, G. Owens, D. Gordon, C. Cain, and A. Ludomirsky, "Noninvasive creation of an atrial septal defect by histotripsy in a canine model," *Circulation,* vol. 121, pp. 742-9, Feb 16 2010.

[11] Z. Xu, A. Ludomirsky, L. Y. Eun, T. L. Hall, B. C. Tran, J. B. Fowlkes, and C. A. Cain, "Controlled ultrasound tissue erosion," *IEEE Trans Ultrason Ferroelectr Freq Control,* vol. 51, pp. 726-36, Jun 2004.

[12] T. L. Hall, K. Kieran, K. Ives, J. B. Fowlkes, C. A. Cain, and W. W. Roberts, "Histotripsy of rabbit renal tissue in vivo: temporal histologic trends," *J Endourol,* vol. 21, pp. 1159-66, Oct 2007.

[13] A. M. Lake, T. L. Hall, K. Kieran, J. B. Fowlkes, C. A. Cain, and W. W. Roberts, "Histotripsy: minimally invasive technology for prostatic tissue ablation in an in vivo canine model," *Urology*, vol. 72, pp. 682-6, Sep 2008.

[14] G. E. Owens, R. M. Miller, S. T. Owens, S. D. Swanson, K. Ives, G. Ensing, D. Gordon, and Z. Xu, "Intermediate-term effects of intracardiac communications created noninvasively by therapeutic ultrasound (histotripsy) in a porcine model," *Pediatr Cardiol*, vol. 33, pp. 83-9, Jan 2012.

[15] N. S. Ahmed, "Development of forelimb bones in indigenous sheep fetuses," *Iraqi J Vet Sci*, vol. 22, pp. 87-94, 2008.

[16] Z. Xu, Z. Fan, T. L. Hall, F. Winterroth, J. B. Fowlkes, and C. A. Cain, "Size measurement of tissue debris particles generated from pulsed ultrasound cavitational therapy-histotripsy," *Ultrasound Med Biol*, vol. 35, pp. 245-55, Feb 2009.

[17] M. K. Eskandari, "Cerebral embolic protection," *Semin Vasc Surg*, vol. 18, pp. 95-100, Jun 2005.

Chapter 5

Safety and Developmental Impact of Non-Invasive Fetal Histotripsy Therapy

This chapter discusses the safety aspects of non-invasive fetal histotripsy therapy to the maternal and fetal well-being for the remainder of the gestation, as well as the local developmental impact of histotripsy treatments on fetal organs in a sheep model. Non-invasive fetal kidney and liver treatments are conducted, and the ewes are allowed to complete the full gestation period under veterinarian observation. Acute and chronic results are compared and contrasted to evaluate the developmental response of fetal organs treated by histotripsy therapy.

5.1 Introduction

The initial feasibility study described in Chapter 4 has demonstrated that histotripsy therapy is capable of non-invasively generating precise lesions in fetal sheep heart, kidney and liver *in utero*, with no or minimal collateral damage to overlying tissue structures. Fetuses ranging from 102-129 days of gestation (full term: 150 days) were targeted and cavitating bubble clouds were successfully generated in 19 of 31 (61%)

treatment attempts, while in the remaining 12 cases (39%), cavitation clouds could not be generated. In those 12 cases, it was observed that bone structures, such as fetal limbs, were a substantial source of blockage for the acoustic pathway.

It was hypothesized that fetuses at a later stage of gestation were more likely to present obstructions to ultrasound therapy due to the higher degree of fetal bone development. This was a motivation to treat fetuses at an earlier gestation stage (95-107 days), when fetal bones are less calcified and less likely to cause ultrasound blockage. Furthermore, treatment at an earlier stage could be clinically desirable in cases where intervention has the potential to limit or stop the progression of certain abnormalities, such as lung masses.

Because of potential bioeffects of ultrasound on tissue, especially those near gas bodies, safety parameters such as the mechanical index have been developed and refined for diagnostic ultrasound [1, 2]. In the fetus however, the lungs and intestines are gas-free, presenting a rather unique situation. Several studies investigated pressure thresholds that induced acute hemorrhage in animal fetuses exposed to non-diagnostic, high ultrasonic fields. In one study [3], it has been observed that fluid-filled fetal tissues are significantly more resilient to lithotripter shockwaves of up to 20 MPa than gas-filled adult lungs and intestines. A separate investigation has shown that when fetal tissue was exposed to high amplitude shockwaves, superficial hemorrhage was more likely to be found at tissue boundaries near more developed bone, whereas soft tissue that was distant from such structures appeared relatively free of hemorrhagic events [4]. In the current study, the minimization of these untoward effects by reducing the impact of bone interfaces was also an incentive for treatment at earlier gestation stages, when fetal bones are less developed.

This study also attempted to improve the consistency of outcomes by treating fetuses within a narrower gestation window and by using fixed ultrasound exposure parameters during treatments.

Limited literature exists on non-invasive fetal intervention [5, 6] and long-term safety studies on large animal models exposed to this type of procedure have not been published. In this study, the treated fetuses were allowed to continue gestation to full term for the purposes of investigating potential safety issues during the course of pregnancy and delivery, as well as examining the longer term impact of the therapy in the treated organs after birth.

5.2 Methods

5.2.1 Histotripsy Treatment

Histotripsy treatment was administered by a 1 MHz focused ultrasound transducer with a diameter of 10 cm and a focal length of 9 cm, using a similar setup as described in Chapter 4. A total of nine ewes and ten lambs were treated, from 95 to 107 days into gestation (full gestation period: 150 days). The sheep were divided into a chronic group and an acute group. The five ewes and six lambs treated in the chronic group were allowed to continue gestation to full term after receiving treatment and samples were collected postpartum. In one case from the chronic group, twin lambs were treated, with each sheep receiving a single treatment. The four ewes and four lambs treated in the acute group were exposed to identical treatment parameters as the chronic group, but tissue samples were harvested immediately after the procedure.

Fetal kidney and liver were exposed to high-pressure (10-16 MPa peak negative pressure) histotripsy pulses at 1 MHz and 5 cycles (5 μs long), delivered at a repetition frequency of 500 Hz. Treatment depths ranged from 3 to 7 cm with respect to the external maternal abdominal wall. Therapy was administered by gradually increasing the acoustic power input until a hyperechoic bubble cloud was generated at the focus of the transducer. Once the initiation of the cavitation process was confirmed by ultrasound imaging, lesion volumes were created in the fetal liver and kidney by mechanically steering the therapy focus in a three dimensional grid in the shape of a cube of 5 mm on each side. A treatment grid of 125 spots (1 mm separation between spots) was distributed within this volume and each point was insonated for 4 seconds. The total treatment time for each ablation volume, including positioner movement delays, was approximately 10 minutes.

At most one kidney was treated in each lamb, leaving an untreated kidney for comparison purposes. In three of the four fetal lambs in the acute group, both the liver and kidney were treated. In the fourth lamb, only the liver was treated, as the location of the kidney was outside of the transducer’s reach. In the chronic group, all lambs with the exception of one case underwent a single treatment for either the liver or the kidney to minimize the risks of complications.

5.2.2 Post-Treatment Evaluation

After the procedure, the sheep in the chronic group were recovered and returned to their pen. A follow-up ultrasound imaging session was performed for each sheep a week after treatment to assess the condition of the fetuses. Periodic check-ups were conducted on the maternal sheep by the laboratory veterinarian (K.A.I.) for any signs of miscarriage.

Fetal viability was ultrasonically evaluated by the presence of a normal heart rate and contractility on the treated fetus and the absence of abdominal ascites. Once the fetus was confirmed to be viable, the sheep were then returned to the farm of origin, where the lambs were delivered at full term. The newborn lambs from the chronic group were visually evaluated by the in house veterinarian within a week after birth for any signs of external injury, abnormal behavior or distress. The fetuses in the acute group were harvested immediately after treatment.

Treated fetal organs were collected for gross evaluation and then embedded in a 1% agarose-based hydrogel for magnetic resonance (MR) scanning by a 7T small animal scanner (Varian Medical Systems, Inc. Palo Alto, CA). T2 weighted spin-echo images of the fetal kidney and liver were acquired along both coronal and axial planes. MRI parameters for each sample were adjusted within the following ranges to optimize lesion contrast and image signal-to-noise ratio (SNR) on a case by case basis. TR: 150-4000 ms. TE: 14-120 ms. Nex: 1-10. Field of View (FOV): (30-100) x (30-100) x (1-50) mm. Matrix Size: (32-256) x (32-256) x (1-50) voxels. Acquisition Time: 2-64 minutes. Matrix size and FOV were manipulated to enhance SNR. Spin-echo sequences were chosen because they can minimize potential artifacts caused by trapped air bubbles and T2* effects caused by the presence of deoxygenated blood. After the MR imaging procedure, the samples were fixed in 10% buffered formalin. Histological samples were processed with hematoxylin and eosin (H&E) staining for further analysis.

5.3 Results

A total of fifteen volume lesions were created in ten lamb fetuses. Hyperechoic bubble clouds were successfully generated at the therapy focus in all treatment attempts except for a single case (not included herein) in which the orientation of the fetuses precluded us from performing the procedure. In that specific case, the ewe was successfully awakened from anesthesia and no unusual after effects were noted. The ewe was eventually returned to the farm of origin, and the lambs were not sacrificed after birth.

In all other cases, as the treatment progressed and a larger volume of tissue was ablated, dark, hypoechoic zones consisting of homogenized tissue were observed to develop (Figure 5.1). Homogenized tissue has been shown to typically appear hypoechoic in comparison to intact tissue because of the reduced number and size of sound scatterers found in the fractionated region [7].

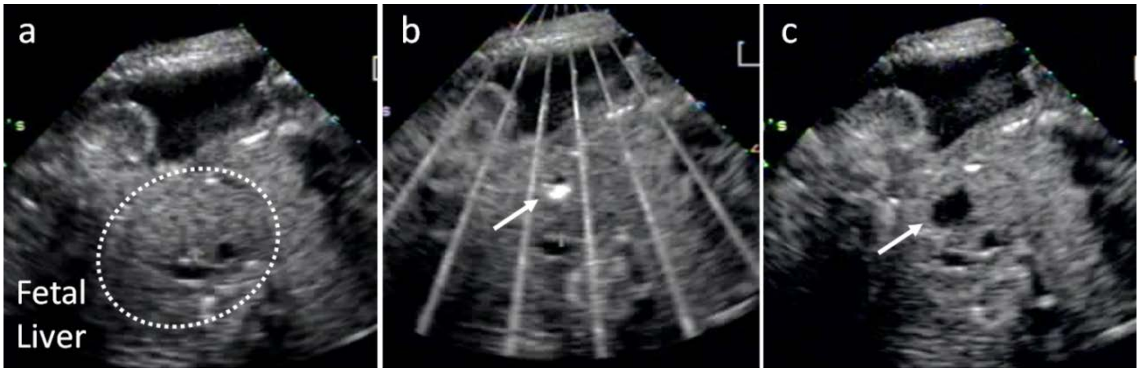

Figure 5.1 Representative B-mode ultrasound image of fetal liver before treatment (a). A highly echogenic bubble cloud was created at the focus during treatment as indicated by the arrow (b). The radial artifacts were caused by acoustic interference from the therapeutic pulses. A well-defined hypoechoic zone representing the ablated region was visible after treatment as shown by the arrow (c).

5.3.1 Lesion Morphology – Acute Group

Four liver lesions and three kidney lesions were created in four fetal lambs that were sacrificed immediately after treatment. The lesions were examined by gross inspection and MR imaging, and corresponded well to their anticipated locations observed by ultrasound. In the liver samples, MR scans showed that the main histotripsy lesions had a relatively higher (brighter) T2 signal compared to background, with shape and size correlating well with gross and histological evaluation (Figure 5.2).

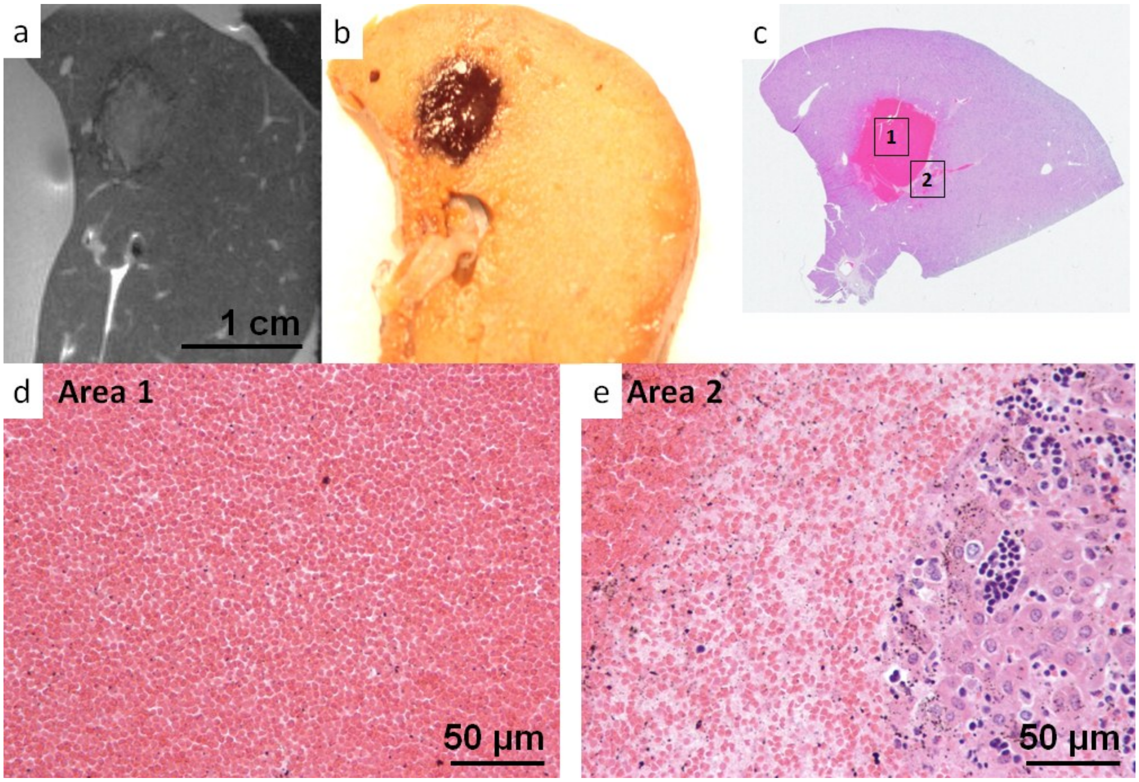

Figure 5.2 Acute aspect of a liver lesion under T2 weighted MRI (a), gross inspection (b), and H&E stained histology (c-e). Panels (d) and (e) represent magnified areas whose locations are indicated in panel (c). Acute liver lesions exhibited consistent fractionation of the targeted region which was characterized by the presence of acellular tissue debris and red blood cells (d) with well-defined lesion boundaries (e).

A darker contour was observed surrounding the lesion boundaries, which corresponded to the accumulation of deoxygenated red blood cells. Histological analysis indicated that the lesion had a completely homogenized center region consisting of acellular debris and red blood cells, exhibiting a clear boundary between fractionated and unfractionated tissue.

In the acute kidney samples, MRI and gross inspection showed darkened hemorrhagic regions caused by extravasated red blood cells (Figure 5.3). The darkened regions seen on T2 weighted images from MR scans appeared to closely follow the extent of the hemorrhage observed under gross inspection.

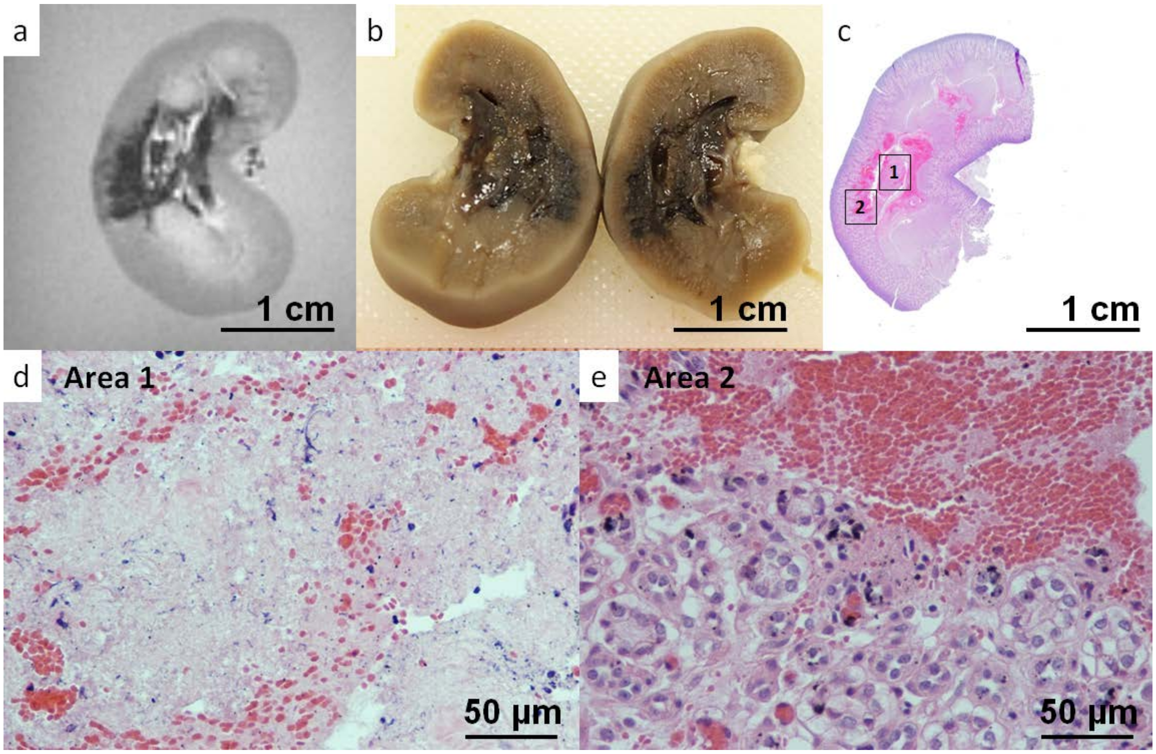

Figure 5.3 Acute aspect of a kidney lesion under T2 weighted MRI (a), gross inspection (b), and H&E stained histology (c-e). Panels (d) and (e) represent magnified areas whose locations are indicated in panel (c). Kidney lesions were characterized by the presence of hemorrhagic areas containing disrupted kidney tissue composed of acellular debris and necrotic tissue structures (d and e). Hemorrhagic products and fractionated tissue were observed to drain into the collecting system in some occurrences.

Histological analysis showed that the treated region was characterized by the presence of red blood cells and disrupted kidney tissue, which contained a mix of acellular debris and partially fractionated tissue structures. It was noted that in some instances, hemorrhagic products and acellular debris accumulated in the collecting system, possibly through the drainage paths made available by the kidney calyces.

5.3.2 Lesion Morphology – Chronic Group

All five ewes in the chronic group tolerated the treatment well, with none suffering early pregnancy termination. Transient fetal tachycardia during treatment was noted in a few cases, but eventually subsided once the procedure was completed. The lambs were delivered at full term (approximately two months after treatment) and appeared healthy, exhibiting no signs of external injury upon visual assessment.

Four liver lesions and four kidney lesions were generated in six lambs. Liver samples from the chronic group had no external defects and no noticeable evidence of scarring or trauma to the bulk tissue under gross morphology or MRI, despite the visualization of definitive hypoechoic lesions by ultrasound at the time of treatment. Histological samples taken from several locations throughout the liver also showed no abnormal cell formations within the hepatic tissue (Figure 5.4).

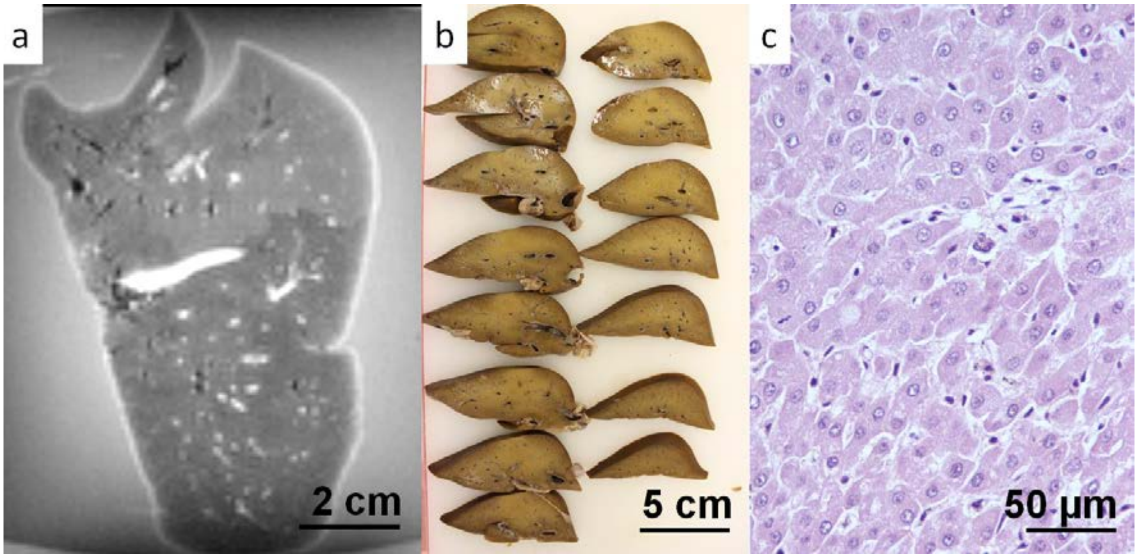

Figure 5.4 Representative images of a treated fetal lamb liver harvested after birth. No evidence of tissue injury was identified through T2 weighted MRI (a) or gross inspection (b). Histological samples obtained from several locations showed no signs of abnormal tissue formation (c).

Treated kidneys from the chronic group consistently displayed an externally visible contour defect presumed from loss of mass, which was not present in untreated kidneys from the same lambs (Figure 5.5). Histological examination indicated that the defect was surrounded by healthy kidney tissue with a border of fibrous tissue appearing to extend from the cortex to the collecting system. No indication of an ongoing inflammatory response was identified.

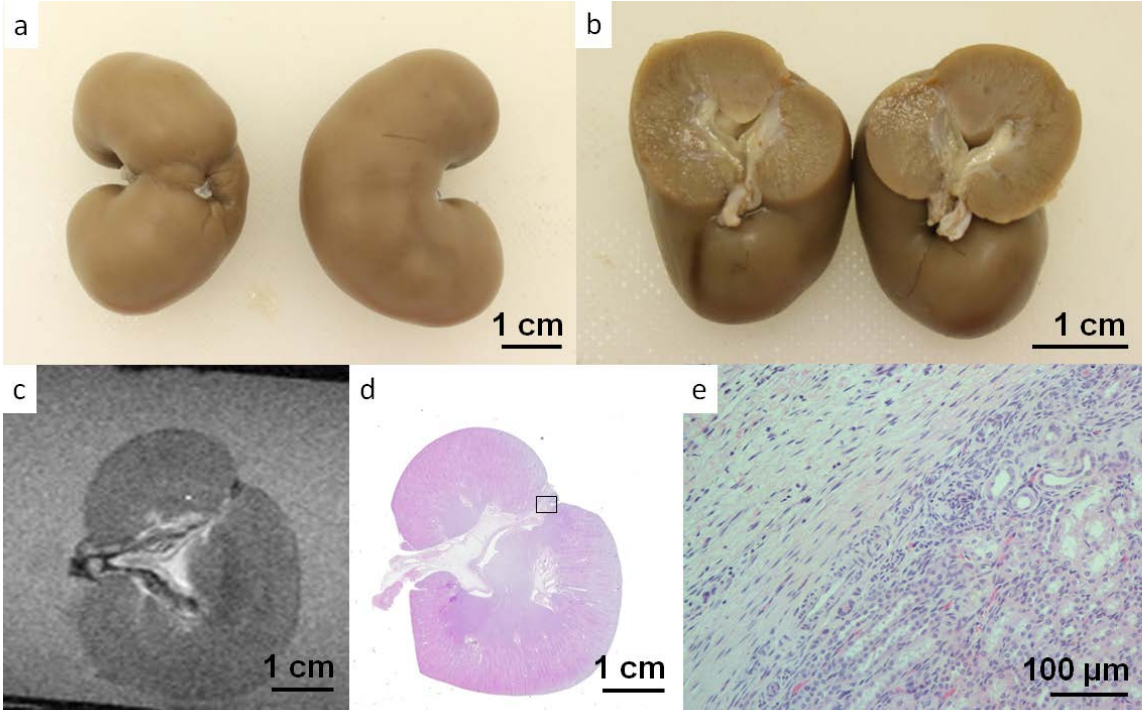

Figure 5.5 Representative images of a treated fetal lamb kidney harvested after birth. External aspect next to the untreated kidney from the same lamb (a). Cross sectional view (b) and T2 weighted MRI scan (c) of the contour retraction (indentation) found in the treated kidney. Histological analysis indicated a minor presence of fibrous tissue in the center of the defect surrounded by healthy kidney tissue (d and e).

5.4 Discussion

The goals of this study were to investigate the safety of fetal histotripsy therapy in the course of the pregnancy and its impact on the development of treated organs. Fetal liver and kidney were treated at 95 to 107 days of gestation, which corresponds to a human gestation stage near the late second or early third trimester. In the initial feasibility study discussed in Chapter 4, histotripsy lesions were also generated in the heart and lungs of the lamb, but treatment consistency was more limited for these organs by obstruction from the ribcage, in addition to long fetal limbs and other anatomical particularities of the sheep model. Hence, fetal liver and kidney were generally more accessible for treatment due to their position in the abdomen. Furthermore, fetal liver and kidney would allow the creation of lesion volumes, a process that would be useful in the treatment of fetal tumors.

In the animals recovered postpartum, no signs of external injury were observed in the treated lambs and no pregnancy related complications were reported in the maternal sheep. Treated livers and kidneys showed no evidence of hemorrhage, and the healthy condition of the tissue surrounding the treatment region suggested complete resolution of any inflammatory response by the time of delivery. The absence of any morphological signs of damage in the chronic liver samples likely indicates that the fractionated tissue was resorbed and the volumetric defect replaced by normal hepatocytes and liver parenchyma, which is not surprising, considering the highly regenerative nature of the liver in the developing fetus [8]. The deformations observed in the treated fetal kidneys harvested after birth indicate that the fractionated acellular tissue resultant from histotripsy therapy was dissipated or resorbed, which is consistent with a previous study concerning histotripsy kidney therapy in adult rabbits [9].

In the acute treatment group, lesion dimensions created by steering the focus of the transducer were observed to be larger than the total scanned volume (5 mm cubes), spanning up to 8-10 mm in some cases. This was a predictable outcome, as the dimensions of the bubble clouds imaged in ultrasound were approximately 3-4 mm in diameter, which is comparable to the focal zone of the therapy transducer. Consequently, the actual ablated volume was expected to extend beyond the scan dimensions, as was indeed observed in the tissue samples harvested after treatment.

The effective size of the bubble cloud may vary depending on the insonation parameters used (such as pressure amplitude and PRF) and/or the type of tissue treated. While particular tissue characteristics can affect the bubble cloud initiation process, higher pressure amplitudes and PRF will, in general, result in a larger cavitation cloud [10]. The real-time imaging capability of histotripsy therapy enables the operator to adjust the dimensions of the bubble cloud to an extent, by making appropriate parameter changes for a given treatment scenario. Theoretically, higher precision could be achieved by using transducers that have a more focused geometry or have a higher operating frequency. However, the benefits of increasing the treatment frequency may be constrained by the increased attenuation, absorption and aberration effects from overlying tissues that could result.

Histological analysis showed that acute lesions in the liver generally exhibited more thorough tissue fractionation and sharper margins than those generated in the kidney, even though similar treatment parameters were used. The relative heterogeneity of the kidney, with a ubiquity of tubules and vessels could be a cause of this discrepancy. Previous studies have shown that tissues with higher mechanical strength such as the renal collecting system and major blood vessels may be significantly more resilient to histotripsy therapy [11, 12]. From one perspective, these distinct “fractionation thresholds” (i.e., the necessary therapy intensity/dosage to achieve full ablation) could be viewed as an advantage, since this characteristic would potentially allow histotripsy to selectively ablate undesired tissue (e.g.: tumors or malformations) while sparing critical structures such as major vessels [13].

In this study, treatment was administered by gradually increasing the acoustic power input until a bubble cloud was observed at the focus. As such, each exposure was delivered at a peak pressure level right above the cavitation threshold of the targeted tissue. It is challenging to determine the *in situ* focal pressure used in each treatment, as standard hydrophone measurements cannot be carried out *in utero* non-invasively, and fetal tissues at various stages of development may present different acoustic properties. The pressure range reported herein is an estimation of the focal pressures *in situ* based on treatment depth and an overlying tissue attenuation factor of 1 dB/cm/MHz [14] applied to pressure measurements previously obtained in free water. This approximation is limited, and does not account for additional obstructions by fetal limbs or other bone structures particular to the sheep model.

It is worth mentioning that while the treatment parameters have not necessarily been optimized for the current study, the acute lesions generated using the settings referenced herein, especially in the fetal liver, were remarkably sharper and displayed more consistent ablation in comparison to those obtained in the initial feasibility study, which were generated at half of the exposure time used in this study. The earlier and relatively narrower gestation window (95-107 days) at which the fetuses were treated may also have contributed in improving the repeatability of the experiments, as fetal bone was less developed and less likely to cause obstruction to the ultrasound therapy.

While fixed treatment parameters were used in this study for consistency and comparison purposes, treatment efficiency could be further improved if a set of optimized parameters suited for particular ablation procedures and/or tissue types were applied on a case by case basis. A previous study suggested that complete tissue homogenization, or breakdown of tissue structures to an acellular level, may not be a requirement to cause tissue necrosis, which could be achieved with fewer pulses and reduced treatment time [15]. Parameter optimization and treatment strategies will be further investigated in subsequent studies.

MRI may be a useful tool to more accurately assess the extent of regions affected by histotripsy therapy. The fractionated homogenate resultant from histotripsy treatment has been shown to appear hyper-intense due to the lengthening of the homogenate’s T2 decay time [16], which allows clear identification of histotripsy-generated lesions in post treatment tissue samples. A variety of MRI modalities such as diffusion weighted imaging and volumetric measurements of the affected regions are currently under investigation to improve methods for the characterization of different levels of tissue injury resulting from histotripsy therapy [17]. Extended MRI capabilities will also be helpful in evaluating the potential of emboli formation resulting from the treatment. While in this study we have not conducted a thorough analysis of fetal organs in search of emboli, a recent investigation involving cardiac ablation in neonate pigs has found no evidence of thromboembolic events caused by histotripsy treatment based on lung pathology and MRI of the brain [18].

5.5 References

[1] C. C. Church and W. D. O'Brien, Jr., "Evaluation of the threshold for lung hemorrhage by diagnostic ultrasound and a proposed new safety index," *Ultrasound Med Biol,* vol. 33, pp. 810-8, May 2007.

[2] R. E. Apfel and C. K. Holland, "Gauging the likelihood of cavitation from short-pulse, low-duty cycle diagnostic ultrasound," *Ultrasound Med Biol,* vol. 17, pp. 179-85, 1991.

[3] C. Hartman, S. Z. Child, R. Mayer, E. Schenk, and E. L. Carstensen, "Lung damage from exposure to the fields of an electrohydraulic lithotripter," *Ultrasound Med Biol,* vol. 16, pp. 675-9, 1990.

[4] D. Dalecki, S. Z. Child, C. H. Raeman, D. P. Penney, R. Mayer, C. Cox, and E. L. Carstensen, "Thresholds for fetal hemorrhages produced by a piezoelectric lithotripter," *Ultrasound Med Biol,* vol. 23, pp. 287-97, 1997.

[5] K. Ichizuka, S. Ando, M. Ichihara, T. Ishikawa, N. Uchiyama, K. Sasaki, S. Umemura, R. Matsuoka, A. Sekizawa, T. Okai, T. Akabane, and M. Kushima, "Application of high-intensity focused ultrasound for umbilical artery occlusion in a rabbit model," *Ultrasound Obstet Gynecol,* vol. 30, pp. 47-51, Jul 2007.

[6] B. Paek, J. Foley, V. Zderic, F. Starr, L. E. Shields, and S. Vaezy, "Selective reduction of multifetal pregnancy using high-intensity focused ultrasound in the rabbit model," *Ultrasound Obstet Gynecol,* vol. 26, pp. 267-70, Sep 2005.

[7] T. Y. Wang, Z. Xu, F. Winterroth, T. L. Hall, J. B. Fowlkes, E. D. Rothman, W. W. Roberts, and C. A. Cain, "Quantitative ultrasound backscatter for pulsed cavitational ultrasound therapy- histotripsy," *IEEE Trans Ultrason Ferroelectr Freq Control,* vol. 56, pp. 995-1005, May 2009.

[8] M. Patricolo, A. Zangari, N. Paolocci, F. Magni, M. P. Viola-Magni, L. A. Hernandez-Mena, L. Capuano, and M. Rivosecchi, "In utero partial liver resection in the rabbit model: a study on fetal tissue regeneration," *Fetal Diagn Ther,* vol. 12, pp. 232-5, Jul-Aug 1997.

[9] T. L. Hall, K. Kieran, K. Ives, J. B. Fowlkes, C. A. Cain, and W. W. Roberts, "Histotripsy of rabbit renal tissue in vivo: temporal histologic trends," *J Endourol,* vol. 21, pp. 1159-66, Oct 2007.

[10] Z. Xu, T. L. Hall, J. B. Fowlkes, and C. A. Cain, "Effects of acoustic parameters on bubble cloud dynamics in ultrasound tissue erosion (histotripsy)," *J Acoust Soc Am,* vol. 122, pp. 229-36, Jul 2007.

[11] A. M. Lake, Z. Xu, J. E. Wilkinson, C. A. Cain, and W. W. Roberts, "Renal ablation by histotripsy--does it spare the collecting system?," *J Urol,* vol. 179, pp. 1150-4, Mar 2008.

[12] M. Cooper, X. Zhen, E. D. Rothman, A. M. Levin, A. P. Advincula, J. B. Fowlkes, and C. A. Cain, "Controlled ultrasound tissue erosion: the effects of tissue type, exposure parameters and the role of dynamic microbubble activity," in *Ultrasonics Symposium, 2004 IEEE,* 2004, pp. 1808-1811 Vol.3.

[13] E. Vlaisavljevich, Y. Kim, S. Allen, G. Owens, S. Pelletier, C. Cain, K. Ives, and Z. Xu, "Image-guided non-invasive ultrasound liver ablation using histotripsy: feasibility study in an in vivo porcine model," *Ultrasound Med Biol - Accepted,* 2013.

[14] I. R. Kamel, "An evaluation of overlying tissues to determine fetal exposure to ultrasound during the third trimester," *Ultrasound Med Biol,* vol. 20, pp. 41-51, 1994.

[15] T. L. Hall, C. R. Hempel, K. Wojno, Z. Xu, C. A. Cain, and W. W. Roberts, "Histotripsy of the prostate: dose effects in a chronic canine model," *Urology,* vol. 74, pp. 932-7, Oct 2009.

[16] T. L. Hall, L. Hernandez-Garcia, and C. A. Cain, "Relaxation properties of cavitation induced tissue lesions," *Proc Intl Soc Mag Reson Med,* vol. 15, p. 1118, 2007.

[17] S. P. Allen, W. W. Roberts, T. L. Hall, C. A. Cain, and L. Hernandez-Garcia, "Characterization of the in vivo histotripsy lesion using high field MRI," *Proc Intl Soc Mag Reson Med,* p. 1582, 2012.

[18] G. E. Owens, R. M. Miller, S. T. Owens, S. D. Swanson, K. Ives, G. Ensing, D. Gordon, and Z. Xu, "Intermediate-term effects of intracardiac communications created noninvasively by therapeutic ultrasound (histotripsy) in a porcine model," *Pediatr Cardiol,* vol. 33, pp. 83-9, Jan 2012.

Chapter 6

Supra-Intrinsic Threshold Sonication for Transcranial Histotripsy Therapy

This chapter explores the feasibility of performing transcranial histotripsy therapy through an intact skull using a novel sonication strategy involving extremely short, high peak rarefactional "supra-intrinsic threshold" pulses. Transcranial acoustic aberration effects are evaluated using an *ex vivo* human skull, and tissue samples are treated transcranially to assess the degree of ablation precision that may be achieved with short pulse histotripsy. Potential therapeutic advantages of using this sonication strategy and further improvements for transcranial histotripsy applications are discussed.

6.1 Introduction

The concept of using high intensity ultrasound for brain therapy has been explored since the 1940s, and early investigations by independent groups studied the biological effects of exposing the brain and nervous tissue of small animals to high intensity sonications [1-5]. In order to allow sufficient acoustic transmission to the treatment focus, craniotomies had to be performed in those experiments due to the highly attenuative nature of the skull bone. For several decades, the skull was considered a major limiting factor for ultrasound brain therapy, restricting the clinical applicability of such a treatment modality. But non-invasive therapy approaches were eventually suggested and studied in the 1970s [6, 7], and subsequent technological advances in transducer fabrication methods and high power electronics resulted in the advent of ultrasound array systems, opening a new phase in ultrasound brain therapy research. Major efforts in this field have explored a variety of non-invasive therapy possibilities for diverse applications such as tumor ablation, treatment of brain disorders, thrombolysis and drug delivery with promising results [8-10]. At the time of this writing, initial clinical trials for essential tremor and Parkinson's disease were underway with FDA approval in the United States.

The main difficulties encountered in non-invasive ultrasound brain therapy are the aberration and attenuation effects from the presence of the skull in the acoustic field. The non-uniform thickness and composition of the skull can cause significant phase variations to appear in the ultrasound beam, which can severely distort the therapeutic focus and hinder the effectiveness of the treatment. Recent studies have made extensive use of non-invasive of computer tomography (CT) or magnetic resonance (MR) imaging technologies to determine the geometry and thickness of the skull in order to compensate for the acoustic distortion effects caused by its presence [11, 12]. Significant efforts have been dedicated to the refinement of these techniques, alongside the development of large high intensity focused ultrasound (HIFU) phased array transducers powerful enough to cope with the high levels of beam attenuation introduced by the skull [13-16].

Another challenge in transcranial ablation therapy is the need to avoid undesired bone overheating effects while delivering a sufficiently high thermal dose at the focus of the treatment to cause tissue necrosis. Due to the high degree of ultrasound absorption in bone, temperature levels on the bone surface need to be carefully monitored during sonication to prevent thermal damage to the outer layers of brain tissue. To address this problem, current systems employ a method of active cooling of the scalp by continuous circulation of refrigerated water, which has been shown to significantly help in reducing the skull temperatures in comparison to passive cooling approaches [17, 18]. However, even with an active cooling system in place, the amount of ultrasound power applied transcranially may need to be restricted in certain cases to prevent damage to the surface of the brain through thermal conduction from the skull [12].

To reduce the overheating effects associated with purely thermal ablation methods, cavitation therapy has been previously proposed as a possible alternative to thermal ablation for transcranial therapy applications in a study by Hynynen and Jolesz [19]. In their study, HIFU pulses of 200 ms repeated at 1 Hz (20% duty cycle) for 10 s were applied to rabbit brain tissue through a human skull cap at focal pressure amplitudes of 8 MPa. The study concludes that the damage was caused by cavitation, as the estimated focal thermal dose was calculated to be too low to induce tissue damage by itself. More recently, a study by Gateau et al. suggested that at lower duty cycles, the cavitation thresholds in live sheep brain may be considerably higher, in the range of over 20 MPa for reliable cavitation events to be detected using 16 to 25 bursts of two-cycle pulses at 660 kHz [20].

Histotripsy therapy uses high pressure, short (< 10 cycles) pulses to fractionate tissue using precisely controlled, dense and energetic cavitation bubble clouds. Histotripsy has been shown to be a versatile treatment modality, being highly robust to even severe transmission aberrations, producing well confined lesions as long as the main focal beam above the cavitation pressure threshold is undistorted and secondary pressure lobes remain below the threshold [21]. Histotripsy treatments are also much less likely to induce overheating effects in overlying tissue since sonication settings may be set to arbitrarily low duty cycles and still be able to initiate cavitation, provided that sufficient pressure is available at the focus. These characteristics make histotripsy desirable for transcranial therapy applications and were the principal motivation behind this feasibility study.

While histotripsy therapy has been researched for a wide range of applications in recent years, [22-27] until the present investigation, transcranial histotripsy therapy could not be explored in depth because of a lack of transducers powerful enough to satisfy the high instantaneous focal pressure requirements to initiate cavitation bubble clouds transcranially. The skull represents a particularly challenging obstacle for traditional histotripsy therapy using the shock scattering cavitation initiation mechanism [28]. In the shock scattering initiation process, a high-amplitude shockwave reflection from single microbubbles created by the initial cycles of the histotripsy pulse constructively interferes with rarefactional cycles of the incident wave, resulting in large negative pressures and generating a dense layer of bubbles behind the initial microbubbles. Each subsequent positive cycle repeats the process and generates a new layer of bubbles opposite the ultrasound propagation direction, until the pressure falls below the cavitation cloud initiation threshold. In transcranial therapy, the skull surface can act as an acoustic low pass filter, aggressively attenuating the non-linear high frequency harmonic components necessary to achieve a large compressional shock front, therefore restricting the probability of cavitation initiation by the shock scattering mechanism.

In a recent study, Maxwell et al. [29] investigated the pressure thresholds necessary to initiate cavitation clouds using a single pulse of 2 cycles. The cavitation initiation probability was observed to follow a sigmoid curve with respect to the peak rarefactional pressures available at the focus. In samples with high water content (water, gel phantoms and most soft tissues), the statistical cavitation threshold corresponding to a 50% probability for initiation of dense bubble clouds was reached at peak rarefactional pressures of 26-30 MPa. This was defined as the "intrinsic threshold" of the medium. The very short, high intensity pulse histotripsy regime generates dense bubble clouds that are more consistent and predictable with minimal shock scattering, as long as part of the negative cycle of the pulse exceeds the intrinsic threshold. Moreover, as a smaller part of the negative cycle exceeds the threshold, the smaller the cloud and the resulting lesion, allowing precise control of lesion generation. If only a small part of the pulse exceeds the intrinsic threshold, clouds as small as a single bubble can be generated, producing very small lesions, even at low operational frequencies. By using shorter pulses, the probability of generating cavitation outside the focus, e.g., at the skin/skull interface, or lateral to the therapy focus, is also reduced in comparison to using longer pulses through the shock scattering mechanism.

To achieve such focal pressure levels through the intact skull, a high gain, large aperture, 32 element hemispherical array was specifically designed for this study using rapid prototyping technology. While focal steering and high resolution aberration correction is limited by the small number of elements, this configuration allowed us to increase directivity to maximize focal gain. The low element count minimized hardware requirements (and cost) while allowing sufficient coarse phase corrections to be performed to partially compensate for large skull aberration effects.

The main objectives in this investigation were to demonstrate the feasibility of using short, supra-intrinsic threshold histotripsy pulses for non-invasive tissue ablation through the skull, and evaluate the degree of precision that may be achievable in lesions generated transcranially. Therefore, this report refrains from extensively discussing specific clinical and safety issues that could potentially arise from using this therapy modality in the brain. Such issues will need to be carefully and extensively investigated with further studies. This chapter describes initial results and introduces the concept of transcranial histotripsy therapy, which could have potentially useful applications for non-invasive brain treatment, by eliminating its susceptibility to focal heat sinks and minimizing the thermal impact to the skull.

6.2 Experiment Setup

The transducer used in this study was specifically designed to achieve high focal gain and was fabricated using rapid prototyping technology. Detailed descriptions of the design and fabrication of this array can be found in Appendix C of this dissertation. Focal pressure profiles were mapped with a high sensitivity hydrophone (model HNR-0500, Onda Corp., Sunnyvale CA). To prevent cavitation damage to the piezoelectric hydrophone, high pressure focal calibration measurements were conducted with a separate fiber optic probe hydrophone designed and built in-house. Cavitation bubble clouds were optically imaged using a high-speed, 1 megapixel CCD camera, (Phantom V210 - Vision Research, Wayne, New Jersey, USA). The camera was focused through a macro lens (Tominon 105 mm f/4.5 Kyocera Corp., Japan) and folding optical bellows (Nikon Corp., Japan). The imaging was performed through the 41 mm glass windows available at the side of the array in a backlit configuration (Figure 6.1)**.**

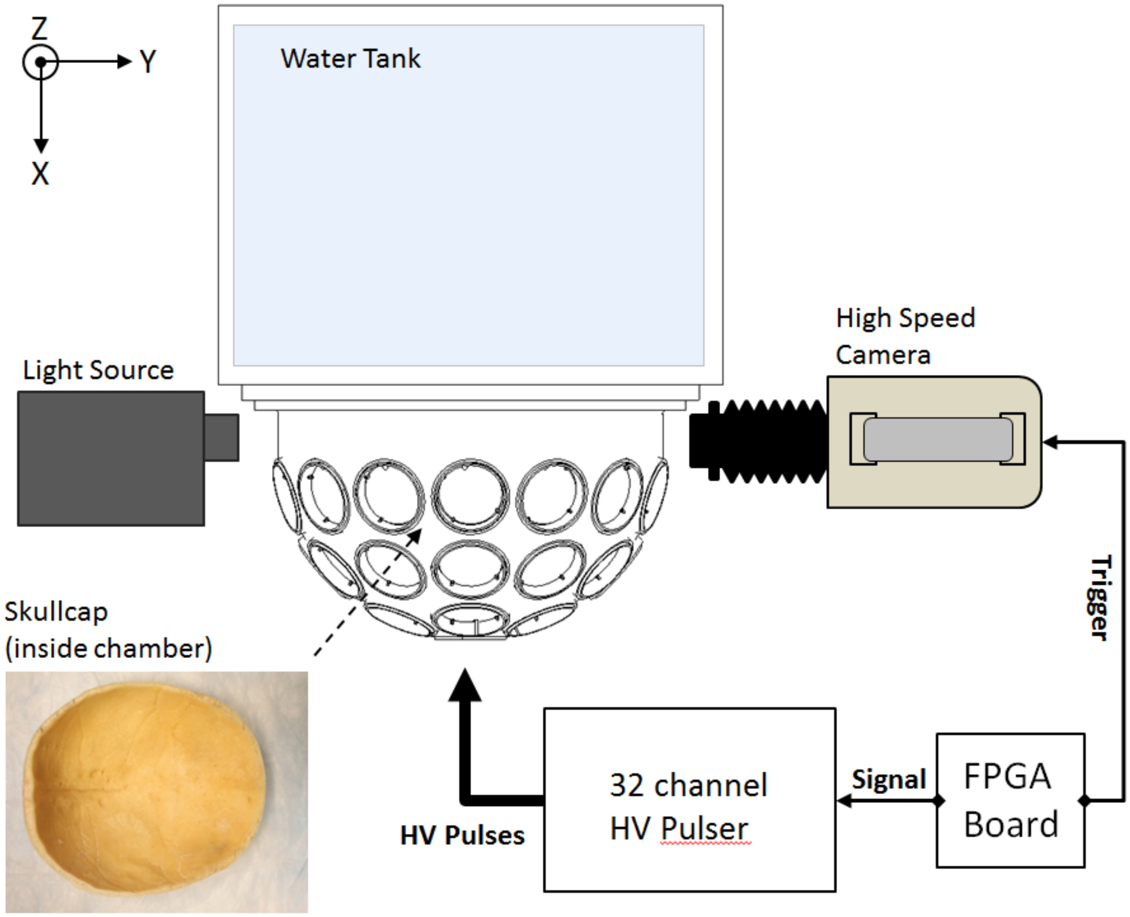

Figure 6.1. Illustration of the experimental apparatus (top view) used to collect high speed optical images of the bubble clouds. The skull cap was positioned inside the hemispherical array chamber, which was driven with a high voltage pulser. A custom programmed FPGA board was used to synchronize the high speed camera shutter with the therapy pulses. The orthogonal coordinates displayed in the figure are used as convention.

6.2.1 Sample Preparation

Transcranial experiments were conducted with a human cadaver skull cap sample obtained through the University of Michigan Anatomical Donations Program. From the time of extraction, the sample had been continuously kept in 10% buffered formalin and prior to the experiments, the sample was degassed inside a vacuum chamber for one day. Following this process, the skull cap was carefully positioned inside the hemispherical transducer tank, which had been pre-filled with degassed water (Figure 6.2).

Red blood cell (RBC) agarose tissue phantoms developed in house were used to assess the dimension of histotripsy lesions produced through the skull cap. The phantom was molded into a rectangular support frame with 5 open sides specifically fabricated to allow ultrasound transmission towards the focus from all incident angles of the hemispherical array. The gel phantom consists of a thin layer of < 500 μm red blood cells (RBC) sandwiched between agarose gel blocks (Figure 6.3). When exposed to cavitation, the cells in the RBC layer lyse and the treated region changes from opaque red to translucent, allowing direct visual inspection of the damaged area immediately after treatment. This phantom has been previously described and used as an indicator of cavitation damage caused by histotripsy in tissue [30].

Ex vivo canine liver samples were also prepared for transcranial ablation for further validation purposes. The samples were collected from dogs in an unrelated study and were used within 6 hours from the harvesting procedure. All procedures have been reviewed and approved by the University Committee on Use and Care of Animals at the

University of Michigan. Prior to the experiments, each tissue sample was initially degassed in room temperature saline (0.9% NaCl solution) under a vacuum chamber for several hours. After the degassing period, the samples were sectioned in smaller blocks and embedded in a 1% agarose hydrogel in a similar support frame as that used in the RBC tissue phantom experiments.

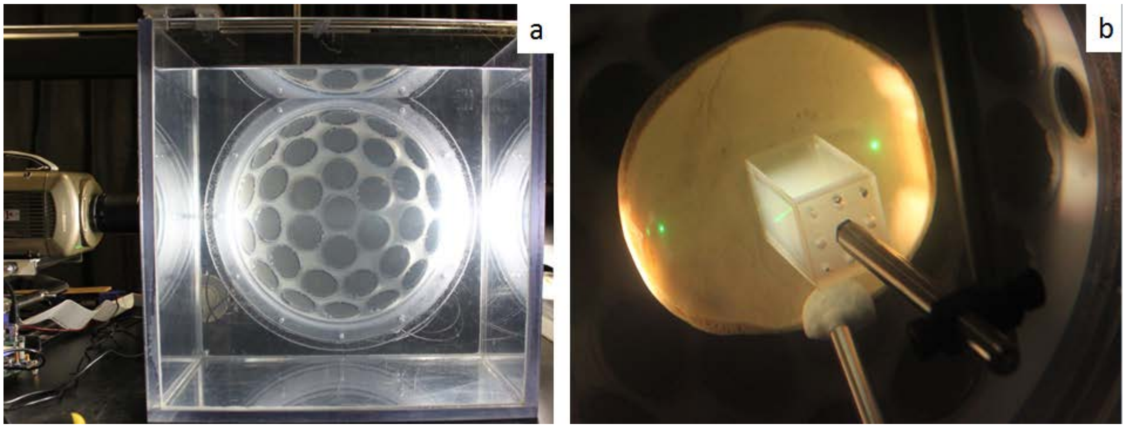

Figure 6.2. Frontal view of the hemispherical array with the high speed camera aligned at the therapy focus for optical cavitation imaging (a). Skull cap sample positioned inside the transducer chamber with an agarose phantom (b). Low power green laser pointers were used for alignment purposes.

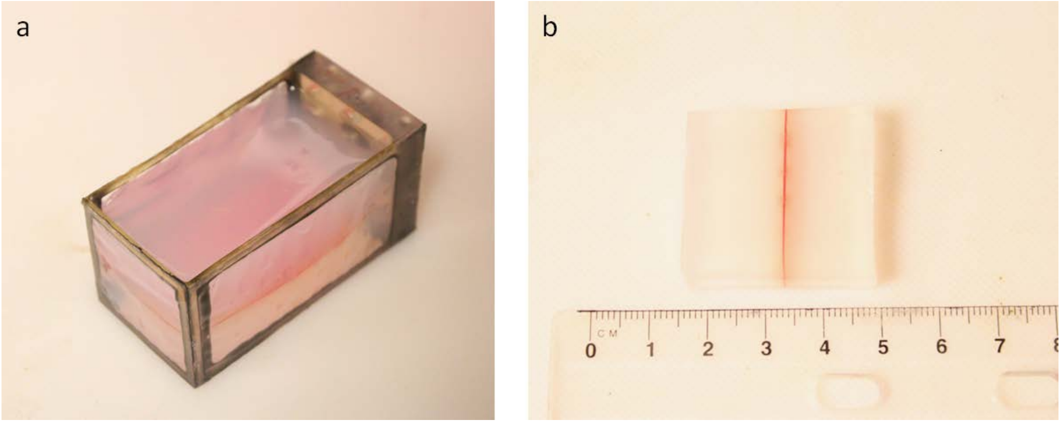

Figure 6.3. Red blood cell (RBC) tissue phantom as molded in the open holder frame (a). Transversal cross section view of the RBC phantom showing its three-layered architecture (b). The thin middle layer (< 500 µm) consists of red blood cells which allow the extent of histotripsy-induced damage to be readily identifiable after treatment.

6.2.2 Pressure Measurements and Phase Alignment

Pressure insertion losses through the skull cap were obtained by comparing transcranial focal pressure measurements with respect to free field focal pressures (without the skull cap) at a fixed sonication setting. This fixed power setting was at a peak pressure of approximately 20 MPa in free field, which was near the maximum that could be reliably measured without initiating cavitation at the tip of the hydrophone. Transcranial pressure measurements were normalized with respect to free field readings to estimate the overall focal pressure attenuation introduced by the presence of the skull. The spatial focal pressure profiles were also collected along three orthogonal axes (X, Y, Z), referencing the peak rarefactional pressures obtained at each location (Figure 6.1). Centered at the focus, scans of 40 mm were taken along the axial (X) direction, and 30 mm scans were obtained for the transversal (Y and Z) directions at a quarter wavelength resolution (500 µm).

With the skull cap still in place, phase correction was performed using a hydrophone positioned at the geometric focus of the transducer. A script written in MATLAB (The MathWorks, Inc., Natick, MA) was used to realign the arrival times of the pressure waveforms by measuring the time of flight signal from each of the 32 individual elements at the geometric focus of the array. The script interfaces a computer station with the FPGA signal generator board and uses a cross correlation algorithm to estimate the time of arrival differences among the ultrasound pulses from each element with respect to the center axial element in the transducer array in free field. Once the proper timing differences were calculated, the values were loaded to the FPGA signal generator, which allowed the necessary timing intervals to be resolved in units of 10 ns based on the FPGA’s internal clock frequency (100 MHz). Delay adjustments were calculated and applied prior to treatment in all experiments.

6.2.3 Histotripsy Treatment

All treatments were administered at an estimated focal peak rarefactional pressure of 29-30 MPa using short pulses (< 2 full cycles). This was slightly above the intrinsic cavitation threshold in water, allowing consistent bubble cloud initiation for every treatment pulse. Pulses were applied at a repetition frequency (PRF) of 1, 10 and 100 Hz, corresponding to effective sonication duty cycles of approximately 0.0004%, 0.004%, and 0.04%, respectively, based on a pulse length of 2 cycles at a center frequency of 500 kHz. At this intensity and pulse width, only a single negative half-cycle of the histotripsy pulse was likely to exceed the intrinsic cavitation threshold.

In the RBC phantoms, the thin blood layer was carefully aligned at the transducer focus with the aid of laser pointers prior to treatment. Lesions were created in the RBC layer by applying a total of 500 histotripsy pulses for each treatment. Images of the bubble clouds were collected as the lesion developed, with frames captured at approximately 5 us after the arrival of each pulse. Images were collected along the axial plane of the transducer (X-Z plane) through the optical windows in the hemispherical array shell to display the extent of the histotripsy damage profile.

In the liver tissue samples, lesions were generated using similar sonication settings as those applied in the RBC tissue phantom treatments, with 500 pulses applied for each treatment in the bulk tissue. After treatment, the samples were removed from the tissue holder frame and allowed to fix in a 10% buffered formaldehyde solution for several days. Histopathological analysis was later performed on the liver sections prepared with hematoxylin and eosin (H&E) stains.

6.3 Results

6.3.1 Pressure Waveforms and Profiles

Focal pressure measurements were collected to evaluate the amount of insertion loss introduced by the skull in comparison to free field conditions. Figure 6.4 shows a representative voltage pulse applied to the elements and the associated focal pressure measurement obtained in free field (without the skull). The maximum peak rarefactional pressure that could be directly measured by the hydrophone in degassed water was approximately 23 MPa. Beyond this level, cavitation bubbles were observed to consistently initiate at the tip of the hydrophone probe, yielding unreliable measurements. The peak rarefactional pressures used for treatments exceeded this value and were therefore estimated based on the summation of focal peak rarefactional pressures generated by individual elements driven at treatment power output levels.

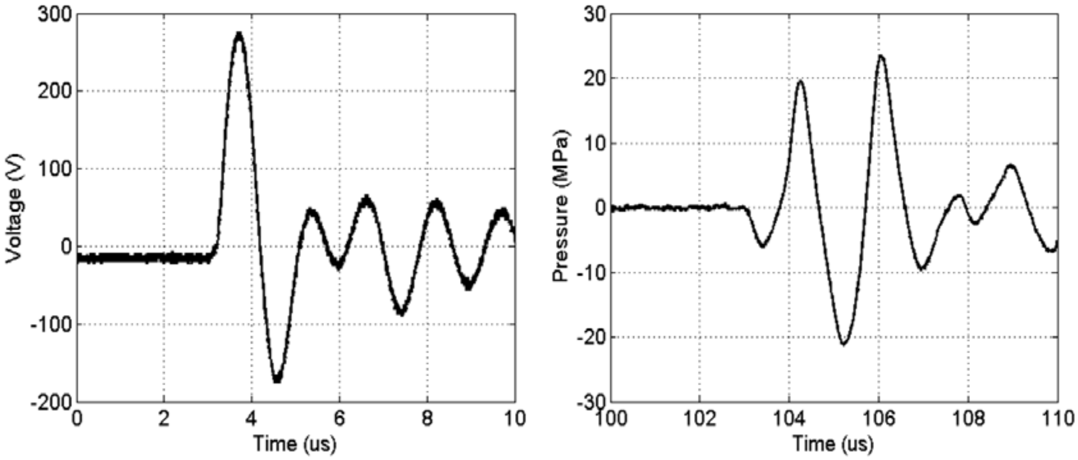

Figure 6.4. Representative voltage excitation pulse applied across the 32 transducer elements (left), and the resulting pressure measured at the geometric focus of the hemispherical array (right). Pressure levels beyond 23 MPa could not be measured reliably by the hydrophone due to the onset of cavitation at the measuring probe.

The presence of the skull cap significantly attenuated the peak rarefactional pressure at the focus to approximately 14% of the value obtained in free field which did not permit supra-intrinsic threshold cavitation clouds to be initiated even at the maximum output settings of the transducer. Transcranial focal pressure measurements were found to be temporally shifted towards the transducer by approximately 2 µs due the higher speed of sound in bone relative to water. Phase distortion from the thickness variation of the skull cap also significantly affected the spatial profile of the focal main beam, especially along the transversal coordinates, (Y and Z axes) in which its full width half maximum (FWHM) values more than doubled, respectively increasing to 4.3 mm and 5.2 mm from symmetrical free field values of 1.8 mm. The focal beam was also found to be spatially shifted by 0.5 mm in the axial coordinate (X axis), whereas its FWHM increased to 4.1 mm from a free field value of 3.9 mm.

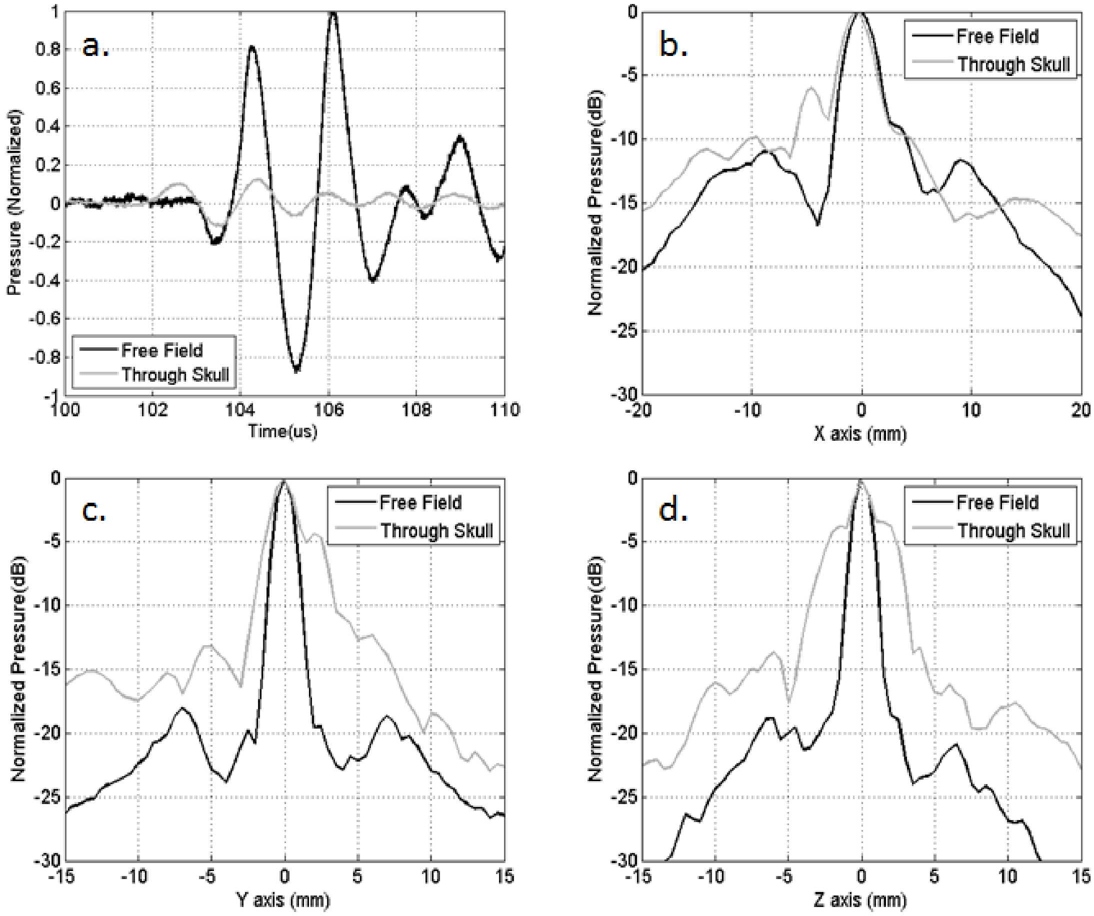

Figure 6.5. Pressure measurements at the geometric focus normalized with respect to free-field conditions. Normalized pressure waveforms measured at the focus in linear scale (a). Peak rarefactional pressure linear insertion losses exceeded 80% with the skull cap in place. Spatial peak rarefactional pressure distribution profiles near the focus (b-d). Phase shift effects introduced by the skull cap significantly distorted the main focal beam. Axial (X) and transversal (Y and Z) profiles are shown.

6.3.2 Phase Correction

Phase variations introduced by the skull were corrected by using a hydrophone placed at the geometric focus of the array. Each of the 32 elements was individually activated and measured in order to obtain a signal delay map across the all the elements of the transducer (Figure 6.6). Appropriate delay corrections for each element were applied to allow for simultaneous pulse arrival times at the focus. The timing corrections required to realign the waveforms ranged from approximately 0.2 to 2.3 µs with respect to free field measurements, with the majority of the delays falling within a 2 µs period.

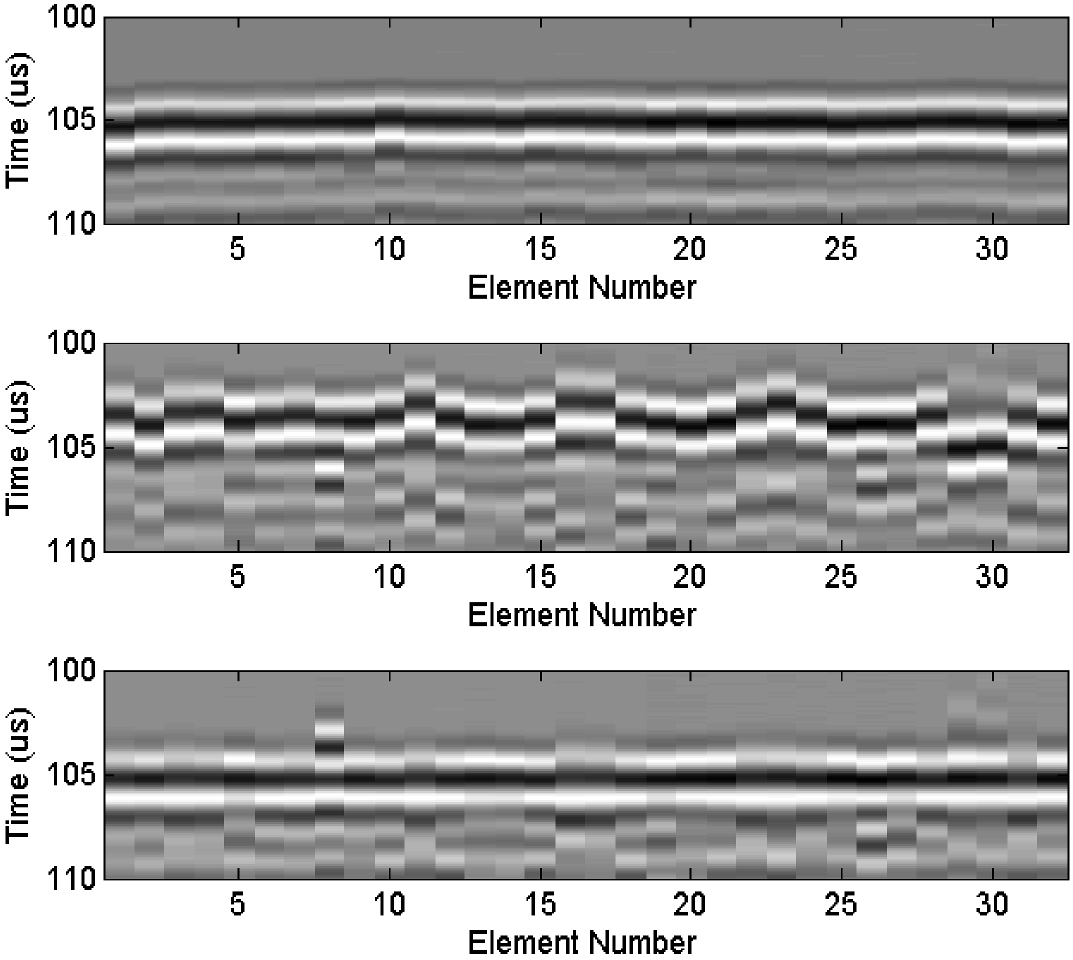

Figure 6.6. Acoustic signals measured from individual array elements at the geometric focus under free-field conditions (top row), through the skull cap (middle row), and through the skull cap after phase correction (bottom row). The majority of the timing delays required to realign the pulses fell within a 2 µs period.

Phase variations introduced by the skull were corrected by using a hydrophone placed at the geometric focus of the array. Each of the 32 elements was individually activated and measured in order to obtain a signal delay map across the all the elements of the transducer (Figure 6.6). Appropriate delay corrections for each element were applied to allow for simultaneous pulse arrival times at the focus. The timing corrections required to realign the waveforms ranged from approximately 0.2 to 2.3 μs with respect to free field measurements, with the majority of the delays falling within a 2 μs period.

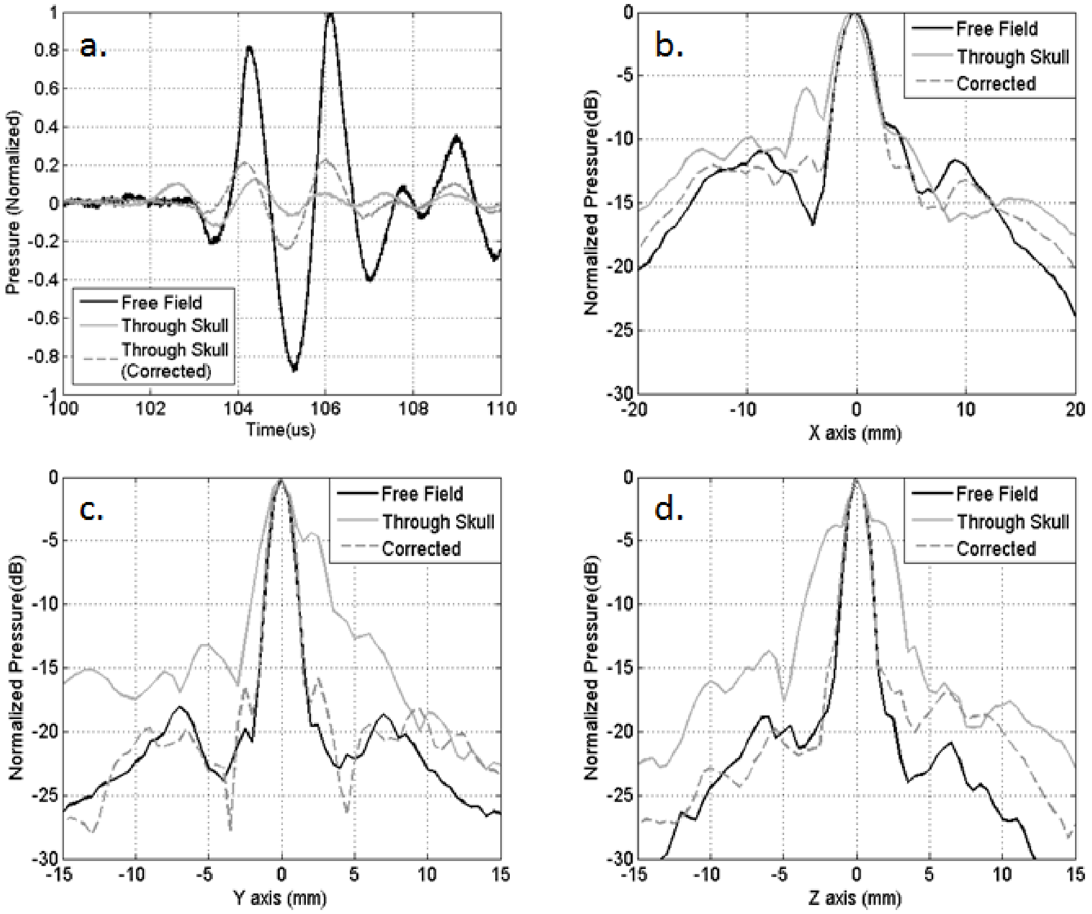

Figure 6.7. Focal pressure profiles measured through the skull before and after phase correction for the 32 elements was applied. Phase correction improved the peak rarefactional focal pressure by 97% in comparison to uncorrected measurements (a). Spatial pressure distribution profiles were also restored to good agreement with respect to free field profiles (b-d). Axial (X) and transversal (Y and Z) profiles are shown.

The 32 delay corrections were able to restore the transcranial main lobe focal profile FWHM to good agreement with free-field conditions (Figure 6.7b-d). Moreover, the peak rarefactional pressure at the focus was increased by a factor of 2, approximately reaching 28% of its reference value obtained in free field (Figure 6.7a) and allowing sufficient pressure transmission to the focus for the initiation of intrinsic cavitation bubble clouds.

6.3.3 Bubble Cloud Imaging

Transcranial cavitation bubble clouds were generated and imaged in RBC agarose tissue phantoms using the high speed camera setup described previously. Image frames were obtained at approximately 5 µs after the therapy pulse arrived at the focus. Figure 6.8 shows the longitudinal plane (X-Z plane) aspect of the cavitation bubble clouds generated at peak rarefactional pressures of approximately 29-30 MPa using PRF parameters of 1, 10 and 100 Hz. The bubble cloud initiation regions reported herein (n = 3) were obtained by measuring the zones in which cavitation bubbles were observed to be present for at least 10 pulses or more, a dosage that has been shown to be sufficient to induce tissue damage in a previous study [31].

Cavitation bubble clouds were consistently generated for every pulse in each case. Bubble clouds generated at a PRF of 1 Hz were observed to be the most confined, with a few bubbles undergoing consistent initiation within a central region with mean and standard deviation dimensions of 1.6 x 3.4 mm (± 0.3 x 0.7 mm). At the start of the treatment, peripheral cavitation bubbles were excited by the first few pulses. These peripheral “incidental” bubbles were observed to collapse and largely subside within the first 100 pulses at 1 Hz PRF. As the PRF was increased to 10 Hz, the focal region affected by cavitation initiation was observed to grow substantially larger, reaching 4.9 x 6.0 mm (± 1.5 x 0.5 mm), with peripheral bubbles lasting for as long as 200-300 pulses. Finally, at 100 Hz, the bubble cloud profile was less differentiable, as a conical region of up to 8 x 10 mm (± 0.7 x 0.9 mm) was observed to be affected by cavitation, with a large number of peripheral bubble nuclei. These incidental bubbles lasted through the entire duration of treatment. However, because of the short therapy pulses used (< 2 cycles) these bubbles did not scatter shockwaves from subsequent cycles. They remained single bubbles, which reduced the potential for further collateral damage.

6.3.4 Red Blood Cell Phantom Lesions

Lesions generated in red blood cell (RBC) layer were examined to evaluate the spatial fractionation profile of the cavitation bubbles generated through the skull cap. A total of 500 ultrasound pulses were applied for each treatment at three different PRF: 1, 10 and 100 Hz. Pressure levels at the focus were kept identical during all treatments and estimated at 29-30 MPa peak rarefactional.

A total of 9 lesions were generated in the RBC phantoms, with 3 lesions generated at each PRF setting. Lesions generated at lower PRF displayed more confined ablation near the focal zone and less collateral damage from incidental bubbles (Figure 6.8). At a PRF of 1 Hz, the mean and standard deviation of the lesion dimensions were approximately 0.9 x 1.9 mm (± 0.1 x 0.1 mm), in the transversal and longitudinal planes, respectively, approximately one half of the FWHM of the focal main beam of the transducer (1.8 x 3.9 mm). At a PRF of 10 Hz, the center lesion appeared to be slightly larger at 1.3 x 2.4 mm (± 0.2 x 0.1 mm) possibly due to increased bubble activity that was observed to occur adjacent to the boundary of the main lesion. The lesion profiles created at a PRF of 100 Hz displayed wider regions of incidental bubble damage surrounding main lesions of 0.8 x 1.7 mm (± 0.1 x 0.1 mm).

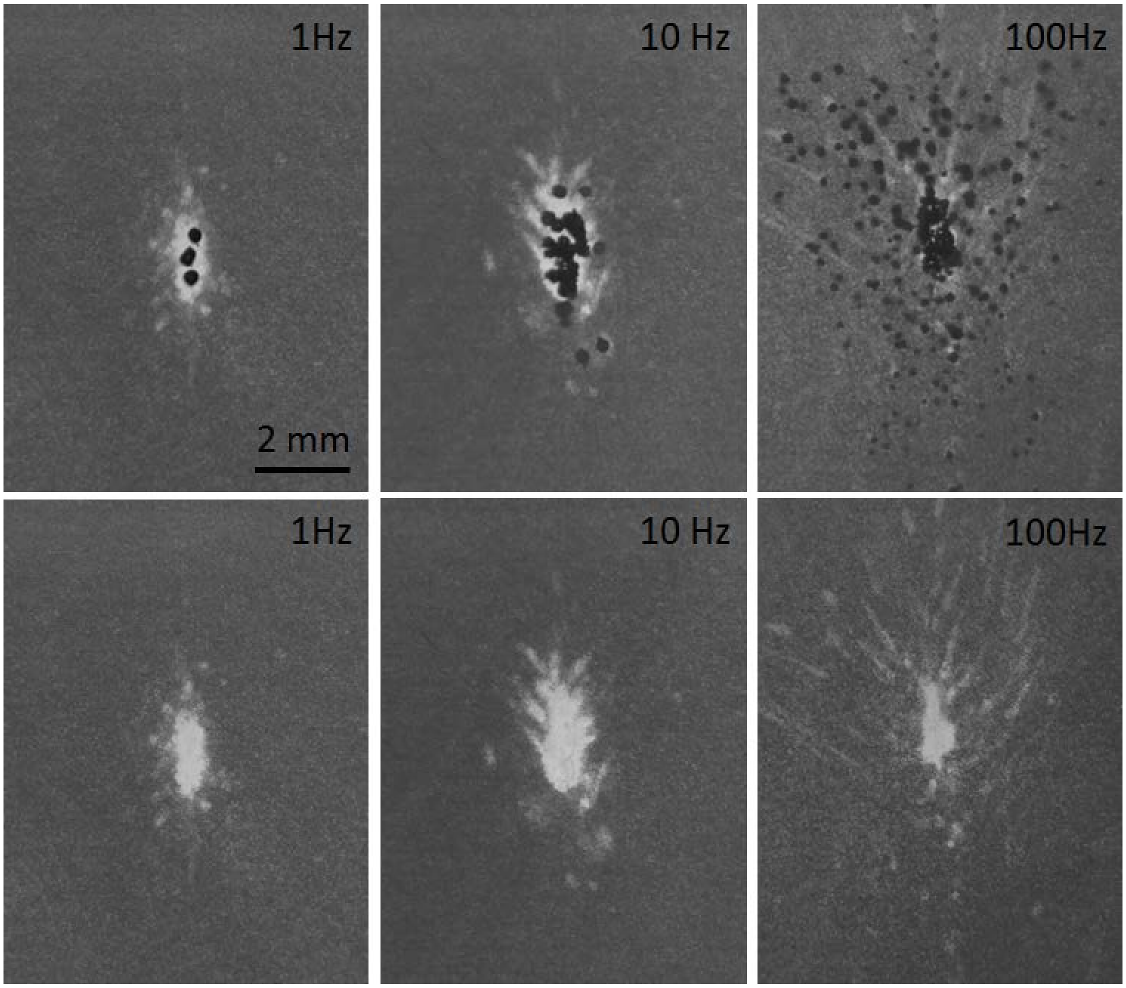

Figure 6.8. Transcranial lesion profiles generated in RBC phantoms at various pulse repetition frequencies (PRF). Top row: bubble clouds generated at the focus as visible near the end of the treatment. Bottom row: resulting lesions after sonication with 500 pulses. Treatments at higher PRF appeared to increase the amount of collateral damage observed in the resulting lesions. Longitudinal planes are shown. Ultrasound propagation: top to bottom.

6.3.5 Ex Vivo Liver Lesions

Additional transcranial lesions were generated in fresh canine liver tissue at similar treatment pressure levels with a total of 500 histotripsy pulses applied through the skull cap at pulse repetition frequencies of 1, 10 and 100 Hz. Figure 6.9 shows hematoxylin and eosin (H&E) stained histology samples of histotripsy lesions generated in bulk liver tissue through the skull. The lesions were characterized by a center region consisting of homogenized acellular debris surrounded by normal liver tissue. A total 3 lesions were generated in liver tissue, one at each PRF setting. At a PRF of 1 Hz, a single treatment lesion 0.5 x 1.2 mm was generated with sharp, well defined boundaries between the homogenized focal region and intact liver tissue. Collateral damage from incidental bubbles (in the form of adjacent injury lines) in treatments at higher PRF was not as noticeable as it was in the RBC phantoms. However, as the treatment PRF was increased, lesion boundaries were observed to become more irregular and less defined, with some instances presenting incomplete homogenization in the focal zone.

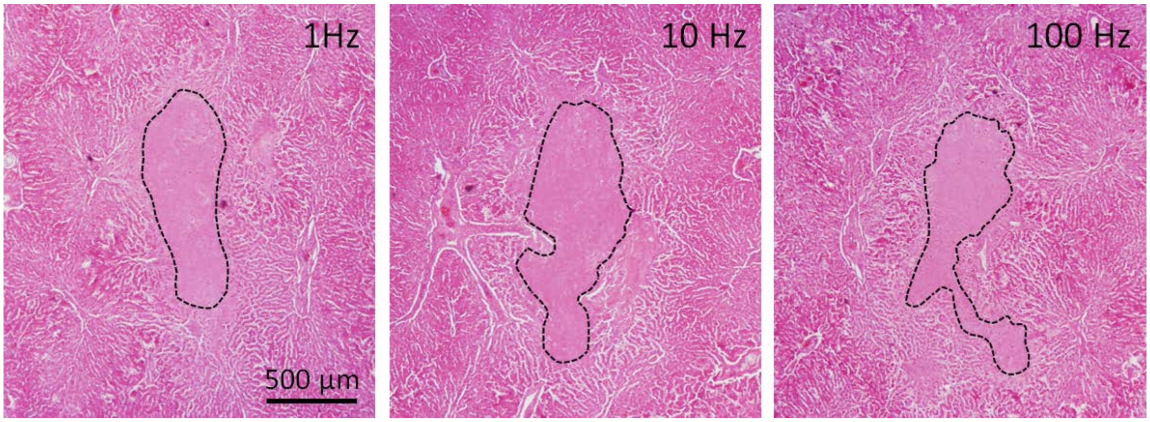

Figure 6.9. Representative H&E stained histology slides of transcranial lesions produced in ex vivo liver tissue. A total of 500 pulses were applied at pulse repetition frequencies (PRF) of 1, 10 and 100 Hz. Lesions were identified by the presence of a central area characterized by the presence of acellular homogenate as indicated by the dashed contours. As the PRF was increased, lesion boundaries became less defined, and ablation at the focal zone appeared to be less consistent.

6.4 Discussion

This study has demonstrated the feasibility of using short pulse (< 2 full cycles) histotripsy therapy to generate transcranial lesions through a human skull cap using a prototype 32-element 500 kHz hemispherical array transducer. Treatments in RBC tissue phantoms and canine liver samples indicated that lesion profiles with precise boundaries and dimensions significantly less than the FWHM of the focal main beam of the transducer could be generated transcranially by modulating the focal pressure near the cavitation threshold of the media with coarse (32 channel) aberration correction.

The “intrinsic threshold” cavitation cloud generation used in the present study is a recent development [29], which minimizes shock scattering effects in the cavitation bubble cloud initiation process [28]. By applying a single, short sonication pulse (< 2 cycles), a bubble cloud is consistently generated when the instantaneous peak rarefactional pressure exceeds the inertial cavitation threshold intrinsic to the medium, resulting in more confined and uniform bubble clouds in comparison to those produced by the shock scattering mechanism. This allows the therapy to achieve a greater degree of bubble cloud control.

As evidenced by this study, sub-wavelength ablation precision may be achieved through the skull using the intrinsic threshold mechanism by modulating the extent of the peak rarefactional focal beam profile that exceeds the cavitation threshold of the treatment medium. In this manner, small, ablative cavitation clouds consisting of a few bubbles (or even a single bubble) may be achieved, and the extent of cavitation damage can be predicted by knowledge of the spatial rarefactional pressure distribution of the field, a feature that would significantly aid treatment planning. Results from a separate, ongoing investigation support this observation, showing that lesion sizes produced by the intrinsic threshold mechanism correlate well with the dimensions of the rarefactional pressure beam width estimated to exceed the intrinsic cavitation threshold.

The higher level of cavitation control afforded by this intrinsic threshold strategy opens new possibilities for non-invasive histotripsy therapy. In this study, coarse phase correction was performed primarily to increase the focal pressure amplitude required to initiate supra-intrinsic threshold cavitation through the skull. However, it is interesting to observe that even with no aberration phase control, the transcranial main beam focal profile remained very narrow, except below the 3 dB pressure level. With sufficient intensity through the skull, the highly aberrated part of the beam below 3 dB (of the peak) could potentially be “thresholded-out”, producing a clean and small ablative bubble cloud in this supra-intrinsic threshold regime, even without aberration correction.

In addition to improved precision and therapeutic robustness, supra-intrinsic threshold sonication using short pulses could offer other potential advantages, such as the ability to operate at lower central frequencies (< 500 kHz), to minimize acoustic attenuation and aberration effects. The intrinsic threshold cavitation mechanism could maintain ablation accuracy despite an increased focal beam size, and the short pulse sonication regime would virtually eliminate the possibility of standing wave formation in the brain, decreasing the risks of undesirable cavitation events occurring outside the focal region [32-34]. Furthermore, in applications involving large transducer arrays, short pulse sonication is less likely to create grating lobes in comparison to long pulse or continuous wave sonication, [35] and at higher treatment intensities, shorter pulses may reduce the degree of shock scattering from overlying boundaries, decreasing risks of injury from incidental bubbles generated at those interfaces.

The effects of PRF in the histotripsy lesions generated in both the RBC phantoms and liver samples using short, supra-intrinsic threshold pulses appeared to validate previous investigations, which showed that in general, low PRF treatments resulted in better defined lesion profiles and more efficient ablation. In the RBC phantoms treated in this study, as the sonication PRF was increased, higher levels of collateral damage were observed in the form of injury lines created by migrating, single incidental bubbles adjacent to the main lesion. This phenomenon could be explained by the onset of sparse cavitation activity from the initial treatment pulses due to the presence of weak cavitation nuclei within the agarose phantom. Such incidental bubbles can be activated by pressures below the intrinsic cavitation threshold of the medium, and at low PRF settings, these bubbles were collapsed early in the treatment without causing visible damage to the RBC layer. However, at a higher PRF, these incidental bubbles were more likely to persist for several hundred pulses, even lasting through the entirety of the treatment. Incidental bubble translation induced by radiation force at higher PRF was the main cause of the collateral damage observed in the RBC phantoms. While this specific form of collateral damage was not noticeable in the liver lesions, higher PRF treatments in bulk liver tissue correlated with lesions displaying more irregular ablation boundaries and regions of incomplete or partial fractionation at the focal region. These results are in good agreement with a previous study conducted by Wang et al., [36] which has investigated this phenomenon in more detail using a multiple cycle treatment regime. A variety of sonication strategies to minimize the effect of persistent bubbles in the focal zone are currently under research, which could potentially lead to faster and more efficient tissue ablation at higher PRFs.

The bubble cloud initiation region for cavitation bubbles observed for at least 10 pulses or more was observed to be significantly larger than the effective lesion dimensions obtained in the RBC layer. The most likely explanation for this discrepancy is that while the thin RBC layer is able to provide a 2D profile of the ablation extent generated by the therapy, the backlit imaging setup used in this study may have captured incidental cavitation events occurring outside the RBC layer.

In this initial study, a hydrophone was used to perform phase corrections in order to achieve supra-intrinsic threshold focal pressures through the skull. Non-invasive correction methods such as CT or MRI are extensively used in current HIFU systems and could be applied for histotripsy therapy with far less required spatial resolution and sensitivity to patient motion. It may be possible at lower center frequencies to use less complex methods to determine the thickness of the skull, such as ultrasound pulse-echo techniques. These could be applied to restore the focal beam to an amplitude large enough to initiate supra-intrinsic threshold cavitation bubble clouds. Very small, even single bubble clouds would themselves be useful to perform accurate non-invasive focal beam correction through the skull [37, 38]. Finally, if enough focal pressure could be coupled through the skull without significantly distorting the main focal beam that exceeds the intrinsic cavitation threshold, it may even be a possibility to avoid correction mechanisms altogether. Several different transducer fabrication strategies and high power driver systems are under evaluation to increase the acoustic capabilities of therapeutic transducers.

6.5 References

[1] J. G. Lynn and T. J. Putnam, "Histology of Cerebral Lesions Produced by Focused Ultrasound," *Am J Pathol*, vol. 20, pp. 637-49, May 1944.

[2] W. J. Fry, W. H. Mosberg, Jr., J. W. Barnard, and F. J. Fry, "Production of focal destructive lesions in the central nervous system with ultrasound," *J Neurosurg,* vol. 11, pp. 471-8, Sep 1954.

[3] J. W. Barnard, W. J. Fry, F. J. Fry, and J. F. Brennan, "Small localized ultrasonic lesions in the white and gray matter of the cat brain," *AMA Arch Neurol Psychiatry,* vol. 75, pp. 15-35, Jan 1956.

[4] L. Basauri and P. P. Lele, "A simple method for production of trackless focal lesions with focused ultrasound: statistical evaluation of the effects of irradiation on the central nervous system of the cat," *J Physiol,* vol. 160, pp. 513-534 2, Mar 1962.

[5] G. F. Young and P. P. Lele, "Focal Lesions in the Brain of Growing Rabbits Produced by Focused Ultrasound," *Exp Neurol,* vol. 9, pp. 502-11, Jun 1964.

[6] S. I. Tyurina, F. A. Brazovskaya, Y. S. Inin, D. I. Paikin, M. G. Sirotyuk, and L. R. Gavrilov, "Use of focused ultrasound for local destruction of brain structures without damage to the skull," *Bul Exp Biol Med,* vol. 75, pp. 597-598, 1973.

[7] F. J. Fry, "Transkull transmission of an intense focused ultrasonic beam," *Ultrasound Med Biol,* vol. 3, pp. 179-84, 1977.

[8] G. T. Haar and C. Coussios, "High intensity focused ultrasound: past, present and future," *Int J Hyperthermia,* vol. 23, pp. 85-7, Mar 2007.

[9] J. J. Choi, K. Selert, Z. Gao, G. Samiotaki, B. Baseri, and E. E. Konofagou, "Noninvasive and localized blood-brain barrier disruption using focused ultrasound can be achieved at short pulse lengths and low pulse repetition frequencies," *J Cereb Blood Flow Metab,* vol. 31, pp. 725-37, Feb 2011.

[10] C. M. Tempany, N. J. McDannold, K. Hynynen, and F. A. Jolesz, "Focused ultrasound surgery in oncology: overview and principles," *Radiology,* vol. 259, pp. 39-56, Apr 2011.

[11] F. Marquet, M. Pernot, J. F. Aubry, G. Montaldo, L. Marsac, M. Tanter, and M. Fink, "Non-invasive transcranial ultrasound therapy based on a 3D CT scan: protocol validation and in vitro results," *Phys Med Biol,* vol. 54, pp. 2597-613, May 7 2009.

[12] N. McDannold, G. T. Clement, P. Black, F. Jolesz, and K. Hynynen, "Transcranial magnetic resonance imaging- guided focused ultrasound surgery of brain tumors: initial findings in 3 patients," *Neurosurgery,* vol. 66, pp. 323-32; discussion 332, Feb 2010.

[13] K. Hynynen, G. T. Clement, N. McDannold, N. Vykhodtseva, R. King, P. J. White, S. Vitek, and F. A. Jolesz, "500-element ultrasound phased array system

for noninvasive focal surgery of the brain: a preliminary rabbit study with ex vivo human skulls," *Magn Reson Med*, vol. 52, pp. 100-7, Jul 2004.

[14] G. T. Clement, J. Sun, T. Giesecke, and K. Hynynen, "A hemisphere array for non-invasive ultrasound brain therapy and surgery," *Phys Med Biol*, vol. 45, pp. 3707-19, Dec 2000.

[15] M. Pernot, J. F. Aubry, M. Tanter, F. Marquet, G. Montaldo, A. L. Boch, M. Kujas, D. Seilhean, and M. Fink, "High power phased array prototype for clinical high intensity focused ultrasound : applications to transcostal and transcranial therapy," *Conf Proc IEEE Eng Med Biol Soc*, vol. 2007, pp. 234-7, 2007.

[16] M. Pernot, J. F. Aubry, M. Tanter, J. L. Thomas, and M. Fink, "High power transcranial beam steering for ultrasonic brain therapy," *Phys Med Biol*, vol. 48, pp. 2577-89, Aug 21 2003.

[17] M. Pernot, J. F. Aubry, M. Tanter, A. L. Boch, F. Marquet, M. Kujas, D. Seilhean, and M. Fink, "In vivo transcranial brain surgery with an ultrasonic time reversal mirror," *J Neurosurg*, vol. 106, pp. 1061-6, Jun 2007.

[18] C. W. Connor and K. Hynynen, "Patterns of thermal deposition in the skull during transcranial focused ultrasound surgery," *IEEE Trans Biomed Eng*, vol. 51, pp. 1693-706, Oct 2004.

[19] K. Hynynen and F. A. Jolesz, "Demonstration of potential noninvasive ultrasound brain therapy through an intact skull," *Ultrasound Med Biol*, vol. 24, pp. 275-83, Feb 1998.

[20] J. Gateau, J. F. Aubry, D. Chauvet, A. L. Boch, M. Fink, and M. Tanter, "In vivo bubble nucleation probability in sheep brain tissue," *Phys Med Biol*, vol. 56, pp. 7001-15, Nov 21 2011.

[21] Y. Kim, T. Y. Wang, Z. Xu, and C. A. Cain, "Lesion generation through ribs using histotripsy therapy without aberration correction," *IEEE Trans Ultrason Ferroelectr Freq Control*, vol. 58, pp. 2334-43, Nov 2011.

[22] T. L. Hall, K. Kieran, K. Ives, J. B. Fowlkes, C. A. Cain, and W. W. Roberts, "Histotripsy of rabbit renal tissue in vivo: temporal histologic trends," *J Endourol*, vol. 21, pp. 1159-66, Oct 2007.

[23] A. M. Lake, T. L. Hall, K. Kieran, J. B. Fowlkes, C. A. Cain, and W. W. Roberts, "Histotripsy: minimally invasive technology for prostatic tissue ablation in an in vivo canine model," *Urology*, vol. 72, pp. 682-6, Sep 2008.

[24] Z. Xu, G. Owens, D. Gordon, C. Cain, and A. Ludomirsky, "Noninvasive creation of an atrial septal defect by histotripsy in a canine model," *Circulation*, vol. 121, pp. 742-9, Feb 16 2010.

[25] A. P. Duryea, T. L. Hall, A. D. Maxwell, Z. Xu, C. A. Cain, and W. W. Roberts, "Histotripsy erosion of model urinary calculi," *J Endourol,* vol. 25, pp. 341-4, Feb 2011.

[26] A. D. Maxwell, G. Owens, H. S. Gurm, K. Ives, D. D. Myers, Jr., and Z. Xu, "Noninvasive treatment of deep venous thrombosis using pulsed ultrasound cavitation therapy (histotripsy) in a porcine model," *J Vasc Interv Radiol,* vol. 22, pp. 369-77, Mar 2011.

[27] Y. Kim, S. K. Gelehrter, C. G. Fifer, J. C. Lu, G. E. Owens, D. R. Berman, J. Williams, J. E. Wilkinson, K. A. Ives, and Z. Xu, "Non-invasive pulsed cavitational ultrasound for fetal tissue ablation: feasibility study in a fetal sheep model," *Ultrasound Obstet Gynecol,* Nov 12 2010.

[28] A. D. Maxwell, T. Y. Wang, C. A. Cain, J. B. Fowlkes, O. A. Sapozhnikov, M. R. Bailey, and Z. Xu, "Cavitation clouds created by shock scattering from bubbles during histotripsy," *J Acoust Soc Am,* vol. 130, pp. 1888-98, Oct 2011.

[29] A. D. Maxwell, C. A. Cain, T. L. Hall, J. B. Fowlkes, and Z. Xu, "Probability of cavitation for single ultrasound pulses applied to tissues and tissue-mimicking materials," *Ultrasound Med Biol - Accepted for publication,* 2013.

[30] A. D. Maxwell, T. Y. Wang, L. Yuan, A. P. Duryea, Z. Xu, and C. A. Cain, "A tissue phantom for visualization and measurement of ultrasound-induced cavitation damage," *Ultrasound Med Biol,* vol. 36, pp. 2132-43, Dec 2010.

[31] W. W. Roberts, T. L. Hall, K. Ives, J. S. Wolf, Jr., J. B. Fowlkes, and C. A. Cain, "Pulsed cavitational ultrasound: a noninvasive technology for controlled tissue ablation (histotripsy) in the rabbit kidney," *J Urol,* vol. 175, pp. 734-8, Feb 2006.

[32] C. Baron, J. F. Aubry, M. Tanter, S. Meairs, and M. Fink, "Simulation of intracranial acoustic fields in clinical trials of sonothrombolysis," *Ultrasound Med Biol,* vol. 35, pp. 1148-58, Jul 2009.

[33] J. Song, A. Pulkkinen, Y. Huang, and K. Hynynen, "Investigation of standing-wave formation in a human skull for a clinical prototype of a large-aperture, transcranial MR-guided focused ultrasound (MRgFUS) phased array: an experimental and simulation study," *IEEE Trans Biomed Eng,* vol. 59, pp. 435-44, Feb 2012.

[34] M. A. O'Reilly, Y. Huang, and K. Hynynen, "The impact of standing wave effects on transcranial focused ultrasound disruption of the blood-brain barrier in a rat model," *Phys Med Biol,* vol. 55, pp. 5251-67, Sep 21 2010.

[35] B. G. Bardsley and D. A. Christensen, "Beam patterns from pulsed ultrasonic transducers using linear systems theory," *J Acoust Soc Am,* vol. 69, pp. 25-30, 1981.

[36] T. Y. Wang, Z. Xu, T. L. Hall, J. B. Fowlkes, and C. A. Cain, "An efficient treatment strategy for histotripsy by removing cavitation memory," *Ultrasound Med Biol,* vol. 38, pp. 753-66, May 2012.

[37] K. J. Haworth, J. B. Fowlkes, P. L. Carson, and O. D. Kripfgans, "Towards aberration correction of transcranial ultrasound using acoustic droplet vaporization," *Ultrasound Med Biol,* vol. 34, pp. 435-45, Mar 2008.

[38] J. Gateau, L. Marsac, M. Pernot, J. F. Aubry, M. Tanter, and M. Fink, "Transcranial ultrasonic therapy based on time reversal of acoustically induced cavitation bubble signature," *IEEE Trans Biomed Eng,* vol. 57, pp. 134-44, Jan 2010.

Chapter 7

Conclusions and Future Work

This work has explored the therapeutic impact of acoustic aberration effects in the context of non-invasive histotripsy therapy for transcostal, transabdominal and transcranial treatment scenarios. The purpose of this chapter is to summarize the key points and findings from each of the studies presented in this work, as well as discuss the challenges and potential improvements that could be made in order increase the effectiveness of the therapy for each application. Recommendations for future studies are given in hopes that further research may be facilitated by building upon the studies presented herein.

7.1 Transcostal Histotripsy Therapy

In the transcostal histotripsy treatments discussed in this work, “traditional”, shock scattering histotripsy therapy using highly non-linear multi-cycle sonication pulses (5 cycles) was observed to have a significant level of immunity against elevated grating lobes. Despite the presence of elevated peak rarefactional grating lobes, exceeding 50%

of the amplitude of the main focal beam, confined lesions could be generated at the focus of each treatment through both rib phantoms and excised porcine ribs.

In addition to the lower peak rarefactional pressures at the grating lobes, it is interesting to note that relative peak compressional values at the locations of the grating lobes may be even more substantially decreased because of the narrow focusing region in which shockwaves tend to develop (Figure 7.1). Because the expansion of bubble clouds in the shock scattering initiation regime is dependent on the presence of high peak compressional shock waves [1], if the shock front is weakened, this process cannot occur reliably. This characteristic could potentially provide an increased safety margin against collateral damage induced by grating lobes during sonication.

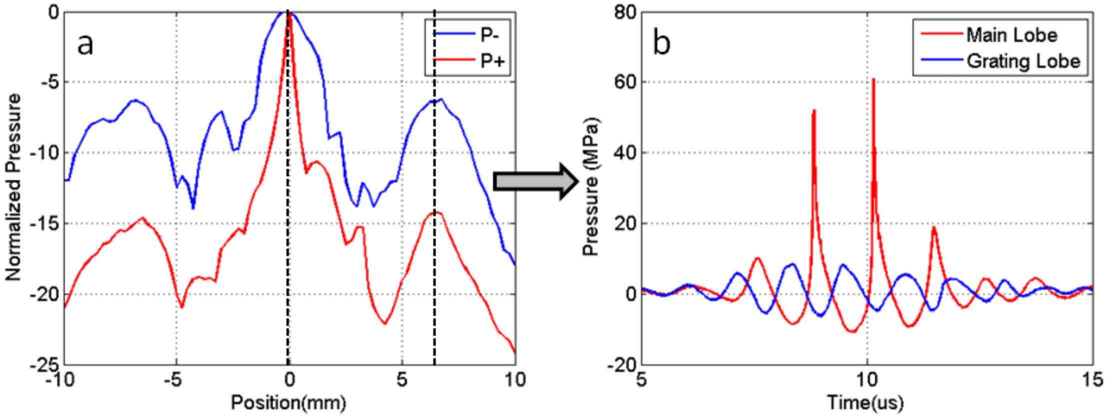

Figure 7.1. (a) Normalized peak rarefactional (P-) and compressional (P+) focal pressure distribution of a 750 kHz transducer when a rib aberrator is placed in the field. (b) Pressure waveforms measured at the main lobe and at the grating lobe locations as indicated by the dashed lines in panel (a).

The therapeutic robustness of histotripsy therapy was validated in non-invasive experiments performed in live pigs without aberration correction. By carefully modulating the input acoustic pressure at the focus through real-time feedback imaging, comparable lesions could be obtained through acoustic windows with and without rib obstruction. Furthermore, the low duty cycle of histotripsy therapy have been shown to minimize the likelihood of inducing potentially hazardous thermal effects on overlying tissues, which is a significant advantage when highly absorptive structures such as rib bones are present in the acoustic field.

One of the potential challenges in performing transcostal histotripsy therapy could be the high levels of pressure attenuation due to the presence of the ribcage. Depending on the extent of rib coverage, acoustic pressure signal losses of over 50% could be incurred because of the ribs, even without considering the attenuation of overlying tissues, such as skin or muscle. Recommendations for future studies would be to improve upon the current therapeutic setup by using high power density transducers which could allow greater pressure to be delivered to the therapy focus. In addition, the use of custom-designed transducer arrays would enable the implementation of electronic beam steering, providing a substantial decrease in treatment times over mechanical focal steering, especially in the ablation of larger lesion volumes.

An additional potential improvement for future studies would be the use pulse regimes using the intrinsic cavitation initiation mechanism [2], which could further reduce the likelihood of inducing thermal effects in overlying tissues. This short pulse sonication strategy would also decrease the probability of inducing shock scattering effects at overlying tissue/bone interfaces, thereby reducing the chance of causing unintended damage at those boundaries. In addition, short pulses may also minimize the amplitude of grating lobe effects arising from the periodic spatial distribution of the acoustic sources [3], which could increase the therapeutic immunity of histotripsy therapy even further. This effect is further discussed in Appendix A.

7.2 Non-invasive Fetal Therapy

Fetal surgery is still a relatively novel concept, with the first general guidelines for fetal intervention established in the early 1980s. Despite significant improvements in fetal/maternal medicine, fetal surgery is still not advisable as a routine procedure to patients due to the level of complexity and potential risks involved in such operations [4, 5]. A non-invasive procedure such as transabdominal fetal histotripsy could potentially eliminate many of the risks associated with currently available invasive and minimally-invasive intervention methods, which was a major motivation for the studies presented in this work.

The initial studies on the feasibility and long-term gestational safety of non-invasive fetal histotripsy therapy have been promising, suggesting that histotripsy therapy may have potential as a treatment option for certain fetal intervention procedures, such as the ablation of abnormal masses, including fetal tumors. From the safety studies explored herein, all lambs which underwent fetal liver and kidney ablation procedures survived and were delivered normally. In addition, histotripsy therapy appeared to cause no significant pregnancy complications in the maternal ewes.

Technical improvements such as the use of more powerful custom-designed transducer arrays capable of electronic focal steering could significantly benefit fetal histotripsy therapy, helping it achieve higher treatment precision and efficiency. The implementation of new sonication strategies, such as short pulse histotripsy therapy could further enhance the precision of the treatment and increase its versatility and robustness against acoustic aberration effects. In addition, shorter sonication pulses would minimize prefocal cavitation events that were occasionally observed to cause petechial hemorrhage on the skin of the fetuses.

Longer term studies evaluating the well-being of treated animals post-partum should also be conducted in order to better assess the full impact of this therapy in both the mother and the fetus. Studies involving a more suitable animal model with fewer anatomical particularities would be beneficial in the refinement of this technique towards clinical application. *In vivo* MR imaging for the detection of potential emboli generated from histotripsy therapy and cognitive/behavioral evaluation of the neonates could also be explored in future studies to better assess any potential long-term side effects arising from the application of this therapy.

7.3 Transcranial Histotripsy Therapy

The feasibility study presented herein demonstrated that short-pulse, supra-intrinsic threshold histotripsy could be applied transcranially to successfully generate lesion sizes significantly below the estimated focal zone dimensions of the therapy transducer. It was necessary to perform aberration correction with a hydrophone, primarily in order to enable the focal main beam to reach sufficient pressure levels for the initiation of cavitation bubble clouds. Future studies may integrate non-invasive imaging modalities such as MRI and ultrasound for aberration correction procedures as necessary. However, histotripsy therapy may not require high spatial resolution algorithms, and coarse aberration correction techniques could be enough to allow histotripsy therapy to achieve sufficient therapeutic precision.

Lower frequency transducers (< 300 kHz) would bring interesting possibilities for further studies, since both attenuation and aberration effects from the skull would be less significant at lower operational frequencies [6]. The challenge in implementation would be to overcome the reduced surface pressure outputs and focusing gains provided by lower frequency PZT elements. Denser element packing ratios could help increase the acoustic gain with low frequency arrays, and further technical improvements in piezoelectric materials, transducer assembly techniques, matching layer design and driving electronics could potentially enable the fabrication of low frequency, high power density elements suitable for transcranial applications.

Another possibility would be the incorporation of small, high frequency transducers through small bone windows in the skull to complement the pressure provided by a larger, extracranial low frequency array. This treatment method would be invasive, but because of the smaller pressure requirements necessary for the high frequency transducer, the invasive transducer could be designed to have a very small footprint, which would minimize the surgical burden of creating an adequate acoustic window. With proper transducer alignment and timing implementation, high frequency pulses could be modulated in such a way to constructively interfere with the low frequency "baseband" pressure in precise spatiotemporal locations, further increasing treatment precision. This pressure "pump" strategy could also have uses in a number of other treatment applications in which therapeutic windows may be limited and/or additional precision is desired.

Transcranial histotripsy therapy research is still in its incipient stages, and as discussed above, a number of improvements could be implemented in future studies in order to augment the therapeutic capabilities of this technique. In addition to refinements in treatment delivery methods, it is also important that bioeffect studies be conducted to evaluate the impact of this therapeutic modality to the brain *in vivo*. Because of the fragile and complex nature of the brain as an organ, acute and chronic issues such as the potential for inducing hemorrhagic and embolic events, as well as long term treatment effects of the therapy will need to be carefully assessed. Transcranial histotripsy studies in small animal models *in vivo* could perhaps be the next research step in this direction. The integration of MRI monitoring of treatment procedures would be beneficial in such studies, and research efforts with the goal of enabling MRI guided histotripsy therapy are currently underway.

While it is still early to determine whether cavitation therapy could be clinically recommended for the treatment of specific brain conditions, initial *in vitro* results are encouraging, and show that short-pulse histotripsy therapy is capable of generating small, fully contained lesions transcranially using a low frequency transducer. This high precision ablation capability, in addition to the immunity of the therapy to heat sink effects and the minimal thermal impact on the skull interface could greatly offset several of the major limitations faced by currently available thermal ablation techniques, bringing significant potential benefits for transcranial therapy applications.

7.4 Conclusions

The pressure threshold mechanism governing the cavitation bubble cloud initiation process in histotripsy therapy grants it considerable therapeutic immunity against acoustic aberration effects, allowing precisely controlled ablation to be achieved by careful pressure modulation near the bubble cloud initiation threshold. Refinements in the understanding of the cavitation initiation mechanism in various media and the development of application-specific transducers and sonication strategies will be beneficial in further improving the controllability and predictability of histotripsy ablation in a variety of non-invasive therapeutic scenarios.

7.5 References

[1] A. D. Maxwell, T. Y. Wang, C. A. Cain, J. B. Fowlkes, O. A. Sapozhnikov, M. R. Bailey, and Z. Xu, "Cavitation clouds created by shock scattering from bubbles during histotripsy," *J Acoust Soc Am,* vol. 130, pp. 1888-98, Oct 2011.

[2] A. D. Maxwell, C. A. Cain, T. L. Hall, J. B. Fowlkes, and Z. Xu, "Probability of cavitation for single ultrasound pulses applied to tissues and tissue-mimicking materials," *Ultrasound Med Biol,* vol. 39, pp. 449-65, Mar 2013.

[3] B. G. Bardsley and D. A. Christensen, "Beam patterns from pulsed ultrasonic transducers using linear systems theory," *J Acoust Soc Am,* vol. 69, pp. 25-30, 1981.

[4] F. I. Luks, "New and/or improved aspects of fetal surgery," *Prenat Diagn,* vol. 31, pp. 252-258, 2011.

[5] S. M. Kunisaki and R. W. Jennings, "Fetal surgery," *J Intensive Care Med,* vol. 23, pp. 33-51, Jan-Feb 2008.

[6] K. Hynynen and F. A. Jolesz, "Demonstration of potential noninvasive ultrasound brain therapy through an intact skull," *Ultrasound Med Biol,* vol. 24, pp. 275-83, Feb 1998.

APPENDICES

Appendix A

Effects of Periodic Acoustic Obstruction in Focused Transducers

This appendix discusses the impact of periodic aperture obstruction in the acoustic pressure profiles of focused transducers as relevant in transcostal therapy scenarios. A transient simulation model is used to evaluate aberration patterns caused by different degrees of aperture obstruction, and the effects of temporally narrow excitation pulses in the focal grating lobe response are examined.

A.1 Time-Harmonic Modeling

As explored in Chapter 2, transcostal acoustic windows can introduce grating lobes in the focusing profile of the therapy transducer because of the periodic obstruction patterns created by the ribcage. Due to the highly reflective and attenuative nature of the rib bones, virtually all of the ultrasound energy significantly contributing to the focal main beam is transmitted through the intercostal spaces between the ribs [1], causing the effective radiating aperture to behave as an array with sources separated by the width of the rib bones.

Correction mechanisms such as time-reversal or phase conjugation methods may be able to improve the focal the profile to an extent by providing an ideal matched filter correction to phase and amplitude distortions present in the field [1, 2]. However, because such algorithms also naturally reduce the acoustic power incident on the ribs, the corrected aperture will still perform as if it were periodically obstructed, making the presence of grating lobes unavoidable due to the arraying effect of the ribs.

A previous study by Khokhlova et al. provides a thorough theoretical analysis on the mechanism behind the formation of grating lobes (referenced in their study as “focal splitting”) in the context of focused radiators operating in continuous wave (CW) mode [3]. An analytical expression describing the aberrated acoustic intensity profile caused by periodic rib obstruction was derived, which is modified herein for normalized pressure:

$$P_{norm}(0, y, F) =$$

$$\left(\frac{kaR^2}{h(F-z)}\right) \times \left| \sum_{m=-\infty}^{\infty} sinc\left(\frac{\pi ma}{h}\right) e^{-i\frac{2\pi md}{h}} \times \frac{J_1\left(R\sqrt{\left(\frac{ky}{F-z} - 2\pi\frac{m}{h}\right)^2}\right)}{R\sqrt{\left(\frac{ky}{F-z} - 2\pi\frac{m}{h}\right)^2}} \right| \qquad \text{A.1}$$

Where $k = 2\pi/\lambda$ is the wavenumber, F is the focal length of the transducer, R is the effective acoustic aperture radius intersecting the ribs, z is the axial distance of the ribs from the origin of the transducer, $h = a + b$ (where a is the intercostal gap and b is the width of the rib bone), d is the distance between the transducer axis to the middle of a intercostal space and $J_1$is a Bessel function of the first kind.

This expression gives the 1D pressure profile distribution across the axis (y) perpendicular to the orientation of the obstructions (i.e., cross-sectioning the ribs). A paraxial approximation is used (weak focusing), and the source is assumed to be a uniform piston radiator periodically obstructed by ideal absorbers. Figure A.1 shows the focal profile given by this analytical expression when a 750 kHz focused radiator with 15 cm diameter and 12 cm focal length is used with the following parameters: $a = 1.3$ cm, $b = 1.4$ cm, $d = 0$ cm, and $z = 4$ cm. These parameters are similar to the experimental setup used in Chapter 2 with the rib phantom positioned at 8 cm from the focus of the transducer, and are comparable to the distribution of ribs and intercostal spaces found in the human ribcage [4].

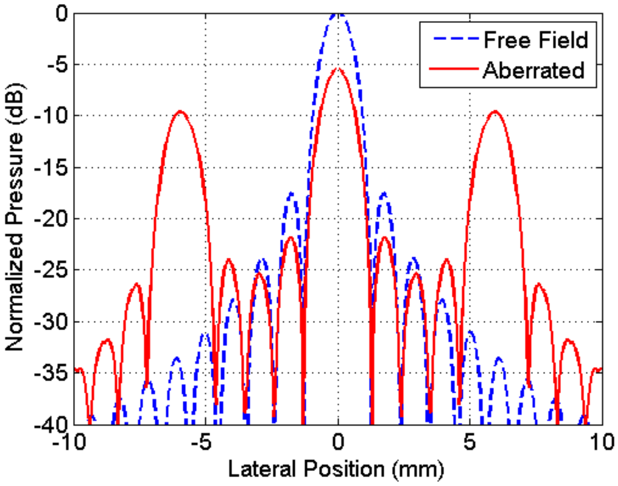

Figure A.1. CW focal pressure distributions analytically calculated for a 750 kHz focused radiator under free field (unobstructed) and aberrated (periodically obstructed) conditions. Plots are normalized with respect to free field.

From the analytically calculated profiles, the aberrated main beam was reduced to approximately -6 dB in comparison to the main beam amplitude obtained without any obstructions (free-field). The relative full width at half maximum (FWHM) of the main beams remained the same, at 2 mm for both cases. In the periodically obstructed field, grating lobes of -4 dB relative to the aberrated main beam were introduced, which were slightly higher than the grating lobe amplitudes measured under similar conditions with the rib phantom as reported in Chapter 2 (approximately -6 dB). Discrepancies between these results were expected since the analytical expression assumes CW sonication and the transducer aperture (containing a center gap) could not be exactly reproduced using the analytical method.

A.2 Transient Acoustic Simulations

While time-harmonic models may be adequate to describe acoustic fields generated by longer pulses, transient simulations can provide a better representation of fields generated by temporally narrow pulses such as those used in histotripsy therapy. In addition, more unique or complex aperture geometries may be defined through direct simulations, allowing radiating sources to be more accurately modeled. Transient acoustic fields were calculated using a simulation package (Fast Object-oriented C++ Ultrasound Simulator - FOCUS) developed by McGough et al., which enables large field calculations to be resolved efficiently through spatiotemporal decomposition techniques [5, 6].

A transducer geometry similar to that used in the study presented in Chapter 2 (750 kHz, 15 cm diameter, 12 cm focal length, 5.9 cm center gap) was modeled as an ultrasound source (Figure A.2a). The aperture consisted of approximately 2000 individual point sources distributed in a spherically focused shell. Periodic obstruction patterns were implemented by applying a binary acoustic mask to the source aperture, which deactivated elements that were directly located under the “blocked” portions of the mask. Each blocking region corresponding to a rib had a width of 1.3 cm and was separated by 1.4 cm (intercostal space). While this approach does not account for diffraction effects arising from the placement of obstructions in the middle of the propagating field, these simulations should still provide a reasonable approximation of the aberration effects caused by obstacles placed close to the transducer aperture. Transient excitation pulses consisting of 5 cycles with a normalized source (particle) velocity of 1 m/s were used in all plots unless stated otherwise (Figure A.2b).

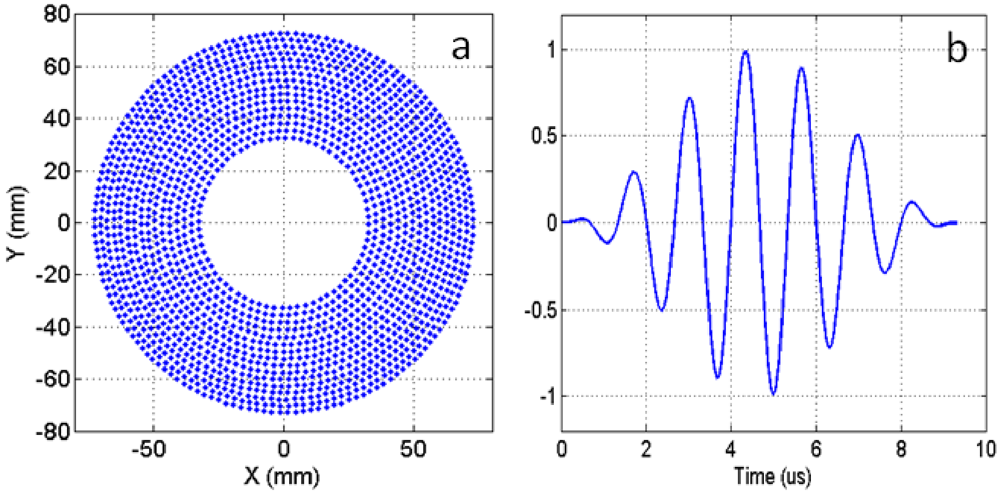

Figure A.2. Unobstructed 750 kHz focused source radiator containing approximately 2000 discrete point sources (a). Five cycle source excitation pulse applied for transient simulations (b).

A.2.1 Partial Aperture Obstruction Effects

Figure A.3 shows aberrated focal profiles generated when the aperture was periodically obstructed by various degrees. The profiles trace the maximum linear pressure amplitude obtained at each spatial point. As expected, the aberrated main beam amplitudes were observed to decrease as a greater portion of the source aperture was masked, but the FWHM of the main beams in all cases remained the same at approximately 2 mm.

With full periodic obstruction of the aperture, the main beam was reduced to approximately -6 dB with respect to unobstructed conditions (free field), and grating lobes of approximately -7 dB relative to the aberrated main beam amplitude were generated in the profile. These values are comparable to directly measured results reported in Chapter 2 when the rib obstacles were positioned close to the transducer aperture, which generated grating lobe amplitudes of -6 to -7 dB with respect to the main beam.

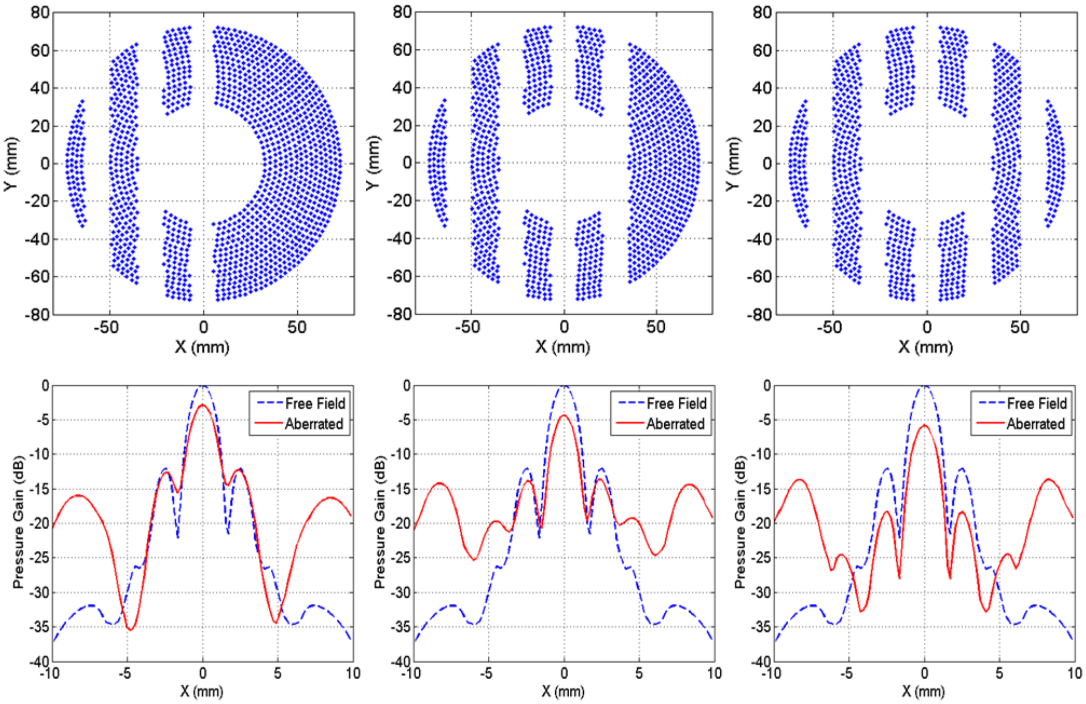

Figure A.3. Transversal focal profiles generated when different portions of the frontal transducer aperture were periodically obstructed. Reduced main beam amplitudes and higher grating lobe levels were observed by masking a greater portion of the aperture. All plots are normalized with respect to free field (unobstructed) conditions.

As a lesser portion of the transducer aperture was obstructed, the relative grating lobe response in the focal profile decreased from -7 dB with full aperture coverage to –13 dB with approximately 50% of coverage. This phenomenon may be explained by array theory, which states that grating lobes are maximized when radiating sources are distributed in spatially regular patterns. Decreased periodicity of the source aperture would therefore be a likely factor in reducing the relative amplitude of grating lobes generated in the focal region. It is interesting to note, however, that while the grating lobe response was decreased, the relative sidelobe amplitudes near the main beam appeared to increase from approximately -13 dB with full aperture coverage, to -9 dB with 50% coverage.

A.2.2 Short Pulse Diffraction Effects

To investigate the effects of using shorter pulse length excitations in the grating lobe response and the overall focusing profile of the transducer, additional transient simulations were performed using pulses consisting of 1, 2 and 3 cycles under full periodic obstruction conditions. Figure A.4 shows the resulting pressure profiles generated by each excitation mode. Whereas the main beam was similarly attenuated in all cases to approximately -6 dB with respect to unobstructed conditions, shorter excitation pulses caused the relative grating lobe response to progressively decrease. Maximum grating lobe amplitudes of -10, -13 and -15 dB with respect to the aberrated main beam were generated with pulse lengths of 3, 2 and 1 cycles, respectively.

This phenomenon has been described in more detail by Bardsley and Christensen [7], who have shown that for point-source linear arrays, pulses shorter than approximately $T = 1.14NT_0$ (where N is the number of active elements in the array and T_0 is the fundamental period of the frequency) yielded reduced grating lobe amplitudes in comparison to CW excitation because of the decreased level of constructive interference occurring outside of the center axis of the array. Using a similar point-source assumption for simplification purposes, this equivalent pulse length *T* for the case modeled herein would correspond to approximately 9 μs — or less than 7 full cycles at 750 kHz — suggesting that excitation pulses shorter than this value would be beneficial in reducing the grating lobe response in the focal profile, as indeed appears to be the case.

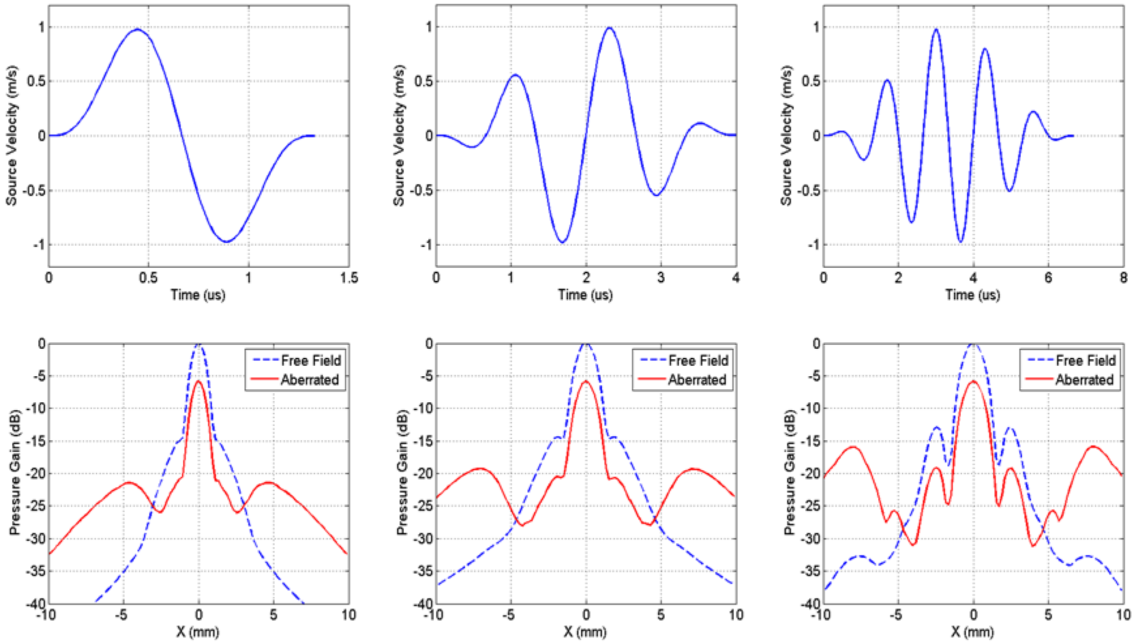

Figure A.4. Focal profiles generated under full periodic obstruction using pulse lengths of 1, 2 and 3 cycles. Grating lobes were progressively suppressed in profiles generated with shorter pulses. Spatial narrowing of the main beam was observed in the focusing profile generated with a single cycle pulse. All plots are normalized with respect to unobstructed (free field) conditions.

Another interesting effect observed was the noticeable spatial narrowing of the main beam in profiles generated by very short excitation pulses (< 3 cycles). The FWHM of the main beam under CW conditions was approximately 2 mm, which was similar in profiles generated with 3 and 5 cycles, but was decreased to as low as 1.3 mm in the profile generated by a single cycle pulse, illustrating the greater relevance of wideband diffraction effects over steady-state assumptions in transient acoustic fields generated by temporally narrow ultrasound pulses [8].

These results suggest that using shorter sonication pulses could be an effective strategy to reduce the impact of grating lobes caused by periodic aperture obstruction while potentially providing higher therapeutic precision in the form of a narrower focal main beam if sufficiently short pulses can be applied. Lower frequency transducers may particularly benefit from this effect, enabling their use in a wider range of high precision therapy applications.

A.3 References

[1] J. F. Aubry, M. Pernot, F. Marquet, M. Tanter, and M. Fink, "Transcostal high-intensity-focused ultrasound: ex vivo adaptive focusing feasibility study," *Phys Med Biol,* vol. 53, pp. 2937-51, Jun 7 2008.

[2] J. R. Ballard, A. J. Casper, Y. Wan, and E. S. Ebbini, "Adaptive transthoracic refocusing of dual-mode ultrasound arrays," *IEEE Trans Biomed Eng,* vol. 57, pp. 93-102, Jan 2010.

[3] V. Khokhlova, S. Bobkova, and L. Gavrilov, "Focus splitting associated with propagation of focused ultrasound through the rib cage," *Acoustical Physics,* vol. 56, pp. 665-674, 2010.

[4] S. J. Cala, C. M. Kenyon, A. Lee, K. Watkin, P. T. Macklem, and D. F. Rochester, "Respiratory ultrasonography of human parasternal intercostal muscle in vivo," *Ultrasound Med Biol,* vol. 24, pp. 313-26, Mar 1998.

[5] J. F. Kelly and R. J. McGough, "A time-space decomposition method for calculating the nearfield pressure generated by a pulsed circular piston," *IEEE Trans Ultrason Ferroelectr Freq Control,* vol. 53, pp. 1150-1159, 2006.

[6] D. Chen and R. J. McGough, "A 2D fast near-field method for calculating near-field pressures generated by apodized rectangular pistons.," *J. Acoust. Soc. Am.,* vol. 124, pp. 1526-1537, 2008.

[7] B. G. Bardsley and D. A. Christensen, "Beam patterns from pulsed ultrasonic transducers using linear systems theory," *J Acoust Soc Am*, vol. 69, pp. 25-30, 1981.

[8] F. S. Foster and J. W. Hunt, "The design and characterization of short pulse ultrasound transducers," *Ultrasonics*, vol. 16, pp. 116-122, 1978.

Appendix B

Piezoelectric Driving Systems for Histotripsy Therapy

High intensity ultrasound transducers for thermal ablation therapy are typically driven with linear radiofrequency (RF) power amplifiers, such as class A or B designs, terminated with a standard output impedance of 50 ohms. Linear amplifiers operate as voltage controlled current sources, and are capable of providing high fidelity signal amplification. However, because the output power transistors in linear designs operate in a continuous mid-conduction state, i.e., always "on", linear amplifiers are inherently limited in terms of power efficiency, generating large amounts of waste heat during operation. High power linear amplifiers typically require large cooling apparatuses for efficient operation, which considerably increase the physical size of the device and the logistical difficulty of driving large transducer arrays containing hundreds of elements.

As discussed in previous chapters, the initiation of histotripsy cavitation bubble clouds may be successfully achieved at arbitrarily low duty cycles, as long that enough rarefactional pressure is available at the focus. As such, the ability of delivering high instantaneous peak voltages directly to the transducer elements becomes a more relevant and critical parameter for histotripsy drivers than its average power handling capabilities.

This is in contrast to RF amplifiers used in thermal ablation therapy, which report total power transfer capabilities as a primary figure of merit.

The high-amplitude, low duty cycle sonication requirements of histotripsy therapy have led to the development of compact, custom electronic driving circuits specifically designed for histotripsy transducers, focusing on achieving the high voltage levels needed to obtain maximum instantaneous pressure outputs from piezoelectric elements. This section presents an overview of these designs, providing a discussion of their advantages and limitations in the context of histotripsy therapy.

B.1 Complementary Push-Pull Amplifier

Switching amplifier designs, such as the class-D amplifier are very power efficient because in contrast to the always-on transistor state required for linear behavior, switching circuits operate the transistor in either full-on or full-off mode. This allows a theoretical efficiency of 100% if ideal switching can be achieved [1]. High voltage push-pull switching drivers based on class-D amplifier designs have been previously developed and optimized for histotripsy applications by Hall and Cain [2], who have demonstrated the use of custom, compact, high density amplifier boards to drive a transducer array with 512 elements.

Push-pull switching drivers can output a single pole square wave with amplitude proportional to the reference DC high voltage source. In the complementary design approach, two types of transistors, a P-channel and an N-channel are responsible for the switching of the high side and low side of the circuit, respectively. At any single time, only one of the sides is open, connecting either the high voltage (HV) or ground (GND) reference to the output of the driver (Figure B.1). The complementary action of P-type MOSFETS on the high side of the circuit brings simplification for push-pull switching designs primarily because P-type transistors used on the high side transistor do not require a floating voltage source in order to drive the transistor's gate (G_P), since the source (S_P) of the transistor is tied to the reference high voltage supply.

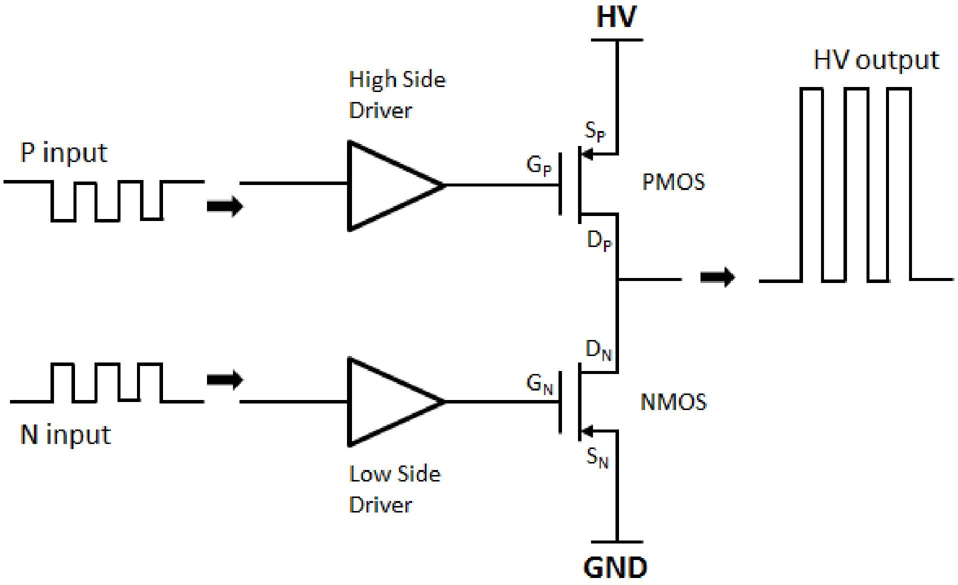

Figure B.1. Basic circuit diagram of a push-pull complementary amplifier design using P-type and N-type transistors for high voltage pulse generation.

PZT transducers present an inherently challenging load for high voltage drivers because of their complex (not purely resistive) impedances. In order to drive a PZT transducer with a square wave push-pull amplifier, an electrical "matching" network is typically used in order to reduce the impedance of the transducer, and remove the complex (inductive or capacitive) part of the impedance at the resonant center frequency of the transducer. Simple L-section networks have been extensively used with histotripsy transducers, providing impedance reduction and low-pass filtering of the higher harmonics of square wave (Figure B.2). In addition, the use of matching networks can provide a significant increase in the peak-to-peak voltage transmitted to the transducer, allowing higher surface pressures to be achieved at a given DC voltage applied to the push-pull driver, as shown in Figure B.3. All measurements presented herein were conducted using a 500 kHz, element module, consisting of a 50.8 mm diameter PZT-8 disc bonded to an acoustic lens through a quarter wavelength matching layer. The particular element used for these tests had an initial impedance of approximately 110 Ω (magnitude). Further details about the construction of this element module and its electroacoustic characteristics may be found in Appendix C.

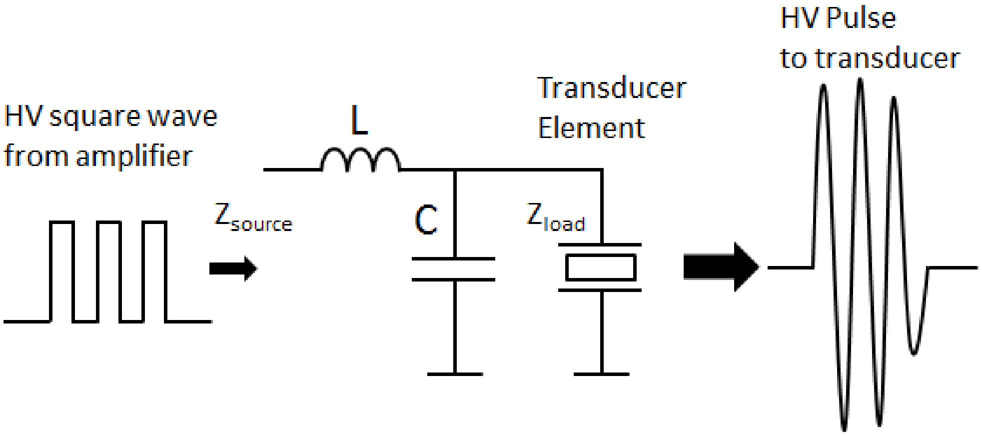

Figure B.2. Standard L-section matching network design used in conjunction with class-D amplifiers to drive histotripsy transducers. Higher voltage gains may be achieved by selecting capacitor (C) and inductor (L) values to reduce the initial transducer impedance (Z_{load}) to a lower impedance (Z_{source}).

The L-section matching network is one of the simplest methods to transform the electrical impedance of complex loads, only requiring a parallel capacitor (C) and a series inductor (L). From the knowledge of the transducer impedance Z_{load}, the source impedance value as seen by the output of the amplifier may be obtained by the formula:

$$Z_{source} = j\omega L + \frac{Z_{load} \times \frac{1}{j\omega C}}{Z_{load} + \frac{1}{j\omega C}} \qquad \text{B.1}$$

Where $\omega = 2\pi f$. One of the limitations of this design is that it does not allow broadband impedance transformation, restricting optimal results to a relatively narrow band centered on the resonant frequency f of the transducer. With L-section designs, higher voltage gains may be achieved with more aggressive impedance transformation ratios, i.e., further reducing the impedance of the transducer as seen by the driver output.

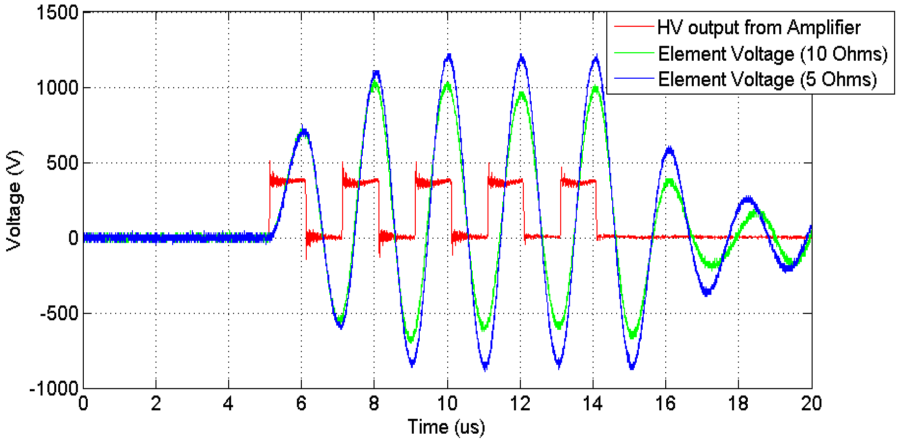

Figure B.3. Voltage excitation waveforms obtained with a class-D push-pull amplifier driving a 500 kHz, acoustically matched PZT-8 module under two L-section impedance configurations at 10 Ω (green) and 5 Ω (blue). A 5 cycle, 400V peak voltage square wave output from the class-D amplifier is shown as a reference (red).

A detailed numerical analysis for the voltage gain expected of PZT transducers using first order LC networks has been provided by Maxwell [3]. A low impedance transformation approach is limited by the higher transistor current handling capabilities necessary to properly sustain very low impedance loads (Figure B.4). This may require the reduction of the effective output impedance of the amplifier, which may be achieved by using larger transistors with lower on-state resistance, or by using several transistors connected in parallel at the output stage of the amplifier.

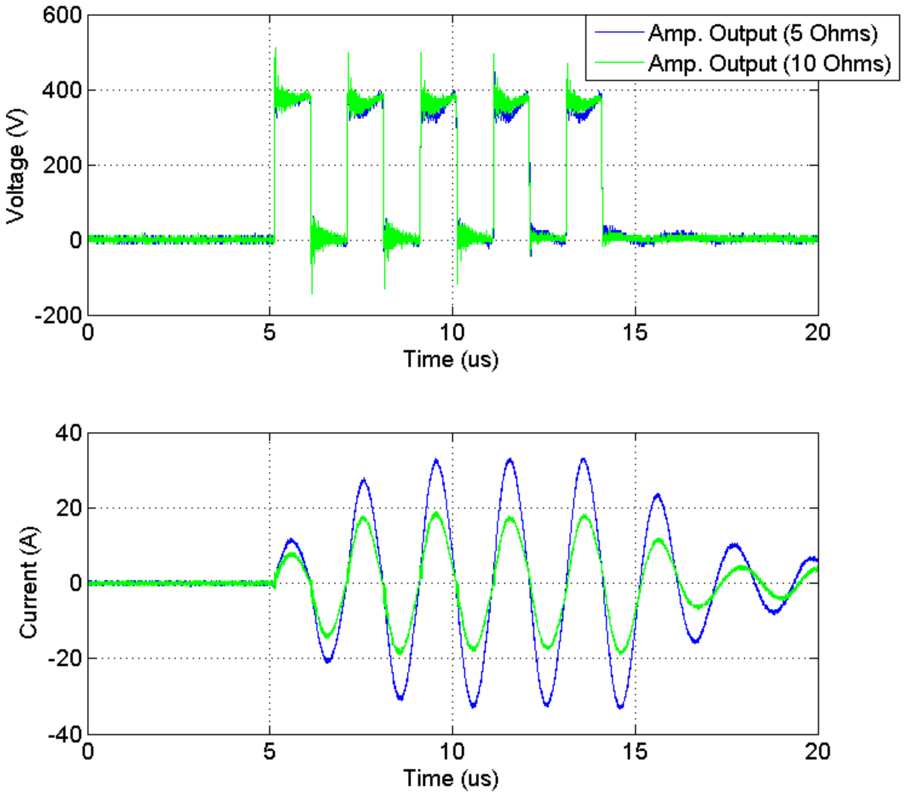

Figure B.4. Voltage and current measurements at the output of the class-D amplifier driving the PZT-8 module matched at 10 Ω (green) and 5 Ω (blue). More aggressive impedance transformation ratios require increased current handling capacities from the transistors for effective operation.

B.2 Stacked Transistor Push-Pull Designs

While providing circuit simplification benefits, one of the shortcomings of the complementary switching design is that the maximum voltage handling capacity of the circuit is restricted by the availability of high voltage/high frequency P-channel transistors used in the high side of the circuit connected to the high voltage (HV) reference. N-channel transistors are typically superior than their P-channel counterparts in switching times, power handling capabilities and conduction resistivity. This is in part due to the fundamental physical difference governing the basic operation of N-channel and P-channel transistors. The inherently lower mobility of holes (used as charge carriers in P-type MOSFETs) in comparison to electrons (used as carriers in N-types) significantly increases the channel resistance of the P transistor, adversely affecting its overall performance [4]. Because of this, P-channel transistors are rarely used in high power applications that do not require complementary switching.

In order to allow class-D driver designs to achieve higher pulse voltages, a potential solution would be to use a design based on all N-channel components, which can offer better high power switching performance. However, because the source of the high side transistor is connected to the output of the driver, the transistor gate needs to be activated by a driver with a floating voltage reference (according to the voltage reference measured at the transistor’s source). Such floating gate driver circuits have been previously implemented through bootstrap capacitor configurations [5] or by isolated DC-DC voltage converters [6].

Despite the additional components necessary for implementation, floating gate driving configurations enable transistors to be driven without the necessity of a fixed reference voltage (such as GND or HV) for the source terminal. This can be especially useful in the assembly of “stacked” transistor designs [7, 8] which can increase the maximum voltage capacity of the amplifier even further (Figure B.5). The transistor stacking method effectively allows the maximum voltage limit of the circuit to be arbitrarily increased by incorporating additional transistors in the high and low sides of the amplifier, at the cost of higher complexity.

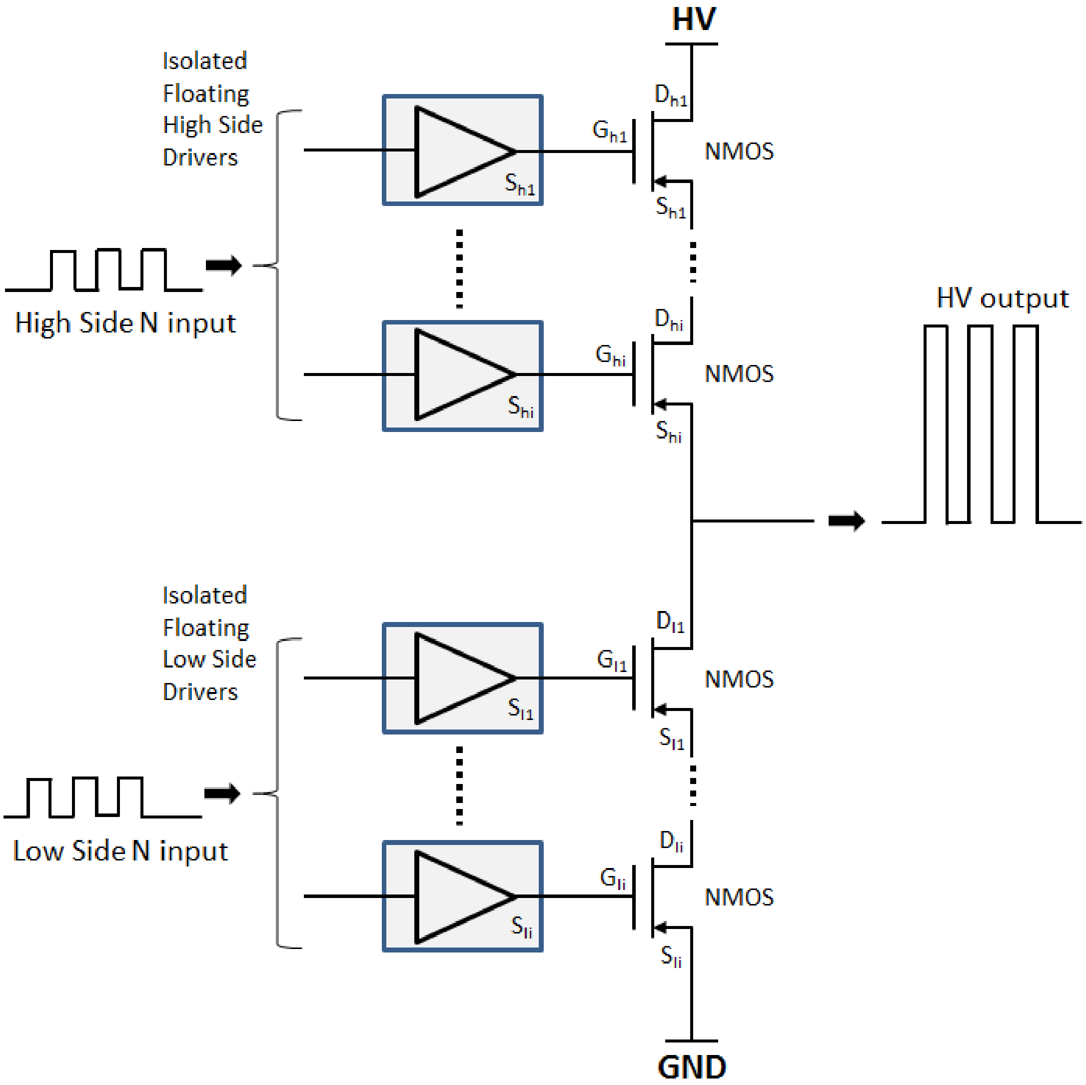

Figure B.5. Stacked push-pull amplifier schematic using single channel (N-type) transistors with floating reference gate drivers.

While stacked transistor configurations may not be a cost-effective option to drive larger arrays consisting of several hundred elements, such an implementation would be useful for transducers designs using fewer, but larger or lower frequency active elements that require higher peak to peak driving voltages to achieve sufficiently high acoustic pressures for histotripsy therapy applications.

B.3 Inductor Current Driver

The inductor current driver design has been one of the most recent developments in high voltage piezoelectric pulsers for histotripsy transducers. The operating mechanism of this driver involves the cyclical charge and discharge of an inductor across a transducer connected in parallel (Figure B.6) A single, high voltage transistor is used as a switch, allowing current to flow through the inductor (L) during its on-cycle. Charging pulse lengths (typically < 10 μs) are dictated by the total period the transistor remains turned on, during which the inductor experiences a linear increase in the current flow i, which increases the voltage across its terminals by the familiar formula $V(t) = L\frac{di}{dt}$. At the end of the charging period, the transistor is turned off, suddenly interrupting the flow of current and forming a circuit consisting of the charged inductor and the transducer load. This excitation method is somewhat similar to delivering an electrical impulse from the charged inductor to a parallel resonant circuit containing a piezoelectric transducer, allowing very short, high amplitude acoustic pulses to be achieved. Figure B.7 shows representative voltage and current pulses measured across the same matched PZT-8 module used in previous tests.

Under this driving regime, the total length of the pulse cannot be easily adjusted as in the case of push-pull switching approaches because of the inductor charging times required prior to firing each pulse and the lack of a grounding cycle to quickly discharge the transducer after the excitation peak is reached. As such, this driving method generates very short pulses (< 2 full cycles) which may not be suitable for narrow bandwidth transducers that require several oscillation cycles in order to “ring-up” to full resonance amplitude. Therefore, piezoelectric elements driven using this approach should be acoustically well-matched, providing the additional bandwidth necessary to increase compatibility with short pulse (or broadband) operation.

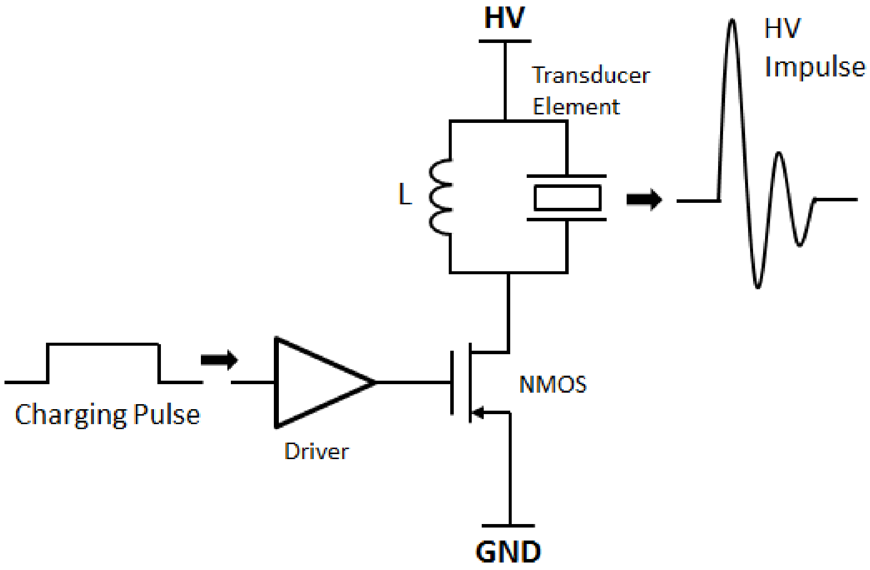

Figure B.6. Simplified schematic of the current charge driver design. The high voltage impulse is delivered to the transducer at the active low edge of the input charging pulse.

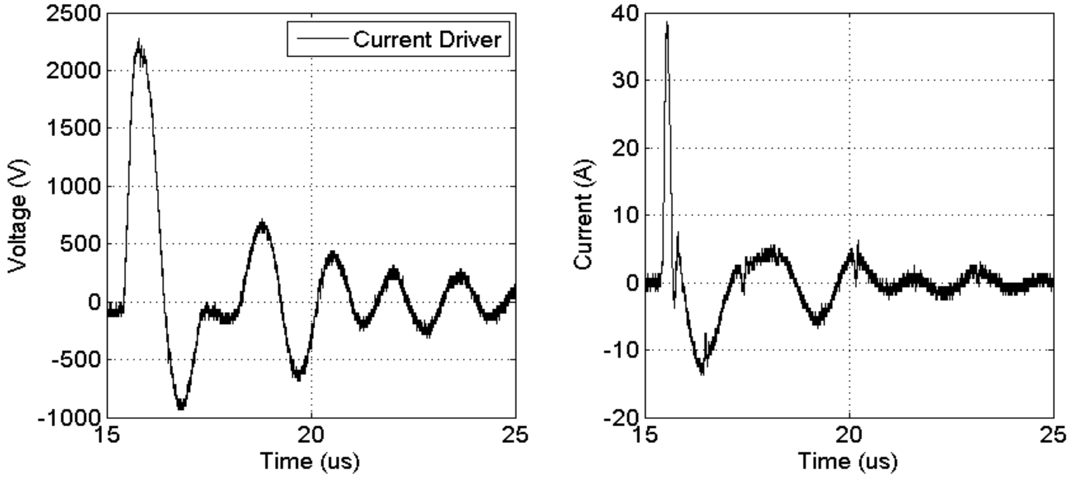

Figure B.7. Voltage and current pulse excitation delivered to a 500 kHz, acoustically matched PZT-8 module at the time the transistor switch is cycled off. Notice the extremely short current spike as the inductor is initially discharged into the transducer.

With properly matched transducers, the current driver is typically able to deliver significantly higher instantaneous peak-to-peak voltages to the piezoelectric elements than class-D amplifiers with impedance transformation networks (Figure B.8). This enables temporally narrow histotripsy pulses to reach high peak rarefactional values that would only be possible with longer pulses with additional cycles. Figure B.9 shows the maximum focal pressures obtained from the PZT-8 module driven using the voltage pulses shown in Figure B.8.

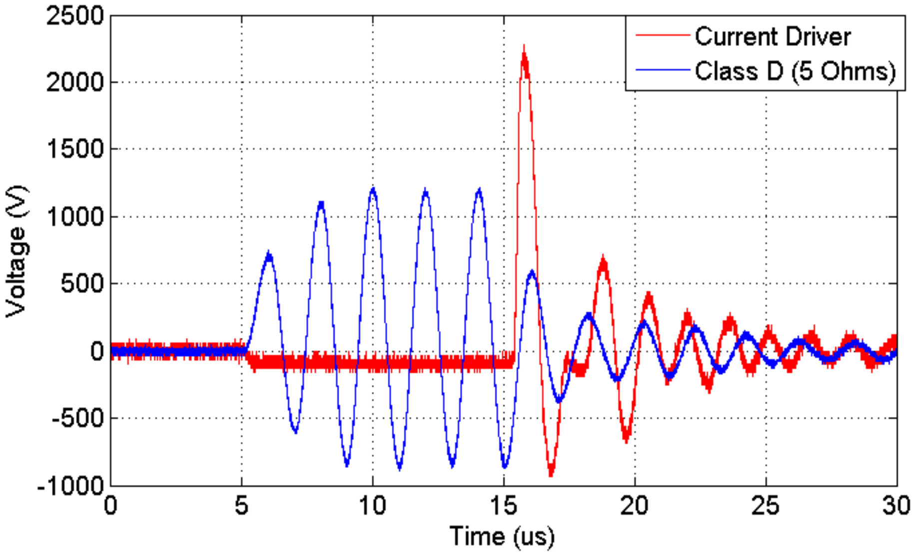

Figure B.8. Maximum voltage amplitude waveforms measured across the PZT-8 module driven with an inductor charge current driver (red) and class-D amplifier matched at 5 Ω (blue). Notice the 10 µs charging pulse in the current driver before the pulse is launched.

It is interesting to note that while the effective peak rarefactional pressures for both pulses are similar, at approximately 4 MPa, the class-D pulse appears to require at least 3 cycles in order to reach this level because of the finite acoustic bandwidth of this transducer. Additional developments in acoustic matching layer fabrication techniques would likely improve the ultrasound radiation output of PZT transducers driven with short pulses, further increasing the utility of the inductor current driver design for non-invasive histotripsy applications.

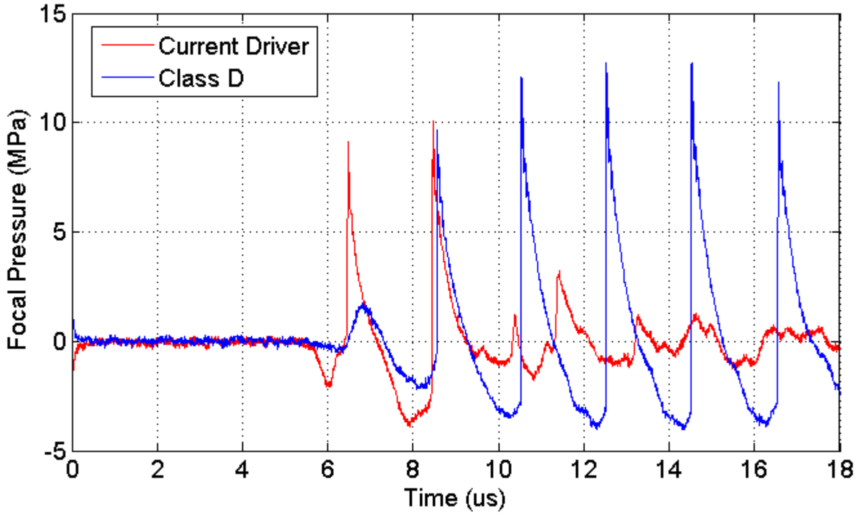

Figure B.9. Maximum focal pressure waveforms obtained with the test PZT-8 module pulsed by the inductor current driver (red) and by a class-D amplifier with a 5 cycle pulse (blue). Measurements were taken at a standoff distance of 15 cm from the element.

B.4 References

[1] S.-A. El-Hamamsy, "Design of high-efficiency RF class-D power amplifier," *IEEE Transactions on Power Electronics*, vol. 9, pp. 297-308, 1994.

[2] T. Hall and C. Cain, "A low cost compact 512 channel therapeutic ultrasound system for transcutaneous ultrasound surgery," *5th International Symposium on Therapeutic Ultrasound*, 2006.

[3] A. D. Maxwell, "Noninvasive Thrombolysis Using Histotripsy Pulsed Ultrasound Cavitation Therapy," Doctoral Dissertation, Dept. of Biomedical Engineering, University of Michigan, Ann Arbor, 2012.

[4] B. J. Baliga, *Fundamentals of Power Semiconductor Devices*, 1st ed. New York: Springer, 2008.

[5] M. Berkhout, "An integrated 200-W class-D audio amplifier," *IEEE Journal of Solid-State Circuits*, vol. 38, pp. 1198-1206, 2003.

[6] J. Hancock, "A class D amplifier using mosfets with reduced minority carrier lifetime," *Journal of Audio Engineering Society*, vol. 39, pp. 650-662, 1991.

[7] M. T. Bernius and A. Chutjian, "Improved high-voltage, high-frequency square-wave generator," *Review of Scientific Instruments*, vol. 61, pp. 925-927, 1990.

[8] W. Jiang, "Fast high voltage switching using stacked MOSFETs," *IEEE Transactions on Dielectrics and Electrical Insulation*, vol. 14, pp. 947-950, 2007.

Appendix C

Hemispherical Array Design using Rapid Prototyping Technology

This appendix discusses recent in-house advancements in prototyping and fabrication techniques for the assembly of experimental transducers for histotripsy therapy. A brief overview of rapid prototyping is given, followed by a detailed description of the design, fabrication and assembly process of a large aperture hemispherical array transducer for transcranial therapy as discussed in Chapter 6. The array output is acoustically characterized and compared to simulation results to evaluate this design approach, as well as the potential of using 3D rapid prototyping technology for the fabrication of custom histotripsy transducers.

C.1 Rapid Prototyping

Rapid prototyping techniques have been in use in industry for a number of years, as useful tools for model visualization during early stages of product development. Unlike traditional manufacturing and machining methods, rapid prototyping fabrication methods such as Selective laser sintering (SLS) and Stereolithography (SLA) enable complex prototypes to be quickly assembled, tested and optimized, considerably simplifying design iteration [1]. This allows production costs to be substantially reduced since part visualization is facilitated and design errors may be identified earlier in the development process, and not during production stages, where costs for design changes significantly increase. Further improvements in 3D printing materials and technologies have extended the reach of rapid prototyping applications in recent years, from simple modeling to the fabrication of fully functional parts [2].

The versatility and flexibility afforded by rapid prototyping systems have been a key catalyst in transducer development efforts for histotripsy research, considerably simplifying the design and fabrication of experimental transducers. Over the years, rapid prototyping methods have been increasingly used in the construction of custom histotripsy transducer designs of significant complexity for a growing number of applications including thrombolysis, kidney stone erosion, neonatal cardiac ablation, and lymph node treatments, with promising results.

As discussed in Chapter 6, transcranial therapy has been one of the most recent, and perhaps the most challenging applications investigated for non-invasive histotripsy therapy, requiring the construction of a high gain transducer array sufficiently powerful to generate cavitation through the highly attenuative skull. The design presented herein is the culmination of several years of collaborative efforts involving the development and evaluation of numerous fabrication techniques and material formulations to optimize the acoustic performance of PZT transducers built in-house. The following sections provide details on the fabrication and assembly techniques involved in this process, illustrating the significant developments achieved in this area, as well as the potential of using rapid prototyping technology in the fabrication of experimental transducers for histotripsy applications.

C.2 Array Design and Assembly

The initial mechanical design of the transducer components was conducted using a professional computer-aided design (CAD) package (Autodesk Inventor 2011, Autodesk Inc., San Rafael, CA). Design parameters aimed to achieve maximum focal gain at a relatively low center frequency to reduce the susceptibility of the therapy focus to acoustic aberration effects from the skull. A hemispherical shape was chosen to maximize the focal gain parameter of the transducer and also distribute the ultrasound radiation over a large area of the skull, reducing the chance of creating localized regions exposed to excessive ultrasound radiation on the bone surface.

The array design was based on a modular approach, in which a larger array scaffold or shell is populated by identical, individually focused element modules. Previous histotripsy transducers fabricated using rapid prototyping consisted of smaller transducer arrays containing fewer than 10 elements, which were typically directly assembled onto the transducers' frontal aperture. In the construction of larger arrays, a modular assembly method offers three main benefits: 1) because each element module can be independently fabricated and individually tested, it may help improve the acoustic output consistency of the array; 2) the ability to separately construct each module substantially simplifies the assembly procedure for the entire array structure, especially in a large hemispherical configuration; and 3) in case failure of one or more elements, this design can be easily repaired and restored to full operational capability, since failed elements may be simply removed and replaced with new modules.

The array scaffold and the element modules were fabricated through a 3D stereolithography (SLA) printer (3D Systems Corporation, Rock Hill, SC). Previous histotripsy transducers were fabricated using a proprietary clear plastic material (Accura® 60), which was recommended by the manufacturer for the fabrication of functional prototypes due to its hardness and transparency, facilitating the identification and diagnosis of potential sources of transducer or electrical failures inside enclosed transducer housings.

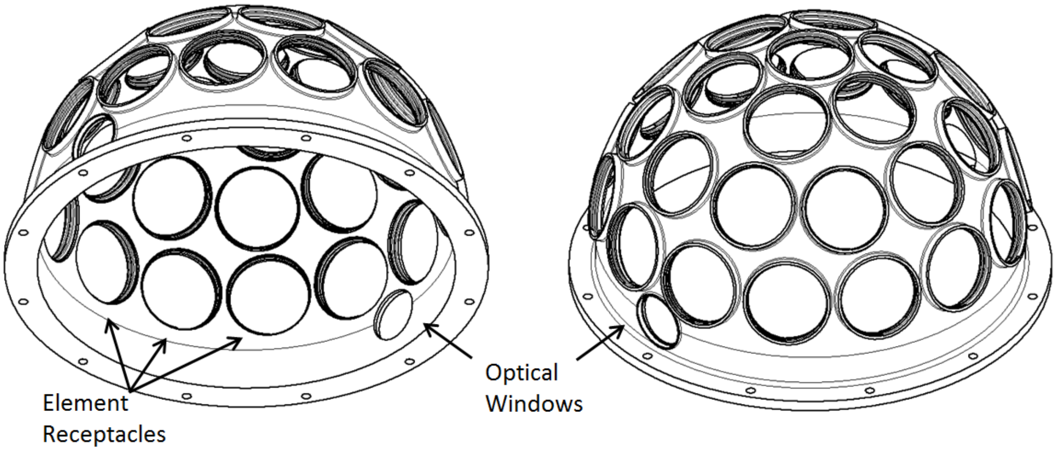

Figure C.1. Illustrations of the hemispherical array scaffold (150 mm focal length) containing 32 threaded receptacles.

The main transducer scaffold consists of a hemispherical shell, with a front aperture diameter of approximately 300 mm and a geometric focal length of 150 mm (Figure C.1). The shell is populated with 32 threaded receptacles which are designed to accommodate individual element modules. In addition, two diametrically opposed glass windows are available on the side of the shell to allow for optical imaging of the geometric focus. The array was specifically designed to be mounted in the side of a tank with a circular hole machined for that purpose.

The outer walls of each active element housing module (Figure C.2) are externally threaded to match the receptacles in the array scaffold. The threaded design allows each module to be firmly attached to the scaffold without the need of using additional bolts or permanent adhesives, which also facilitates module removal if necessary (Figure C.3). The front of the module consists of an elliptical acoustic lens focused at 150 mm, which is also the geometric focus of the array. While individual element focusing limits the steering capabilities of the array, this approach was taken in order to maximize the focal gain of the transducer. The elliptical lens design was specifically chosen to avoid aberration effects from spherically curved lenses [3].

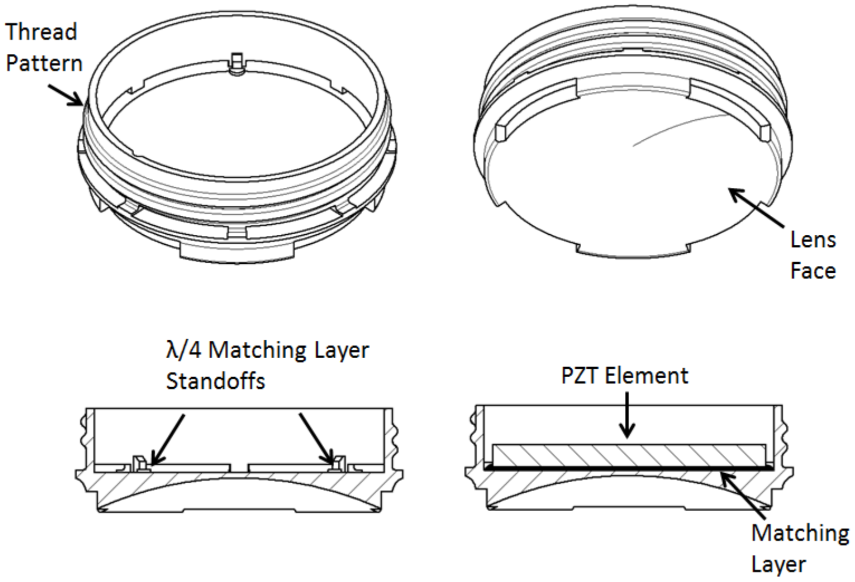

Figure C.2. Design drawings of a single element module housing showing the outer threads and the elliptical lens (top row). Cutout views (bottom row) show the matching layer standoffs inside the housing in order to achieve the correct layer thickness when assembling the module. The quarter-wavelength gap between the disc and the back of the elliptical lens is filled with a high acoustic impedance tungsten-epoxy compound specifically formulated for this purpose.

The piezoelectric elements used in this design were 50.8 mm diameter, 4.2 mm thick lead-zirconate-titanate (PZT) ceramic discs (5804 Navy III, Channel Industries Inc., CA). The thickness mode frequency constant N_t of this particular material is 2110 Hz-m, which when divided by the thickness of the discs yields a center resonance frequency of approximately 500 kHz. This relatively low operation frequency was chosen in this particular design to reduce the effects of ultrasound aberration and attenuation through the skull.

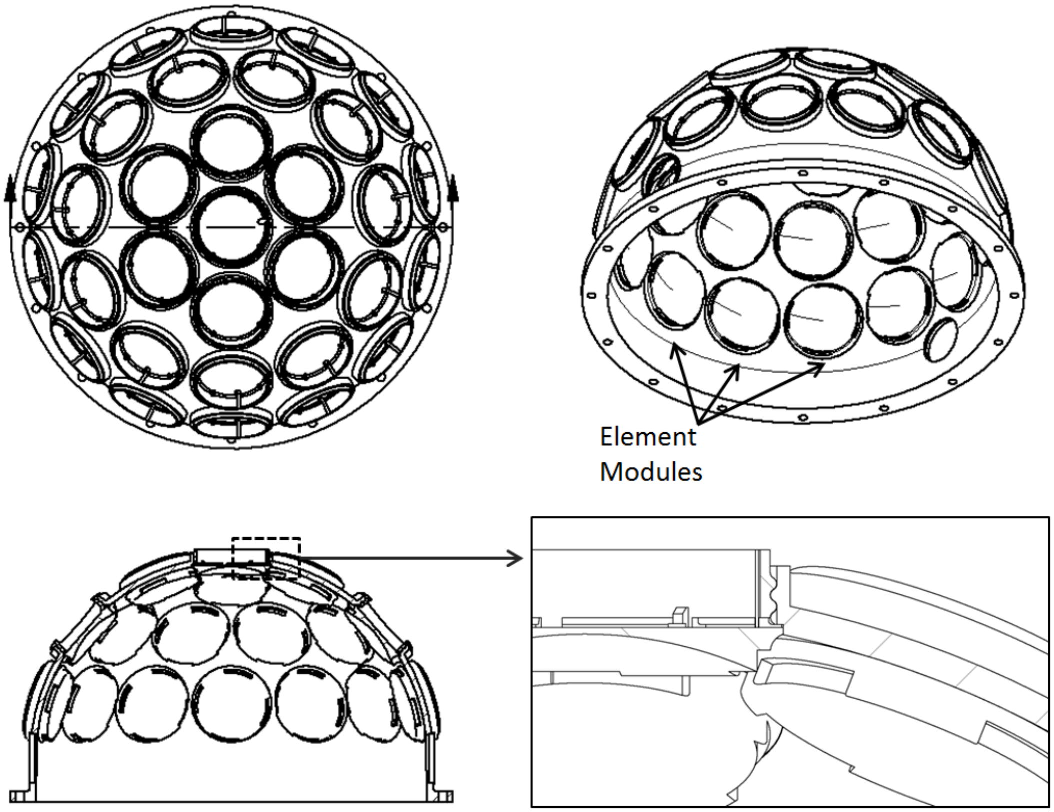

Figure C.3. Drawing of the fully populated array with 32 element modules (top row). A cutout view shows a detail view of the threaded connection between the array scaffold and each module (bottom row).

To improve the acoustic radiation efficiency and the electroacoustic bandwidth of the array elements, each PZT disc was coupled to the housing module by way of a single quarter-wavelength matching layer. The matching layer composition was specifically formulated to improve the acoustic matching between the PZT disc and the housing lens terminated by the propagation medium (water). Based on the work of Maréchal et al. [4], a tungsten-epoxy mixture was developed in house through extensive tests involving a variety of composite materials. Further details on the acoustic matching layer materials used in the fabrication of histotripsy transducers may be found in the dissertation work by Maxwell [5]. To maintain the consistency of the matching layer thickness during assembly, each element housing module has four quarter wavelength matching layer standoffs positioned around the perimeter of the back of the lens (Figure C.2).

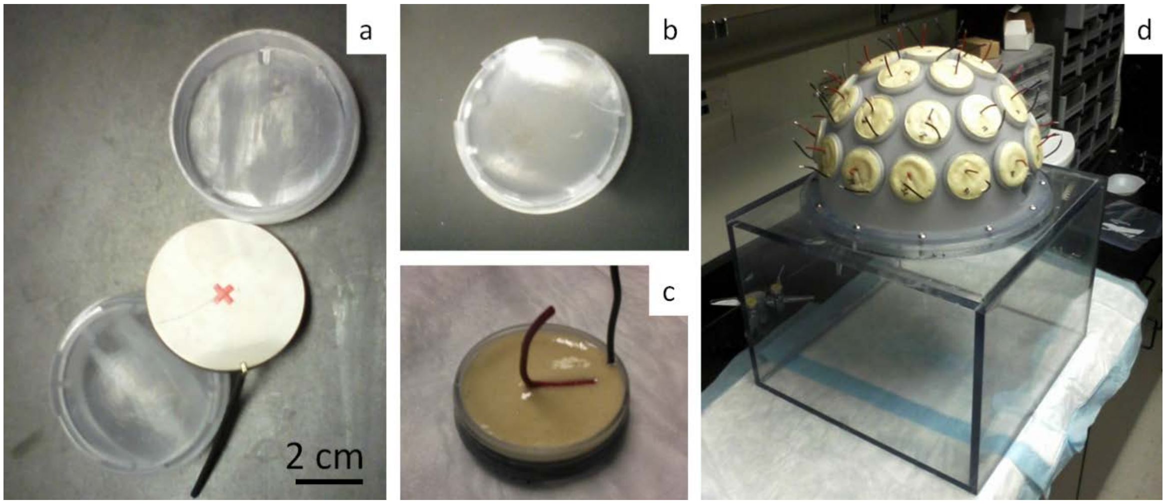

Figure C.4. Pictures of the assembly process of the array. Single 50 mm diameter PZT-8 disc with empty housing modules (a). Frontal view of a single assembled module with matching layer compound applied between the ceramic disc and the lens (b). Application of urethane compound to seal the backside of the element (c). Fully populated array shell mounted on the side of a water tank (d).

After the elements were mounted into the housing modules and the epoxy mixture was fully cured, a urethane foam compound was applied to the back of each module (Figure C.4). This self-setting foaming material was chosen in order to allow the transducer to be air-backed while still providing a waterproof seal and a tension relief mechanism for the electrode contact wires soldered onto the PZT disc.

C.3 Acoustic Characterization

The following paragraphs describe the methods and parameters used in the characterization of the PZT element modules and the fully assembled transducer. A field-programmable gate array (FPGA) was used as a custom pulse generator to electronically control each channel (Altera Corp., San Jose, CA). The FPGA was connected to a 32-channel bank of inductor current drivers developed in-house as described in Appendix B.

Focal pressure profiles were mapped with a high sensitivity hydrophone (model HNR-0500, Onda Corporation, Sunnyvale CA) and compared to transient simulation results. To prevent cavitation damage to the piezoelectric hydrophone, high pressure focal calibration measurements were conducted with a separate fiber optic probe hydrophone (FOPH) designed and built in-house.

C.3.1 Single Modules

Prior to the assembly of the array, each transducer module was individually characterized and tested in order to assess its integrity and acoustic characteristics. Initial impedance measurements were conducted with a network analyzer (VNA 2180, Array Solutions, Sunnyvale, TX) to check the acoustic matching layer consistency. Figure C.5 gives representative impedance plots measured for a single PZT module. The measured mean and standard deviation of the impedance magnitudes of all 32 elements were

$Z_{mag} = 109.0 \pm 10.2\,\Omega$ indicating that the quarter-wavelength matching layer standoffs designed for the element housing were effective in maintaining the consistency of the matching layer thickness throughout the elements.

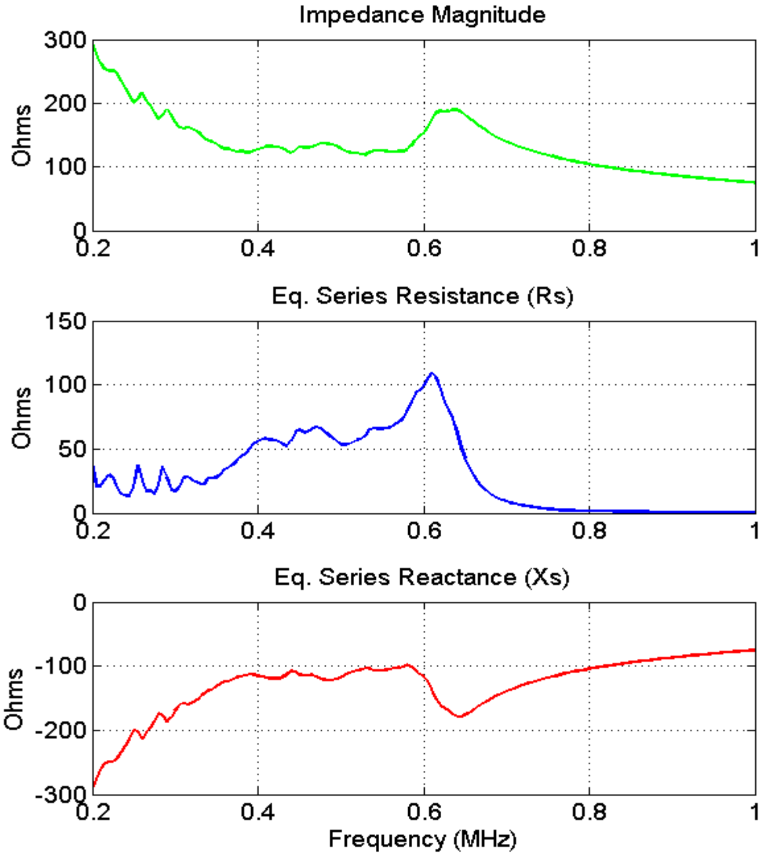

Figure C.5. Representative magnitude, real and imaginary impedance measurements of a single 2 inch acoustically matched PZT element module used in the transducer array. Acoustic matching was observed to substantially increase the impedance of the PZT modules. At 500 kHz, the mean impedance magnitude value measured for all 32 elements was approximately 109 Ω.

Figure C.6 shows normalized near-field "surface" pressure and focal pressure plots measured in the linear (low amplitude) regime. FWHM measurements of the surface profile and focal profile were 43 mm and 16 mm respectively. The measured linear focusing gain provided by the lens with respect to the maximum pressure measured at this near-field surface was approximately 3. Due to the curvature of the lens, the near field pressure measurements reported herein were performed at a standoff distance of approximately 8 mm from the vertex of the lens, possibly explaining the comparatively smaller FWHM pressure profile obtained at this plane relative to the actual diameter of the PZT element (50.8 mm) used in the assembly of the module.

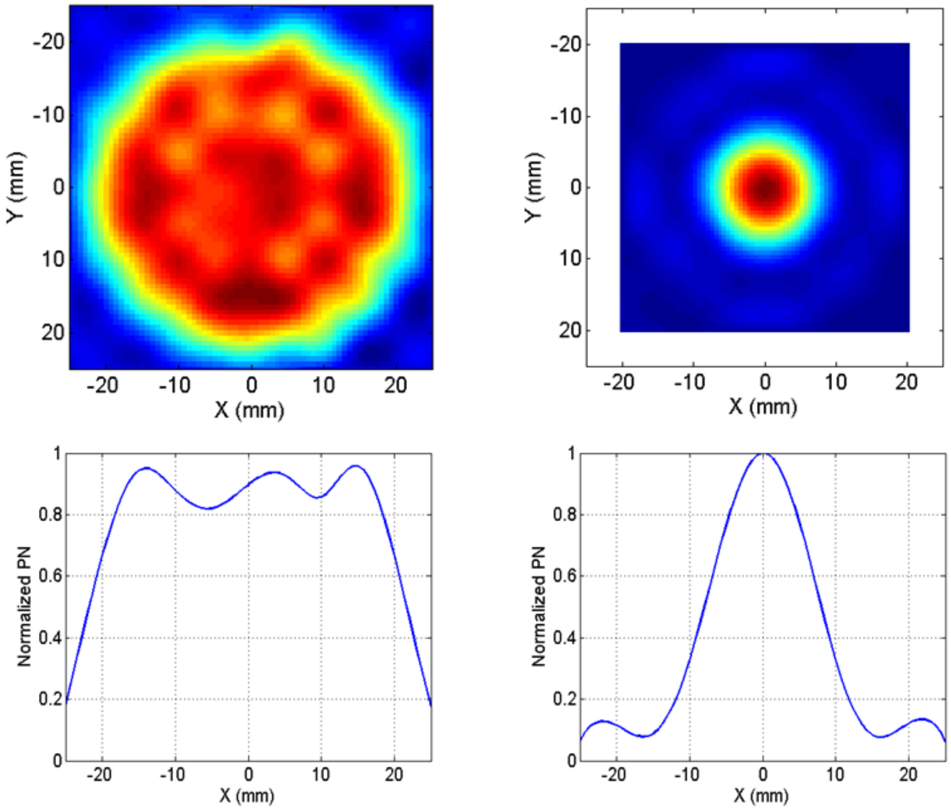

Figure C.6. Normalized near-field surface (left column) and focal plane (right column) pressure scans of a single element module. The approximate dimensionless focusing gain factor with respect to the surface pressure measurements was approximately 3.

In combination with a 47 µH parallel inductor, a charging pulse of 10 µs allowed maximum peak-to-peak voltages of over 3000 V to be reached across the PZT element, enabling each module to output short ultrasound pulses of less than 2 full cycles and peak rarefactional pressures exceeding 3.5 MPa at the geometric focus of the array (Figure C.7).

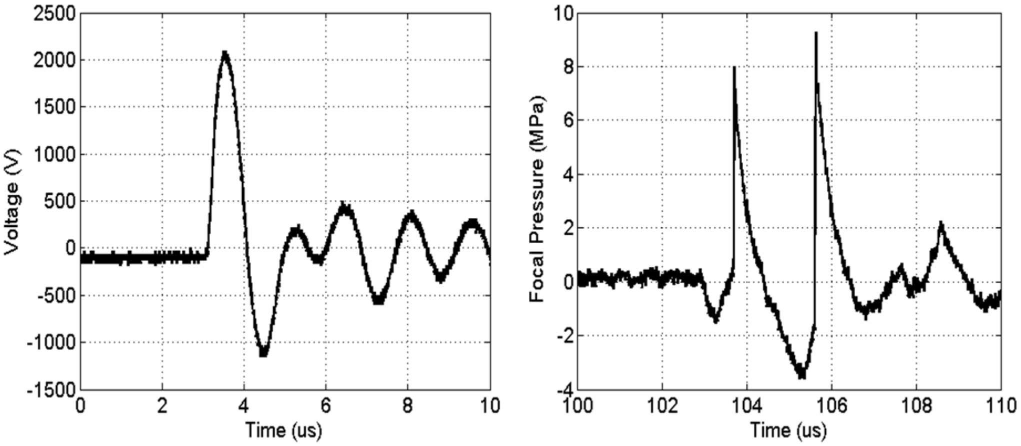

Figure C.7. Representative maximum voltage excitation amplitude achieved across a single element module (left) and its corresponding pressure waveform at the geometric focus of the lens (right). Each module is capable of achieving peak rarefactional pressures of over 3.5 MPa at the focus.

C.3.2 Hemispherical Array

The fully populated array with 32 elements was acoustically characterized to evaluate the degree of accuracy afforded by the modular assembly method. Very good agreement was found between simulation and measured results of the transducer array's focal profile, especially along the transversal X and Y coordinates (Figure C.8). The FWHM of the main beam was approximately 1.8 x 3.9 mm in the transversal and axial coordinates, respectively.

The threaded contacts between the individual element housing modules and the array scaffold appeared to provide an effective attachment contact for all elements. To assess any element placement inconsistencies in the array, each element module was individually pulsed with a hydrophone positioned at the geometric focus of the array. The time-of-arrival of the maximum rarefactional cycle in all elements had a mean and standard deviation of 105.09 ± 0.07 μs, with all measurements falling within the range of

104.96 to 105.31 µs (Figure C.9). At 500 kHz, this interval corresponds to less than one-fifth of a full period (2 µs), which provided a satisfactory degree of element alignment for this particular application.

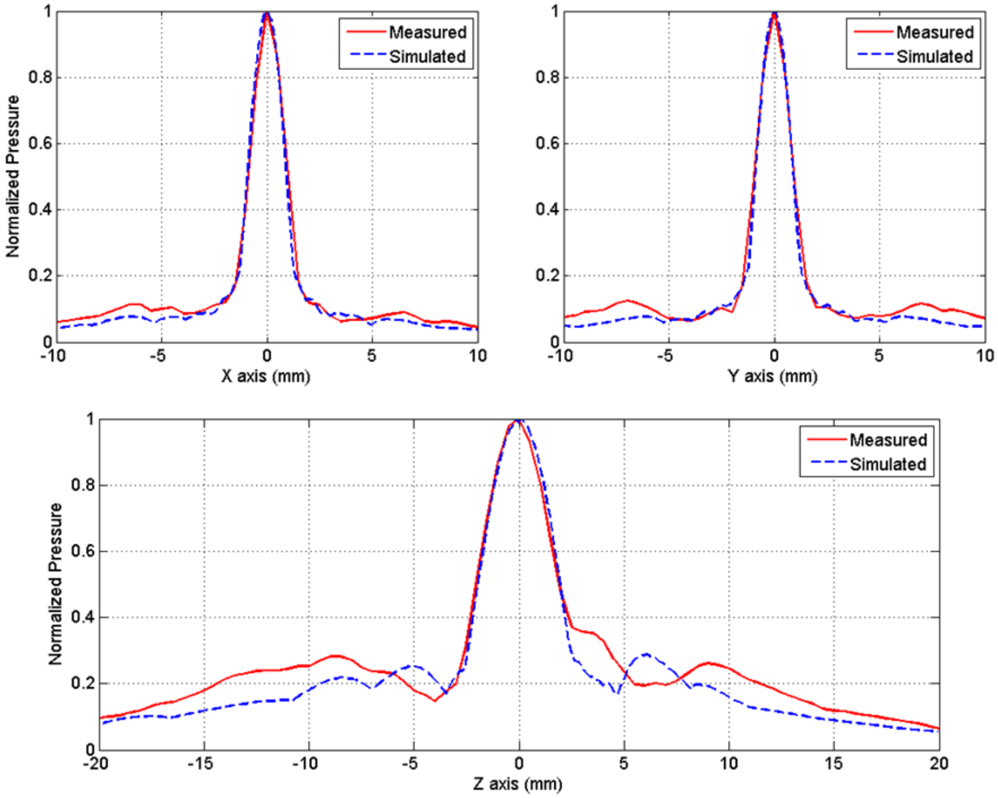

Figure C.8. Measured and simulated linear focal pressure profile plots for the hemispherical array. Transversal (X and Y) and axial coordinates (Z) are shown. The largest secondary lobe amplitude for both simulated and measured results was approximately 29% of the main beam.

Direct maximum focal pressure measurements were limited by the initiation of cavitation at the tip of the measuring probe at rarefactional pressures exceeding 23 MPa, which could be achieved at approximately one-fifth of the full power allowed by the system. In order to estimate the maximum potential pressure capabilities of the array, individual waveforms from each element module were collected and superimposed at the focus. Using this linear approach, the theoretical maximum peak rarefactional pressure that could be potentially reached at the focus of the array in the absence of cavitation was in excess of 100 MPa (Figure C.10). It should be emphasized that this is only a theoretical figure of merit used for convenience since water would not be able to physically sustain such high tensile forces, and cavitation would occur at the focus long before this pressure is reached.

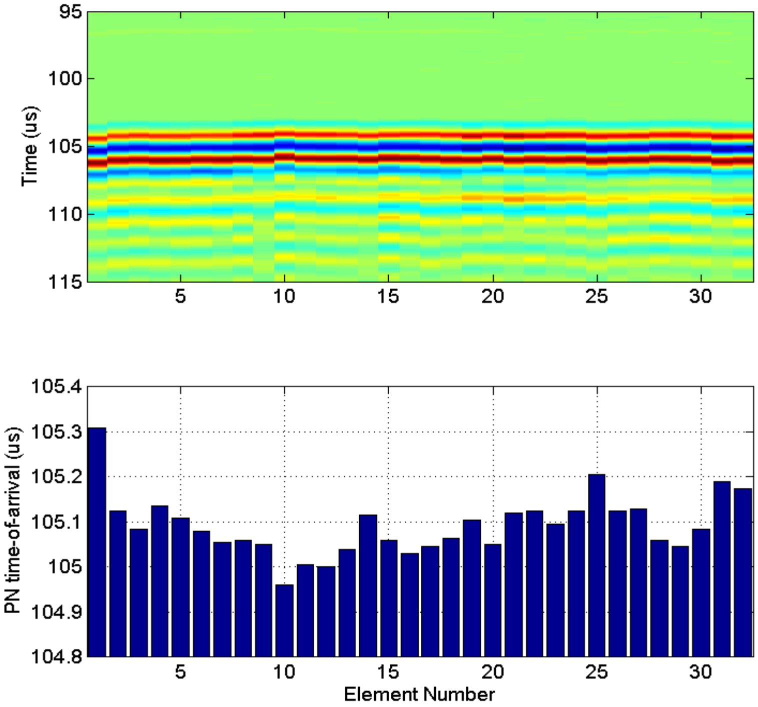

Figure C.9. Time-of-flight measurements for individual elements performed with a hydrophone positioned at the geometric focus of the array (top panel). Time-of-arrival data for the peak rarefactional cycle in each pulse (bottom panel).

This extrapolation method is limited and does not account for non-linear effects developed during propagation. However, while highly shocked peak compressional pressures cannot be estimated using this approach, peak rarefactional amplitudes associated with the fundamental frequency of the transducer may be amenable for linear extrapolation [6]. Furthermore, the relatively sparsely populated element packing of the array limits the overlap of the individually focused sound fields from adjacent elements modules until near the geometric focus, reducing the possibility of inducing additional non-linear effects in the near-field of the transducer.

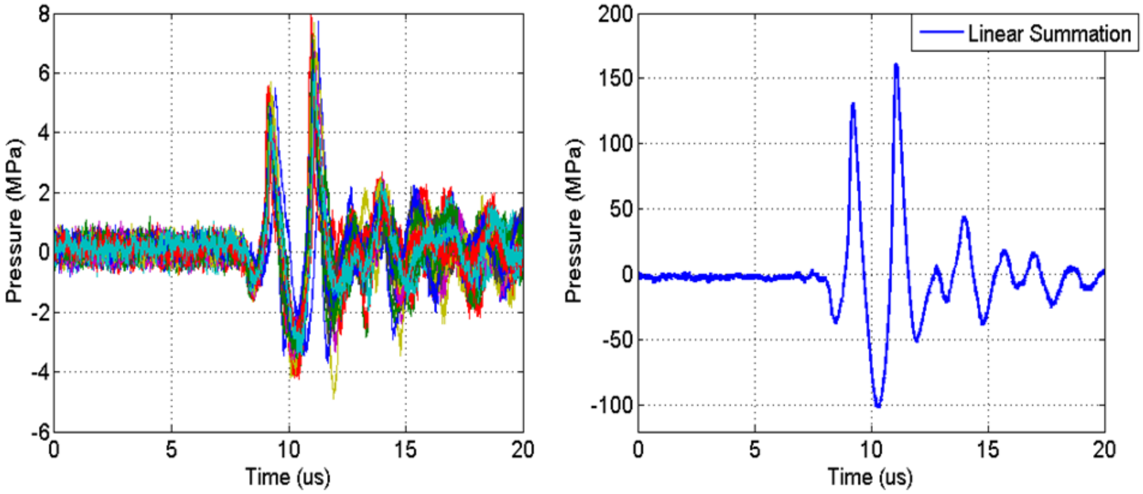

Figure C.10. Maximum focal pressure waveforms from individual elements measured at the geometric focus of the array (left panel). Maximum estimated focal pressure obtained from linear summation of the 32 waveforms (right panel).

The large instantaneous peak rarefactional pressure capabilities afforded by this transducer can allow the initiation of dense and consistent “intrinsic” bubble clouds at the focus of the array without the shock scattering phenomena observed in traditional, multi-cycle histotripsy therapy. Figure C.11 shows cavitation bubbles generated by this array in water at a repetition rate of 1 Hz. The effective size of the cloud could be consistently modulated by increasing the input voltage to the transducer, until an estimated peak rarefactional pressure of 90 MPa (using linear superposition) was reached at the focus, beyond which, additional bubbles appeared to be initiated along the axial length of the array. At such elevated focal pressures, it was likely that pressure levels in the axial secondary lobes (29% amplitude of the main beam) were reaching the intrinsic cavitation threshold (Figure C.8).

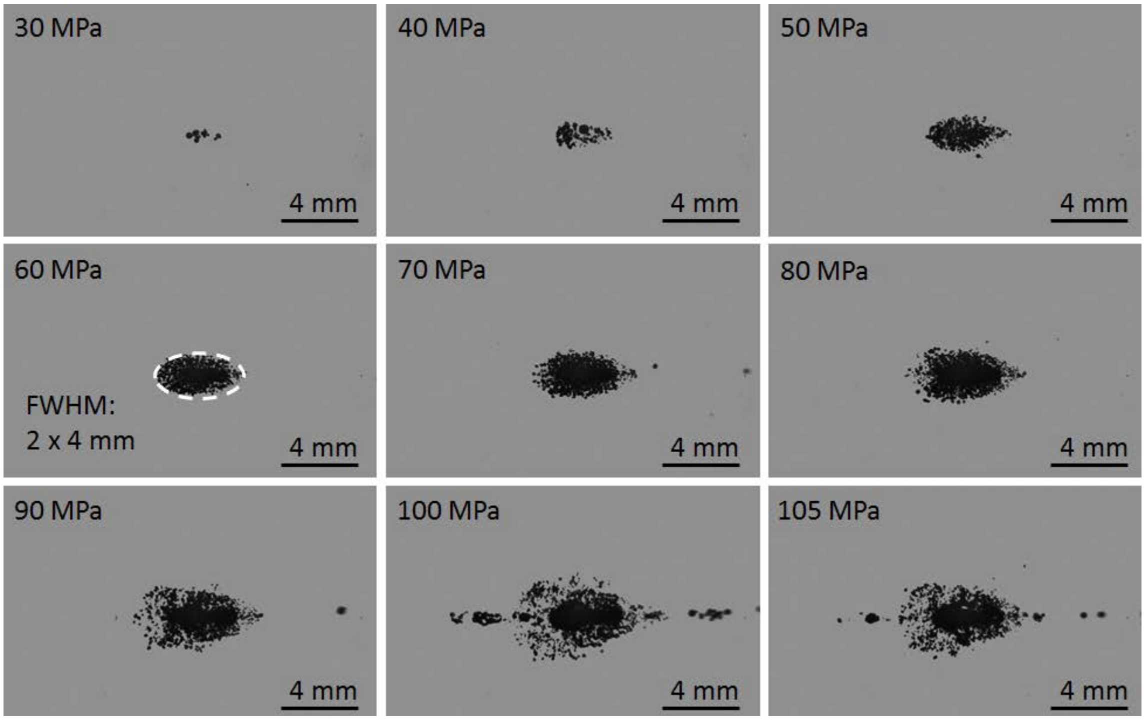

Figure C.11. Bubble clouds imaged in degassed water under free-field conditions with estimated focal peak rarefactional pressures. Short pulses (< 2 full cycles) were applied at a PRF of 1 Hz. Axial planes are shown. Ultrasound propagation: left to right.

As discussed in Chapter 6, the supra-intrinsic threshold short pulse sonication regime used by this array can allow significantly higher ablation precision and control to be achieved. While this particular array was designed for transcranial applications, the fabrication and assembly techniques described herein may be easily adapted and applied for a variety of other custom transducer geometries. Additional refinements in element construction, matching layer formulation and electronic driving systems will allow further improvements in pressure output capabilities, potentially enabling smaller aperture transducers to reach the high rarefactional pressure levels required for intrinsic threshold bubble cloud initiation. With the extended fabrication capabilities afforded by rapid prototyping, this could lead to the development of more portable high power transducer designs, which would be useful for many non-invasive histotripsy applications.

C.4 References

[1] X. Yan and P. Gu, "A review of rapid prototyping technologies and systems," *Computer-Aided Design*, vol. 28, pp. 307-318, 1996.

[2] A. P. Nyaluke, D. An, H. R. Leep, and H. R. Parsaei, "Rapid prototyping: applications in academic institutions and industry," *Computers ind Engng*, vol. 29, pp. 345-349, 1995.

[3] L. Schlussler, "The design and test results for an acoustic lens with elliptic surfaces," *J Acoust Soc Am*, vol. 67, pp. 699-701, 1980.

[4] P. Maréchal, F. Levassort, L.-P. Tran-Huu-Hue, and M. Lethiecq, "Lens-focused transducer modeling using an extended KLM model," *Ultrasonics*, vol. 46, pp. 155-167, 2007.

[5] A. D. Maxwell, "Noninvasive Thrombolysis Using Histotripsy Pulsed Ultrasound Cavitation Therapy," Doctoral Dissertation, Dept. of Biomedical Engineering, University of Michigan, Ann Arbor, 2012.

[6] A. D. Maxwell, C. A. Cain, T. L. Hall, J. B. Fowlkes, and Z. Xu, "Probability of cavitation for single ultrasound pulses applied to tissues and tissue-mimicking materials," *Ultrasound Med Biol*, vol. 39, pp. 449-65, Mar 2013.

Appendix D

Electroacoustic Characterization of a PZT Stack Module

This section presents initial characterization results obtained from an experimental PZT stack module designed to increase the acoustic pressure output capabilities of histotripsy transducers using short pulse sonication methods. A brief description of the stack assembly process is provided, and the acoustic performance of a 500 kHz two-element PZT stack module is compared to that of a single element module of similar dimensions and center frequency.

D.1 PZT Stack Assembly

The concept of stacking piezoelectric elements for improved electromechanical performance is not new and has been extensively applied in the construction of piezoactuators used in a variety of industrial and research fields [1, 2]. Because piezoelectric constants for typical PZT (Lead-Zirconate-Titanate) ceramics fall in the range of sub-nm/V [3], mechanically joining several single PZT elements in series is a common approach used to extend the displacement capabilities of PZT structures.

Under this configuration, elements are bonded together by their common polarities, and the stack is electrically connected in parallel while remaining mechanically in series (Figure D.1). This allows all the component elements of the assembly to be driven simultaneously by a single high voltage excitation source, enabling greater mechanical displacements to be achieved in comparison to those from a single element of equivalent thickness. Assuming an ideal bond is formed between the component elements, the resulting resonant frequency of a PZT stack is given by f/n, where f is the thickness resonant mode of a single element and n is the number of elements used in the assembly of the stack.

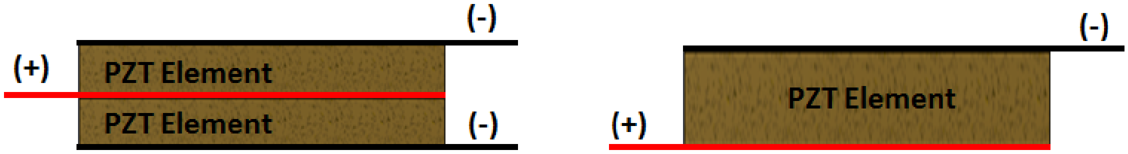

Figure D.1. Electrode diagram for a two-element PZT stack (left) vs. a single PZT element of equivalent thickness (right).

Initial tests were performed with a PZT stack module assembled with two 1 MHz PZT-4 discs (SM 111, Steiner & Martins, Inc., FL). Each individual disc had a diameter of 50 mm and a thickness of 2.1 mm, giving the overall stack a thickness of approximately 4.2 mm and a center frequency of 500 kHz. In order to gain access to the electrode shared by both elements, ceramic discs with a "wrap-around" electrode configuration were used to assemble the stack (Figure D.2). The wrap-around configuration exposes both electrodes (+ and -) to the "top" side of the discs, making the "bottom" side electrode (+) accessible for wiring connections. The wrap-around electrode of the lower element of the stack (which comes in contact to the lens housing through a conductive matching layer) was chemically etched prior to assembly to avoid short-circuit effects.

The two elements were bonded by a thin layer of high strength epoxy that was allowed to cure for 24 hours. Constant pressure was applied on the stack during this process using a bar clamp to minimize the thickness of the epoxy layer and remove potential air bubbles trapped between the two PZT surfaces. The PZT stack was then mounted into a focused housing module similar to that described in Appendix C using the same tungsten-epoxy matching layer composition.

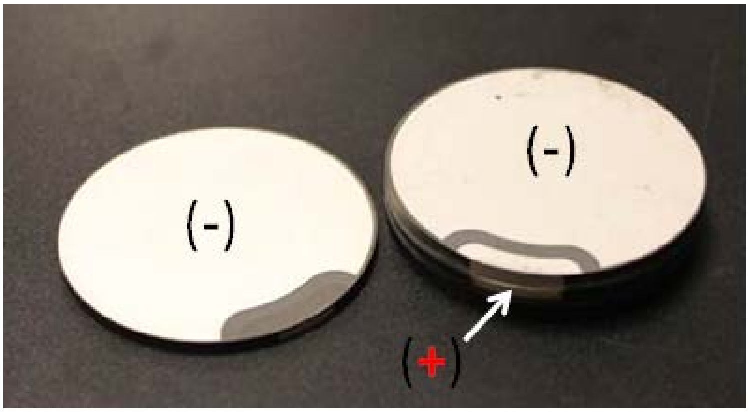

Figure D.2. Picture of a single 1 MHz PZT-4 disc (50 mm x 2.1 mm) on the left, and an assembled stack on the right. The wrap-around electrode on the single disc (used as the lower element in the stack assembly) was removed to prevent short circuiting across the conductive matching layer used in the acoustic lens assembly. Both elements in the stack were bonded by their (+) polarity side.

D.2 Electroacoustic Measurements

Electrical impedance measurements of the acoustically matched PZT stack module were obtained with a network analyzer as described in the previous appendix. At a center frequency of 500 kHz, the effective impedance magnitude of the stack module was $Z_{mag} = 27.8\ \Omega$ (Figure D.3), approximately one-fourth of the value measured from single element 500 kHz modules. This result agrees well with expectations, as the PZT stack consists of two electrically parallel elements half the thickness of the PZT discs used in the assembly of single element modules.

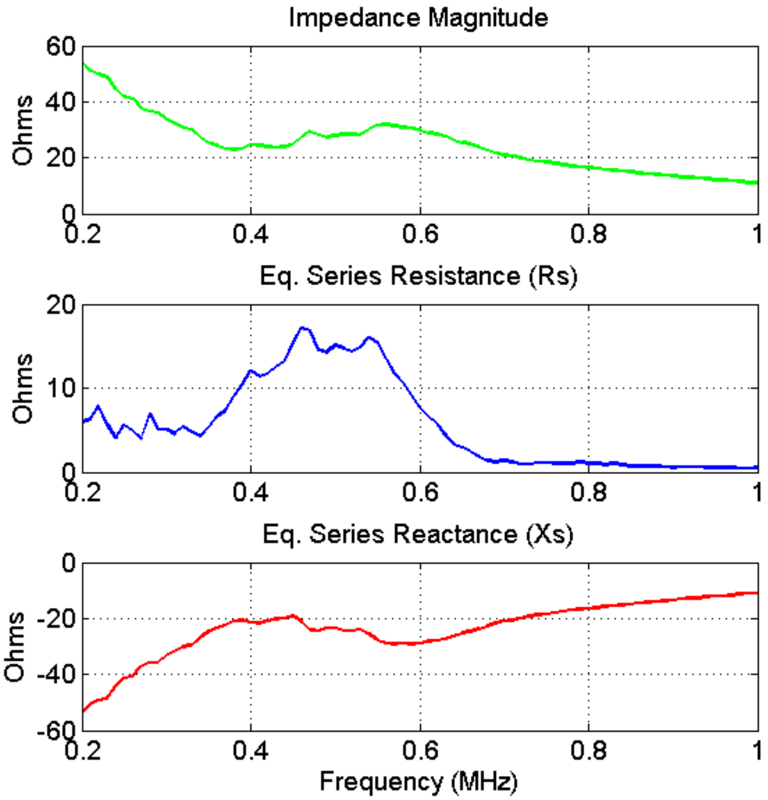

Figure D.3. Magnitude, real and imaginary electrical impedance measurements of an acoustically matched, two-element PZT stack module. At a center frequency of 500 kHz, the impedance magnitude of the module was 27.8 Ω.

Linear measurements (low amplitude) and high pressure focal measurements were collected for both transducers at comparable peak to peak voltage ranges using the inductor current driver system described in Appendix B. Figure D.4 shows normalized 2D scans of the near-field surface pressure distribution of each module referencing peak rarefactional (P-) pressures. The wrap-around electrode configuration introduced a noticeable loss in the surface radiation pattern of the stack module in comparison to that generated by a single element module, which appeared to present a more homogeneous pressure distribution within its surface aperture.

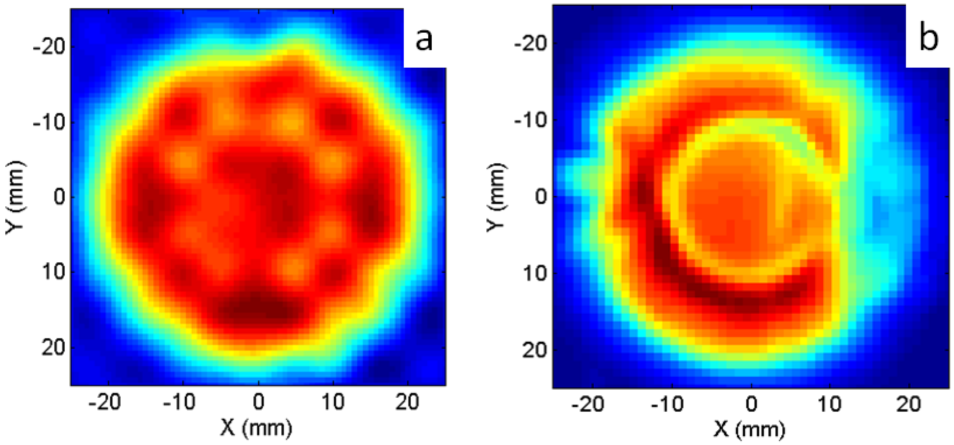

Figure D.4. Normalized linear surface pressure distribution of a single element module (a), and the two-element stack module (b). Notice the region of radiation loss in the stack module aperture due to the wrap-around electrode configuration.

Figure D.5a shows the on-axis maximum surface pressure waveforms obtained with each module. Direct and edge waves generated by the modules could be differentiated at this location, and the P- value of the direct wave was chosen as a reference for surface pressure measurement purposes. At maximum output, the stack module was able to generate a P- amplitude of approximately 2.8 MPa in comparison to the 1.4 MPa achieved by the single element module. When similar peak-to-peak voltages were applied, the surface P- amplitudes measured with the stacked module were approximately 2.2 times as high as those measured with a single element module, following a linear trend within the range of excitation voltages applied (Figure D.5b).

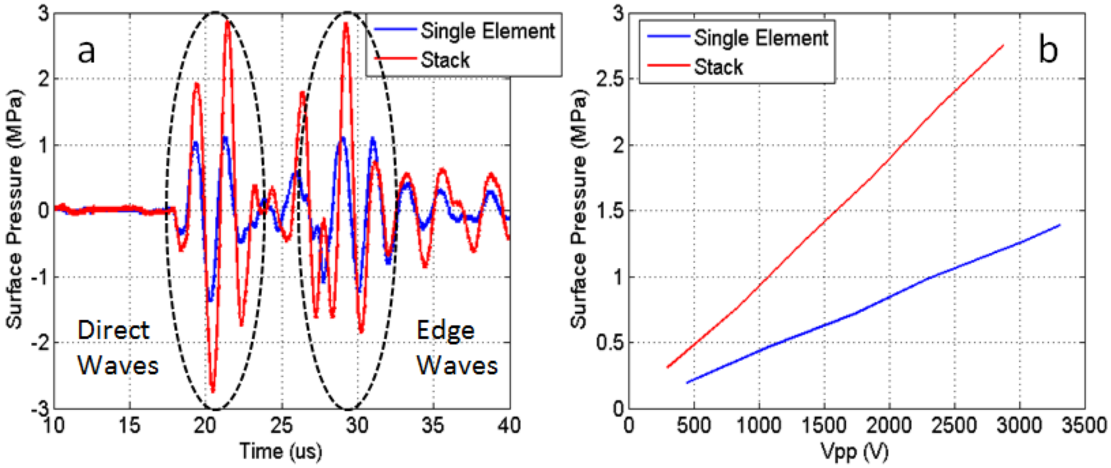

Figure D.5. Maximum on-axis surface pressure waveforms obtained with a single element module and the stack module (a). Direct and edge waves are indicated by the dashed contours. At the same excitation voltages (Vpp), the stack module was able to achieve more than twice the P- amplitude output by a single element module (b).

Despite the relative irregularity of the surface pressure profile generated by the stack module, transversal pressure profiles measured at the geometric focus of the transducer (15 cm) appeared to have good agreement with those of the single element module (Figure D.6). The maximum focal P- values obtained were approximately 3.6 and 4.4 MPa for the single element and stack modules, respectively (Figure D.7a). Unlike surface pressure measurements, focal P- amplitudes displayed a non-linear trend with respect to the applied excitation voltage, and acoustic saturation effects appeared to become more prominent as higher voltage amplitudes were applied to the elements (Figure D.7b).

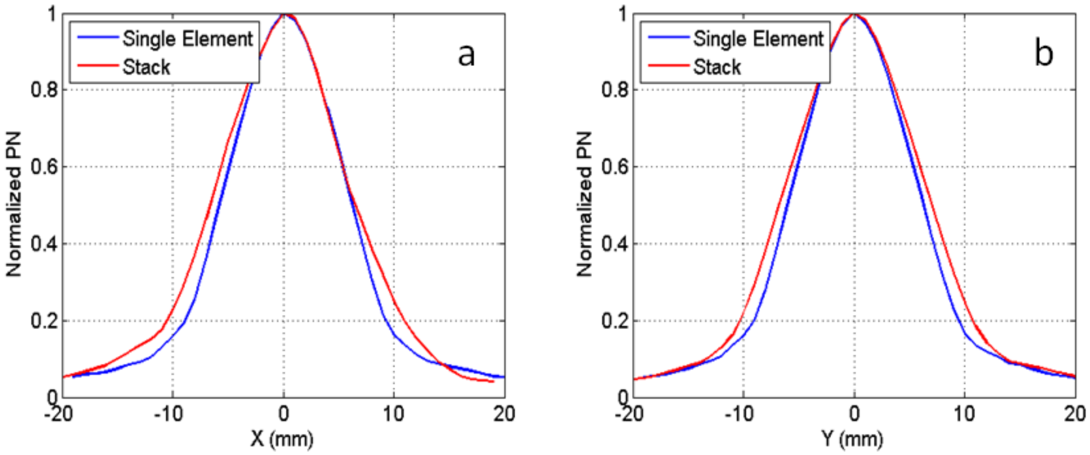

Figure D.6. Transversal linear pressure profiles measured at the geometric focus of a single element module and the stack module (a and b). Good agreement was observed for focal beam patterns generated by both transducers.

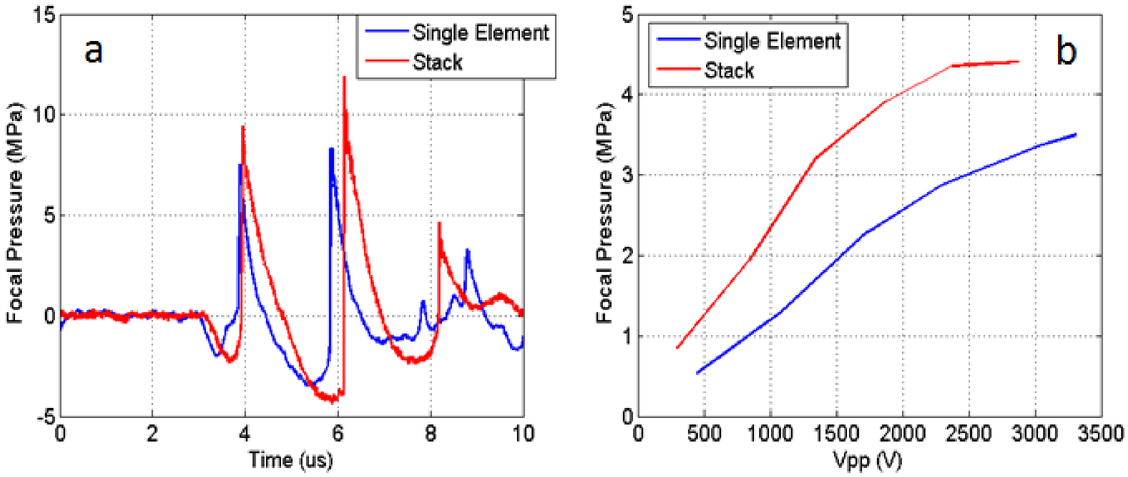

Figure D.7. Maximum focal pressure waveforms obtained with a single element module and the stack module (a). P- amplitudes measured at the focus with respect to the voltage amplitude applied to the elements (b). Acoustic saturation effects appeared to become more significant at higher voltage levels.

These initial results suggest that stacked element assembly may be an effective method to increase the overall pressure output of a transducer without using a larger acoustic aperture. In principle, further enhancement of acoustic output may be achieved by increasing the number of individual elements in the stack, at the cost of higher assembly complexity, and perhaps reliability (as thinner elements may be more susceptible to depoling effects when driven at higher voltage amplitudes).

It should be noted, however, that while larger surface or near field pressures may be easily achieved with this construction method, the greater impact of non-linearity and acoustic saturation effects could significantly reduce the effective focal pressure gain achievable for transducers with longer focal distances. The implementation of non-linear acoustic simulations would be beneficial in this regard, and could provide a more accurate estimate of pressure saturation limitations for specific transducer designs intended for different therapeutic applications.

D.3 References

[1] M. Goldfarb and N. Celanovic, "Modeling piezoelectric stack actuators for control of micromanipulation," *IEEE Control Systems*, vol. 17, pp. 69-79, 1997.

[2] M. Mitrovic, G. P. Carman, and F. K. Straub, "Response of piezoelectric stack actuators under combined electro-mechanical loading," *International Journal of Solids and Structures*, vol. 38, pp. 4357-4374, 2001.

[3] A. Safari and E. K. Akdogan, *Piezoelectric and Acoustic Materials for Transducer Applications*: Springer, 2008.